

# **Effect of Processing Routes on Deformation Behaviour and Microstructural Characteristics of Zircaloy-4**

**THESIS**

Submitted in partial fulfilment  
of the requirements for the degree of  
**DOCTOR OF PHILOSOPHY**

by

**K Limbadri**

**ID. No. 2016PHXF0118H**

Under the Supervision of

**Dr. Kurra Suresh**

&

Under the Co- Supervision of

**Dr. Swadesh Kumar Singh**



**BITS Pilani**  
Pilani | Dubai | Goa | Hyderabad

**BIRLA INSTITUTE OF TECHNOLOGY AND SCIENCE, PILANI**

**2020**

**BIRLA INSTITUTE OF TECHNOLOGY AND SCIENCE, PILANI**

**CERTIFICATE**

This is to certify that the thesis entitled **Effect of Processing Routes on Deformation Behaviour and Microstructural Characteristics of Zircaloy-4** and submitted by **Mr. K Limbadri, ID No: 2016PHXF0118H** for award of Ph.D. Degree of the Institute embodies original work done by him under my supervision.



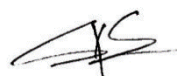
Signature of the Supervisor

Name in capital letters

**Dr. KURRA SURESH**

Designation

**Assistant Professor, BITS Hyd.**



Signature of the Co-supervisor

Name in capital letters

**Dr. SWADESH KUMAR SINGH**

Designation

**Professor, Dean R&D, GRIET, Hyd.**

Date: 25-07-2020

Date:25-07-2020

## ACKNOWLEDGEMENTS

I would like to express my gratitude to my supervisor **Dr. Kurra Suresh** for his strong support, patience and constant availability for technical discussions. I feel motivated and encouraged by his technical discussions. I would like to thank him for being my well-wisher. This thesis is the outcome of the kind co-operation, good-will, technical and beyond technical support extended by **Dr. Swadesh Kumar Singh**, Professor in Mechanical Engineering Department, GRIET, Hyderabad. He provided me an opportunity to use the lab facility available at GRIET.

I am grateful to my doctoral advisory committee members, **Dr. Nitin Ramesh Rao Kotkunde**, Assistant Professor, Department of Mechanical Engineering and **Dr. Ravi Shanker Vidyarthi**, Assistant Professor, Department of Mechanical Engineering for their valuable advices during semester reviews. I am grateful to them for their suggestions in bringing this thesis into final form.

I am grateful to Director Prof. G. Sunder of BITS Pilani Hyderabad campus, for allowing me to carry out my doctoral research work in the institute. I would like to express my sincere thanks to Prof. Vamshi Krishna Venuganti, Associate Dean, AGSRD, Prof. Vidya Rajesh, former Associate Dean and Prof. S. K. Verma, Dean, ARD, BITS Pilani for their continuous support during my research work. I would like to express my sincere thanks to Prof. Amit Kumar Gupta, HOD, Mechanical department for his support during my research work. I am very grateful to DRC convener Dr. Sabareesh Geetha Rajasekharan and his team for monitoring entire procedure of conducting seminars.

I am highly indebted to the **Board of Research in Nuclear Sciences (BRNS)** Govt. of India for their project grant **36(2)/14/56/2014-BRNS/2699** in collaboration with Nuclear Fuel Complex (NFC), Hyderabad, which helped in procuring the test facilities and raw material to conduct this research.

Co-authors in my published papers deserve very special thanks. The valuable inputs from them really helpful for publishing the papers in the reputed international journals and conferences.

I am thankful to my colleagues, Mr. Gangadhar Jella, Mr. Wankhede Pankaj Rambhauji, Mr. Praveen G, Mr. Ahsan ul Haq, Mr. Rakesh and Mr. Mahesh who supported me during my difficult time. I am extremely grateful to all the faculty and staff of Mechanical Engineering Department. I owe special thanks to Materials testing lab technical staff for providing me the cooperation and help during preparation of metallurgical standard specimens. Also, I would like to thank the technical staff at GRIET for their corporation and help during the experimentation.

I would like to thank several colleagues beyond BITS-Pilani University and GRIET who in one way or another contributed in this research. I would like to express my particular gratitude to **Dr. Ashok Kumar Singh**, Scientist G, DMRL, Hyderabad, who helped me in conducting XRD experiments and given valuable inputs in relation to texture. I would like to thank **Prof. Sushanta Kumar Panda** and **Dr K. Sajun Prasad**, for their constant support in conducting formability tests using Hydraulic press facility at Department of Mechanical Engineering, IIT Kharagpur. I would like to thank **K.V. Mani Krishna**, Scientific Officer, BARC, who helped me to get microstructure by EBSD technique. I would like to thank **Dr. V. V. Kutumba Rao**, Former Professor, IIT BHU for sharing part of his invaluable knowledge in tensile test data.

Most of all I would like to thank my wife **Anitha** for her unyielding devotion and love, support, encouragement and quiet patience. I would like to thank my close friends Dr. Prudvi, Gangadhar Jella, Mahesh K, Anupama, Dr. Sunil, who helped me in proof reading of my thesis. My deepest appreciation also goes to my **parents** and their faith in me and allowing me to be as ambitious as I wanted.

## ABSTRACT

In the present work, three different types of Zircaloy-4 materials are used for texture tensile property correlation. They are Slab Route Sheet (SRS), Tube Route Sheet (TRS) and Low Oxygen Sheet (LOS). The SRS and LOS sheet materials have come from rolling route whereas the TRS has come from pilgering route. The chemical composition of the SRS and TRS is same whereas Oxygen content is low in LOS (834ppm).

The microstructure, obtained by EBSD technique, is resulted as all the three sheet materials have equiaxed grains. The XRD patterns of the three materials have same peak pattern of HCP crystal structure. The texture of as received samples are analysed in terms of  $\{0002\}$  basal pole figures and the quantitative study of texture is analysed by Orientation Distribution Function (ODF). The texture intensity variation is also studied in  $[0001] \parallel \text{ND}$  fiber plot. It is resulted that the TRS has maximum texture intensity with  $f(g) = 6.5$ . And the tensile tests at different strain rates of 0.001, 0.005 and  $0.01\text{s}^{-1}$  in three different sample directions (rolling or Longitudinal (L) direction, Transverse (T or  $90^\circ$  to rolling) direction, Radial (R or  $45^\circ$  to rolling) direction) at room temperature are conducted. The tensile property variation with respect to orientation and strain rate is analysed. The anisotropy of tensile properties is captured by calculating the in-plane anisotropy ( $A_{\text{IP}}$ ) and anisotropy index ( $\delta$ ). The moderate values of  $A_{\text{IP}}$  and  $\delta$  are in good agreement with the presence of moderate texture.

Similarly, the orientation dependant tensile properties of Zircaloy - 4 sheet materials are analysed at elevated temperatures by conducting tensile tests at elevated temperatures ( $75^\circ\text{C}$ ,  $150^\circ\text{C}$  and  $225^\circ\text{C}$ ) in three different sample orientations. The tensile properties such as yield stress, and ultimate tensile strengths are decreased with increasing temperature. The yield stress is decreased by changing the sample direction from rolling to the transverse direction. The variation with the orientation of the sample is analysed by calculating the  $A_{\text{IP}}$  and  $\delta$ . The

instantaneous work hardening curves of the materials are showed three different regions similar to room temperature work hardening curves. Furthermore, the temperature effect on the texture of the sample are also analysed and the LOS is showed maximum texture intensity ( $f(g)=17.4$ ) compared to the other two materials. The moderate values of the  $A_{IP}$  and  $\delta$  are in good agreement with the moderate texture present in the three materials.

The calculated tensile stress strain data at room temperature and elevated temperatures are used to calibrate constitutive models for Zircaloy-4. Four different constitutive models such as Johnson Cook (JC), modified-Arrhenius (m-Arr), modified-Zerilli Armstrong (m-ZA) and Khan-Hang-Liang (KHL) models are calibrated to predict flow stress. The predicting capability of the constitutive models is determined by calculating coefficient of correlation ( $R^2$ ) and average absolute error ( $\% \Delta$ ). Among the four constitutive models, the m-Arr is predicting well for the three Zircaloy-4 sheet materials.

In formability of the Zircaloy-4, initially, an experimental forming limit diagram (FLD) for TRS material in rolling direction is constructed. The forming limit curve (FLC) of TRS is indicated that the forming limits are decreasing from tension-compression region to tension-tension region. Finite element simulation is also performed by incorporating experimental FLD as fracture criteria. Furthermore, it is observed that with respect to the orientation of the sample, the formability decreased from rolling direction to transverse by 11.76% at tension-compression region but the variation is not observed in tension-tension region. The formability also studied in terms of limiting dome height and strain distribution profiles of the samples. The experimental FLDs also constructed for SRS material and compared with that of TRS. The correlation between texture and formability of Zircaloy-4 also established. Furthermore, theoretical forming limit diagrams such as Hill-Swift criterion (H-S), Storen-Rice bifurcation criterion (S-R), Bressan and Williams (B-W) model, Hill-Tresca (H-T) model are calibrated for Zircaloy-4 (TRS) material to predict FLC.

# TABLE OF CONTENTS

ACKNOWLEDGEMENTS .....	ii
ABSTRACT.....	iv
TABLE OF CONTENTS.....	vi
LIST OF FIGURES .....	ix
LIST OF ABBREVIATIONS.....	xiv
LIST OF SYMBOLS .....	xv
Chapter 1 .....	1
1.1 Background and Motivation.....	1
1.2 Historical development of Zirconium for reactors.....	3
1.3 Development of Zircaloy-4 .....	4
1.4 Applications and reasons behind them.....	8
1.5 Organization of thesis.....	13
Chapter 2.....	16
2.1 Texture in Zirconium alloys.....	16
2.2 Constitutive models.....	18
2.3 Forming limit diagrams (FLD) and finite element analysis (FEA).....	21
2.4 Research gaps.....	25
2.5 Scope of objectives.....	26
2.6 Methodology .....	28
Chapter 3.....	33
3.1 Introduction .....	33
3.2 Experimental details.....	33
3.2.1 Materials used and its composition .....	33
3.2.2 Experimental procedure of microstructure and texture .....	34

3.2.3 Experimental procedure for tensile tests of SRS, TRS and LOS at room temperature .....	35
3.3 Results and Discussion.....	37
3.3.1 Microstructure and texture study .....	37
3.3.2 Tensile properties of Zircaloy-4 at room temperature.....	40
3.3.3 Anisotropy of Zircaloy - 4 at room temperature and fractography .....	51
3.4 Summary .....	54
Chapter 4.....	56
4.1 Introduction .....	56
4.2 Experimental details .....	56
4.2.1 Materials used.....	56
4.2.2 Experimental procedure of texture analysis at elevated temperatures. ....	57
4.2.3 Experimental procedure for tensile tests at elevated temperatures.....	57
4.3 Results and discussion.....	58
4.3.1 Texture analysis of Zircaloy - 4.....	58
4.3.2 Tensile properties of Zircaloy-4 at elevated temperatures .....	61
4.3.3 Anisotropy of Zircaloy - 4 at room temperature and fractography .....	73
4.4 Summary .....	76
Chapter 5.....	78
5.1 Introduction .....	78
5.2 Experimental details .....	78
5.3 Development of constitutive models.....	79
5.3.1 Johnson Cook (JC) model.....	79
5.3.2 Modified Zerilli-Armstrong (m-ZA) model .....	83
5.3.3 Modified-Arrhenius equation .....	87
5.3.4 Khan-Huang-Liang (KHL) Constitutive modelling .....	92
5.4 Comparison of constitutive models.....	97



5.5 Summary .....	100
Chapter 6.....	102
6.1 Introduction .....	102
6.2 Experimental details.....	102
6.3 Forming limit diagram of TRS in longitudinal direction .....	104
6.4 Finite element modeling and validation of the FLD .....	105
6.5 Limiting dome height.....	107
6.6 Forming limit diagrams of TRS in three sample directions .....	108
6.7 Strain distribution on TRS.....	112
6.8 Comparison of formability of SRS and TRS in three sample directions .....	114
6.9 Comparison of strain distribution.....	118
6.10 Theoretical forming limit diagrams .....	121
6.11 Summary .....	128
Chapter 7.....	131
7.1 Conclusions .....	131
7.2 Specific Contributions to the Research .....	136
7.3 Future Scope of Work .....	136
References.....	137
List of Publications .....	150
Biography.....	151

# LIST OF FIGURES

Fig. 1.1: Fuel bundle assembly showing Spacer grid (Song and Lee 2012).....	2
Fig. 1.2: Flow chart representing the development of zircalloys.....	6
Fig. 1.3: Applications of Zircaloy-4 in nuclear fission reactors .....	9
Fig. 1.4: Schematic view of (a) spacer grid along with its details (b) a unit spacer grid set ..	10
Fig. 2.1: Flow diagram representing tensile tests .....	28
Fig. 2.2: Flow diagram representing calculation of ODF by XRD tests.....	29
Fig. 2.3: Development of constitutive models for Zircaloy-4 material .....	29
Fig. 2.4: Flow diagram representing experimental construction of forming limit diagram ....	30
Fig. 2.5: Flow diagram representing construction of theoretical forming limit diagrams .....	31
Fig. 2.6: Comprehensive methodology .....	32
Fig. 3.1: Schematic diagram of the tensile sample used in the present study.....	36
Fig. 3.2: Electra-50 BISS servo-electric universal testing machine of 50 kN capacity.....	36
Fig. 3.3: Microstructure of the alloys: (A) SRS, (B) TRS and (C) LOS .....	38
Fig. 3.4: XRD patterns of the SRS, TRS and LOS alloys .....	38
Fig. 3.5: Texture of all the three alloys (SRS, TRS and LOS): (a) ODF ( $\varphi_2 = 0^\circ$ and $30^\circ$ sections) and (b) [0001]    ND fibre plots. ....	39
Fig. 3.6: Effect of strain rate on (a) strength (yield and ultimate), (b) uniform elongation, (c) strength coefficient, (d) work hardening exponent. ....	41
Fig. 3.7: Tensile properties of the sample SRS at $0.001 \text{ s}^{-1}$ strain along L, R and T directions: (a) Engineering stress – Engineering strain curves, (b) True stress – True strain curves (c) True stress – True plastic strain and (d) Differential curves.....	43
Fig. 3.8: Tensile properties of the sample SRS at $0.005 \text{ s}^{-1}$ strain along L, R and T directions: (a) Engineering stress – Engineering strain curves, (b) True stress – True strain curves (c) Log True stress – Log True plastic strain and (d) Differential curves.....	44
Fig. 3.9: Tensile properties of the sample SRS at $0.01 \text{ s}^{-1}$ strain along L, R and T directions: (a) Engineering stress – Engineering strain curves, (b) True stress – True strain curves (c) Log True stress – Log True plastic strain and (d) Differential curves.....	45
Fig. 3.10: Tensile properties of the sample TRS at $0.001 \text{ s}^{-1}$ strain along L, R and T directions: (a) Engineering stress – Engineering strain curves, (b) True stress – True strain curves (c) Log True stress – Log True plastic strain and (d) Differential curves...	46

Fig. 3.11: Tensile properties of the sample TRS at 0.005 s <sup>-1</sup> strain along L, R and T directions: (a) Engineering stress – Engineering strain curves, (b) True stress – True strain curves (c) Log True stress – Log True plastic strain and (d) Differential curves...	47
Fig. 3.12: Tensile properties of the sample TRS at 0.01 s <sup>-1</sup> strain along L, R and T directions: (a) Engineering stress – Engineering strain curves, (b) True stress – True strain curves (c) True stress – True plastic strain and (d) Differential curves.....	48
Fig. 3.13: Tensile properties of the sample LOS at 0.001 s <sup>-1</sup> strain along L, R and T directions: (a) Engineering stress – Engineering strain curves, (b) True stress – True strain curves (c) Log True stress – Log True plastic strain and (d) Differential curves...	49
Fig. 3.14: Tensile properties of the sample LOS at 0.005 s <sup>-1</sup> strain along L, R and T directions: (a) Engineering stress – Engineering strain curves, (b) True stress – True strain curves (c) True stress – True plastic strain and (d) Differential curves.....	50
Fig. 3.15: Tensile properties of the sample LOS at 0.01 s <sup>-1</sup> strain along with L, R and T directions: (a) Engineering stress – Engineering strain curves, (b) True stress – True strain curves (c) True stress – True plastic strain and (d) Differential curves.....	51
Fig. 3.16: The fracture surface of SRS tensile samples along L direction with different strain rates: (a) 0.001, (b) 0.005 and (c) 0.01 s <sup>-1</sup> .....	53
Fig. 3.17: The fracture surface of TRS tensile samples along L direction with different strain rates: (a) 0.001, (b) 0.005 and (c) 0.01 s <sup>-1</sup> .....	53
Fig. 3.18: The fracture surface of LOS tensile samples along L direction with different strain rates: (a) 0.001, (b) 0.005 and (c) 0.01 s <sup>-1</sup> .....	54
Fig. 4.1: Texture of SRS in terms of ODF sections ( $\varphi_2 = 0^\circ$ and $30^\circ$ ) and test temperatures (348K and 423K). .....	58
Fig. 4.2: Texture of TRS in terms of ODF sections ( $\varphi_2 = 0^\circ$ and $30^\circ$ ) and test temperatures (348K and 423K). .....	59
Fig. 4.3: Texture of LOS in terms of ODF sections ( $\varphi_2 = 0^\circ$ and $30^\circ$ ) and test temperatures (348K and 423K). .....	59
Fig. 4.4: Texture terms of [0001]   ND fibre plots at different temperature: (a) SRS, (b) TRS and (c) LOS.....	60
Fig. 4.5: Effect of temperature on (a) strength (yield and ultimate), (b) uniform elongation, (c) strength coefficient, (d) work hardening exponent.....	63

Fig. 4.6: Tensile properties of SRS sample at 348K along L, R and T directions: (a) Engineering stress – Engineering strain curves, (b) True stress – True strain curves (c) Log True stress – Log True plastic strain and (d) Differential curves.....	64
Fig. 4.7: Tensile properties of SRS sample at 423K along L, R and T directions: (a) Engineering stress – Engineering strain curves, (b) True stress – True strain curves (c) Log True stress – Log True plastic strain and (d) Differential curves.....	65
Fig. 4.8: Tensile properties of SRS sample at 498K along L, R and T directions: (a) Engineering stress – Engineering strain curves, (b) True stress – True strain curves (c) Log True stress – Log True plastic strain and (d) Differential curves.....	67
Fig. 4.9: Tensile properties of TRS sample at 348K along L, R and T directions: (a) Engineering stress – Engineering strain curves, (b) True stress – True strain curves (c) Log True stress – Log True plastic strain and (d) Differential curves.....	68
Fig. 4.10: Tensile properties of TRS sample at 423K along L, R and T directions: (a) Engineering stress – Engineering strain curves, (b) True stress – True strain curves (c) Log True stress – Log True plastic strain and (d) Differential curves.....	69
Fig. 4.11: Tensile properties of TRS sample at 498K along L, R and T directions: (a) Engineering stress – Engineering strain curves, (b) True stress – True strain curves (c) Log True stress – Log True plastic strain and (d) Differential curves.....	70
Fig. 4.12: Tensile properties of LOS sample at 348K along L, R and T directions: (a) Engineering stress – Engineering strain curves, (b) True stress – True strain curves (c) True stress – True plastic strain and (d) Differential curves.....	71
Fig. 4.13: Tensile properties of LOS sample at 423K along L, R and T directions: (a) Engineering stress – Engineering strain curves, (b) True stress – True strain curves (c) Log True stress – Log True plastic strain and (d) Differential curves.....	72
Fig. 4.14: Fig. 4.13: Tensile properties of LOS sample at 498K along L, R and T directions: (a) Engineering stress – Engineering strain curves, (b) True stress – True strain curves (c) Log True stress – Log True plastic strain and (d) Differential curves.....	73
Fig. 4.15: The fracture surface of SRS tensile samples along longitudinal direction at: (a) 348K, (b) 423K and (c) 498K.....	75
Fig. 4.16: The fracture surface of TRS tensile samples along longitudinal direction at: (a) 348K, (b) 423K and (c) 498K.....	75
Fig. 4.17: The fracture surface of LOS tensile samples along longitudinal direction at: (a) 348K, (b) 423K and (c) 498K.....	76

Fig. 5.1: True stress predicted from Johnson Cook model and experimental stress at various strains for different strain rates of (a) $0.001s^{-1}$ (b) $0.005s^{-1}$ (c) $0.01s^{-1}$ for LOS material..	82
Fig. 5.2: True stress predicted from modified Zerilli-Armstrong and experimental stress at various strains for different strain rates of (a) $0.001s^{-1}$ (b) $0.005s^{-1}$ (c) $0.01s^{-1}$ For LOS material. ....	84
Fig. 5.3: True stress predicted from modified-Arrhenius and experimental stress at various strains for different strain rates of (a) $0.001s^{-1}$ (b) $0.005s^{-1}$ (c) $0.01s^{-1}$ for LOS material..	90
Fig. 5.4: The true stress estimated using KHL model and experimental true stress at various strains and strain rates of (a) $0.001s^{-1}$ , (b) $0.005s^{-1}$ , and (c) $0.01s^{-1}$ for LOS material. ....	93
Fig. 5.5: The true stress estimated using KHL model and experimental true stress at various strains and strain rates of (a) $0.001s^{-1}$ , (b) $0.005s^{-1}$ , and (c) $0.01s^{-1}$ for SRS material.....	94
Fig. 5.6: The true stress estimated using KHL model and experimental true stress at various strains and strain rates of (a) $0.001s^{-1}$ , (b) $0.005s^{-1}$ , and (c) $0.01s^{-1}$ for TRS material.....	95
Fig. 5.7: Coefficient of correlation of (a) JC, (b)m-ZA, (c) m-Arr and (d) KHL for LOS.....	99
Fig. 6.1: Schematic diagram of (a) LDH test facility with tooling, (b) specimen geometries, and (c) samples cut along different orientation with respect to the sheet rolling direction. ....	103
Fig. 6.2: (a) Deformed stretch formed specimens, and (b) forming limit diagram of the material. ....	104
Fig. 6.3: Finite element model of stretch forming process. ....	106
Fig. 6.4: FE predicted cups of (a) sample 1, (b) sample 2, and (c) sample 3 at time step when the deformation path intersects the experimental FLD.....	107
Fig. 6.5: Deformed stretch formed specimens along rolling direction of the sheet.....	108
Fig. 6.6: Forming limits of Zirconium-4 alloy along (a) rolling, (b) diagonal, and (c) transverse direction of the sheets. ....	110
Fig. 6.7: Forming limits comparison along rolling, diagonal, and transverse direction of the sheet. ....	111
Fig. 6.8: Strain distribution profile of 25mm width Hasek specimen along (a) rolling, (b) diagonal, and (c) transverse orientation with respect to rolling direction of sheet. ....	112
Fig. 6.9: Strain distribution profile along rolling direction for (a) dry condition, and (b) lubricated condition of 150mm circular blank.....	114
Fig. 6.10: Stretch formed specimens deformed along different strain paths for rolling direction of the sheet.....	115

Fig. 6.11: Forming limits of slab-route processed Zirconium-4 alloy along (a) rolling, (b) diagonal, and (c) transverse direction with respect to the rolling direction of the sheets. .....	117
Fig. 6.12: Forming limit comparison between(a) Tube Route Sheet (TRS) and (b) Slab Route Sheet (SRS) Zirconium alloy along three direction of the sheets.....	118
Fig. 6.13: Strain distribution profile of SRS sample 1 along (a) rolling, (b) diagonal, and (c) transverse orientation with respect to rolling direction of sheet.....	119
Fig. 6.14: Strain distribution profile of TRS sample 1 along (a) rolling, (b) diagonal, and (c) transverse orientation with respect to rolling direction of sheet.....	119
Fig. 6.15: Strain distribution profile of SRS sample along rolling direction for (a) sample 2, and (b) sample 3.....	120
Fig. 6.16: Strain distribution profile of TRS sample along rolling direction for (a) sample 2, and (b) sample 3.....	121
Fig. 6.17: Comparison of theoretical FLDs with experimental FLDs. ....	128

## LIST OF ABBREVIATIONS

SRS: Slab Route Sheet  
TRS: Tube Route Sheet  
LOS: Low Oxygen Sheet  
HCP: Hexagonal close packed crystal structure  
ASTM: American Society for Testing and Materials  
UTM: Universal testing machine  
LDH: Limiting Dome Height  
RT: Room temperature  
FLD: Forming limit diagram  
FLC: Forming limit curve  
BHF: Blank-holding force  
SEM: Scanning electron microscope  
EBSD: Electron Back Scatter Diffraction  
XRD: X-ray diffraction  
ODF Orientation Distribution Function  
BISS: Bangalore integrated system software  
JC: Johnson Cook model  
m-Arr.: Modified Arrhenius model  
m-ZA: Modified Zerilli Armstrong model  
KHL: Khan-Hang-Liang  
H-S: Hill-Swift criterion,  
SR: Storen-Rice criterion,  
BW: Bressan – Williams Model  
HT: Hill-Tresca Model  
M-K: Marciniak Kuczynski

## LIST OF SYMBOLS

$r_n$	: Normal anisotropy
$\Delta r$	: Planer anisotropy
$E$	: Modulus of Elasticity
$v$	: Cross head speed
$\varepsilon_p$	: Plastic strain
$Q$	: Activation energy
$R$	: Universal gas constant
$Kb$	: Boltzmann constant
$\Delta$	: Average absolute error
$\rho$	: Density
$A_{IP}$	: In-plane anisotropy
$\delta$	: Anisotropy index
$\% \varepsilon_U$	: Percentage uniform elongation
$T$	: Transverse
$L$	: longitudinal
$v$	: Crosshead velocity
$L$	: Gauge length of specimen
$t$	: Time
$\dot{\varepsilon}$	: Strain rate
$\dot{\varepsilon}_0$	: Reference strain rate
$\varepsilon$	: True plastic strain
$\dot{\varepsilon}$	: True plastic strain rate
$K$	: Strength Coefficient
$n$	: Strain hardening Exponent
$R^2$	: Coefficient of Correlation
$\mu$	: Shear Modulus
$m$	: Thermal softening exponent
$T^*$	: Homologous temperature
$T_a$	: Absolute temperature,
$T_{ref}$	: Reference temperature,



$T_m$	: Melting temperature
$A$	: Yield stress at reference temperature
$\Delta$	: Average absolute error
$\sigma$	: Flow stress
$\sigma_{exp}$	: Experimental stress
$\sigma_p$	: Predicted stress
$\sigma_1$	: True major principal stress
$\sigma_2$	: True minor principal stress
$\sigma_{ut}$	: Ultimate tensile strength
$\sigma_a$	: Thermal component
$\sigma_i$	: Intrinsic stress component
$\sigma_m$	: Mean stress
$\tau_{cr}$	: Critical shear stress
$\sigma_T$	: Tresca stress at plain strain condition.
$N$	: Total number of data points
$A_0$	: Thermal component of yield stress
$C_1$	: Yield stress at reference temperature
$\eta$	: Triaxiality
$\varepsilon_p$	: Plastic strain
$Z$	: Zener-Hollomon parameter
$r_\theta$	: Anisotropy constant
$e_1$ :	: Major engineering strains
$e_2$	: Minor engineering strains
$M$	: Integer exponent
$\varphi_1, \Phi, \varphi_2$	: Euler angles

# Chapter 1

## Introduction

### 1.1 Background and Motivation

A nuclear reactor is a device where a self-sustained nuclear chain reaction is controlled. This device is used in nuclear power plants for production of electricity and in the ships for propulsion. In the reactor, heat is generated by the process of nuclear fission, and it will be transferred to the water. The water is then converted to pressurized steam, and thereafter, turbines are rotated by the steam to produce electricity.

In the nuclear industry, the reaction that takes place in the core is the nuclear fission or in other words, the chain reaction of a bombardment of neutrons on a Uranium nucleus. The core consists of three main components, namely fuel bundle, control pads and moderator. The first one, fuel bundle, is a number of pipes placed closely and they are filled with Uranium fuel in the form of pellets. The second is control pads, generally made of Boron, to absorb excess neutrons for controlling the nuclear reaction. The remaining is the moderator that carries the heat generated from a nuclear reaction. Now, the fuel bundles must sustain the irradiation of neutrons, should not undergo corrosion due to contact with high-temperature water and should not absorb neutrons which are required for the nuclear reaction. Therefore, suitable material for the fuel cladding tube is the one which has less thermal neutron absorption cross-section (Krishnan and Asundi 1981). Neutron absorption cross-section is a measure of the area of nuclei cross-section indicating the probability of absorption of neutrons, and high corrosion resistance (Xu et al. 2000).

Like other metals, Fe (2 barns), Ni (3 barns), Au (98.7 barns) the Zirconium also has high neutron cross-section but later on it was discovered that pure Zirconium absorbs very few neutrons. The natural Zirconium contains 2% Hafnium causing the Zirconium to have the high

neutron cross-section. Further, Kaufman at MIT and Pomarance at Oak-Ridge came up with a laboratory test to separate the Hafnium from Zirconium. Also, they proved that Zirconium in pure stage ( $< 0.02\%$  hafnium) absorbs fewer neutrons, that is 600 times less than that of natural Zirconium, figuratively 0.006 barns (K. Shibata et al. 2011). From then, Zirconium was selected for manufacturing the fuel clad tubes, and later on for better improvements in corrosion resistance and mechanical properties, the development of Zirconium alloys was started.

In reactor core, the fuel bundle is an assembly of fuel rods. The fuel is Uranium-235 or Plutonium-239. The fuel is filled in the form of fuel pallets in pipes of diameter about 1cm, thickness 1mm and length is about 4 meters, called fuel rods. The fuel rods are assembled together with the help of spacer grid assembly, as shown in Fig. 1.1 (K. Song and Lee 2012). All the structural materials of the fuel assembly are manufactured by Zirconium alloys.

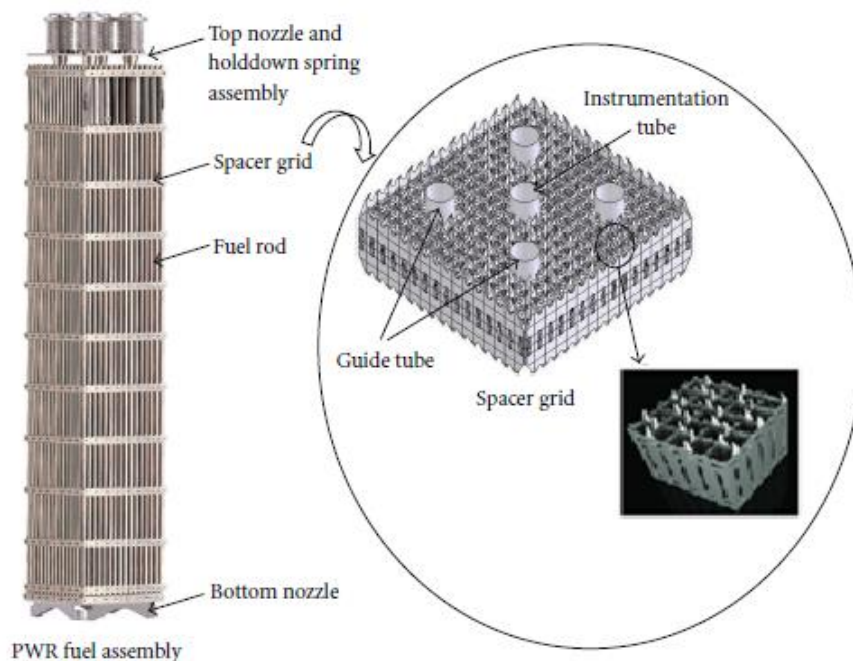


*Fig. 1.1: Fuel bundle assembly showing Spacer grid (Song and Lee 2012).*

Nuclear Fuel Complex, Hyderabad, India, uses three types of Zircaloy-4 (one of the latest Zirconium alloys) sheet materials for stamping contacting areas of the spacer grids. The

three types are Slab Route Sheet (SRS), which is normally rolled sheet, Tube Route Sheet (TRS), which is obtained from pilgering route and Low Oxygen Sheet (LOS), which is similar to SRS but with low Oxygen content. During the stamping, contacting areas (dimples and spring) of spacer grid was failed. This has led to thinking over the formability aspects and metallurgical reasons for the failures. The formability of sheet materials can be understood by constructing forming limit diagrams. Furthermore, The Zirconium has an hexagonal close packed (hcp) crystal structure and therefore, it has a limited activation slip system during deformation. This has further led towards thinking about the anisotropy and texture of the material, which may induce failure during the forming of the sheet material.

## **1.2 Historical development of Zirconium for reactors**

In 1975, Admiral Rickover (Rickover, Geiger, and Lustman 1975) was in charge of developments of ships and submarines in the US Navy. He envisioned a reactor to move the ships when they were rolling or pitching, also when the submarines were surfacing or diving. Therefore, a metal was required to construct the reactor. The metal was required with high-temperature corrosion resistant, less neutron absorption which needs for a nuclear chain reaction and with required structural integrity. The availability of the material and cost was also other considerations. Stainless steel, Beryllium and Aluminium were all proved to be the disadvantage against their usage. Initially, the Zirconium was also showed high absorption of neutrons but high number of neutrons are needed in nuclear fission. Zirconium cost was too high, and availability was less. Later on, it was found that the naturally obtained Zirconium has 2% Helium which was the cause for the high absorption of the neutrons. A process was established to remove the Helium from the Zr. Then the pure Zirconium was the best choice for Admiral Rickover to construct the reactor(Murty and Charit 2006a).

The Zirconium was chosen by the US Navy, but there were no standards set (Krishnan and Asundi 1981). The only standards essential were the Zirconium should be as pure as

possible, and it must be as strong as possible. Therefore, the choice fell on the crystal bar process to produce high purity Zirconium. It is a vaporization technique; therefore, Iodine reacts with impure Zirconium, and then the composite is decomposed at 1673K. After the decomposition, the pure Zirconium is deposited on a film. The pure Zirconium is called crystal bar due to the surface brightness. Then the crystal bar was subjected to high temperature corrosion resistance tests. A confused test behaviour was found in the crystal bar corrosion tests. It was due to unexpected culprit elements in the crystal bars. Then the next step went to choose a pure grade of sponge Zirconium as source for making the crystal bar. Instead of the crystal bar process a higher-grade process called Kroll process was selected for making the very pure crystal bar.

Contrary to the expected results, the impure crystal bars showed higher corrosion resistance than that of the pure crystal bars. At this stage, the attention of the scientific community went on to add known elements to Zirconium to make alloys for high corrosion resistance. This was the beginning of development of Zirconium alloys.

### **1.3 Development of Zircaloy-4**

As it was discussed in the earlier chapter that the Kroll bar process of Zirconium metal gave unexpected results such as the pure crystal bar has less corrosion resistance than that of the impure crystal bar. Therefore, the focus shifted to the development of Zirconium alloys for structural elements in the reactor core. The first step in developing Zirconium alloys was to identify the alloying elements. After intensive investigation, Tin was selected as the alloying element because it improved the corrosion resistance without affecting the neutron absorption cross section. Initially, even though it was taken as 5wt% but later on it was decided to 2.5wt% with a good agreement among corrosion resistance, strength, and fabricability. This was called as Zircaloy-1. The Zircaloy-1 samples were subjected to long term corrosion resistant tests. Unexpectedly, an unusual trend was observed in the test. Instead of decreasing corrosion rate

after certain time, it was increased and had come to a constant trend. This corrosion rate was comparable with formation of white non-adherent oxide layer on unalloyed sponge. Therefore, immediately the processing of Zircaloy-1 was stopped.

A melter in Bettis fabrication shop melted Zircaloy-1 and accidentally it got contaminated by stainless steel. The resultant component has high corrosion resistance. At the same time, effect of Iron additives on the corrosion resistance of Zircaloy-1 was established. Therefore, the next step was to choose a composition that would give high corrosion resistance. Thus, Iron content was selected as 0.15% due to the range of Iron content present in the sponge Zirconium. A 0.05% Nickel content was chosen due to its beneficial effect of high temperature corrosion resistance. The Bettis Melter's component picked up the Chromium content of 0.10%, therefore the Chromium content was kept to be same. To counteract the deleterious effects of Nitrogen, Nickel content was chosen as 0.05%. This was designated as Zircaloy-2. The Zircaloy-2, compared to that of Zircaloy-1, had equal tensile properties and better corrosion resistance.

The Zircaloy-2 samples were subjected to high temperature corrosion tests and the results were satisfactory. Even though the Zircaloy-2 had adequate corrosion resistance, there was a fear of ill effect of the high content of Tin which was experienced in the case of Zircaloy-1. Therefore, as an attempt to develop a highest corrosion resistant alloy among the family of Zircaloys, the Tin content was decreased to 0.25% and Iron content was increased to 0.25%. This new alloy was referred as Zircaloy-3. The Zircaloy-3 samples were subjected to high temperature corrosion tests and unexpectedly a network of white corrosion surface was found. Later on, it was identified as a net-work of Fe-Cr intermetallic. This was due to the manufacturing defect. While manufacturing the Zircaloy-3 the temperature went in to the two-phase range (alpha pulse beta). In the process of eliminating the intermetallic compounds, instead of using the induction melting method, a vacuum arc melting method has been

introduced. In this way the complete intermetallic compounds were eliminated. The resultant alloy, however, did not have sufficient mechanical strength and led to its abandonment. Then the interest went back to the composition of Zircaloy-2.

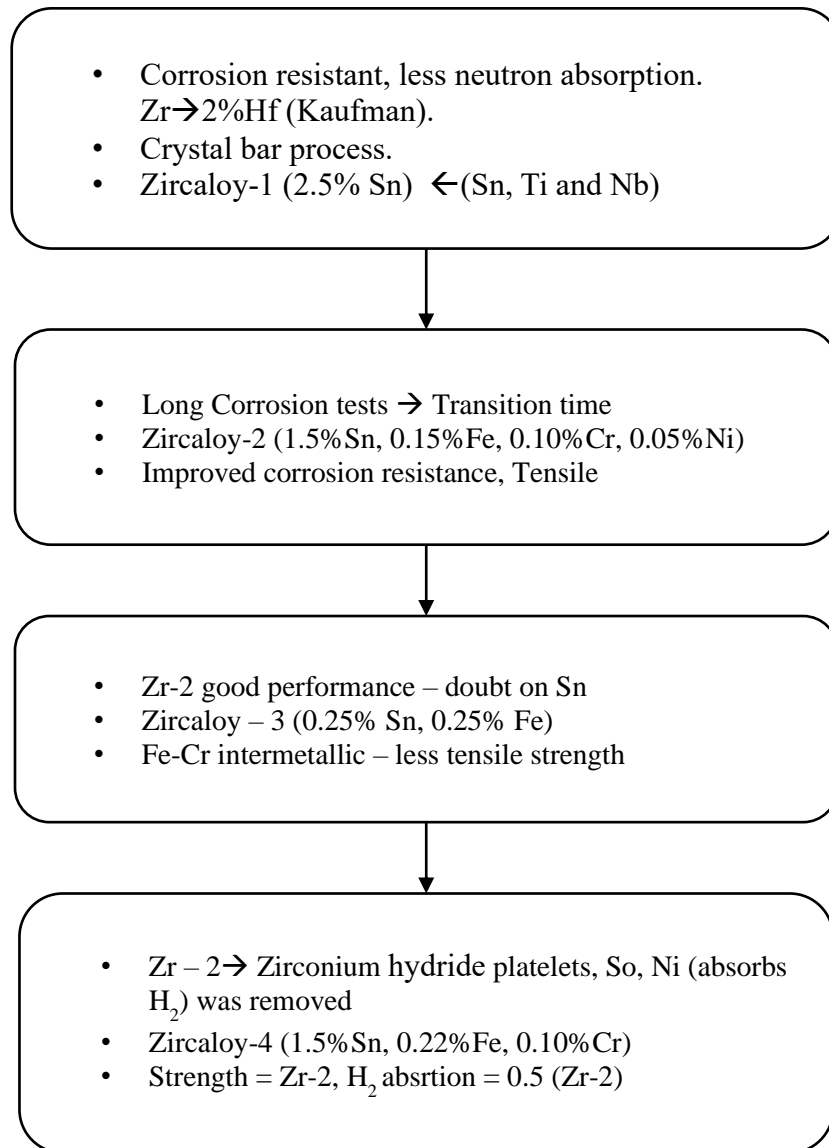


*Fig. 1.2: Flow chart representing the development of Zircalloys*

*Table 1.1: Chemical composition of Zircalloys*

Alloys	Composition elements in weight %			
	Tin	Iron	Chromium	Nickel
Zircaloy-1	2.5	-----	-----	-----
Zircaloy-2	1.5	0.12	0.10	0.05
Zircaloy-3	0.25	0.25	-----	-----
Zircaloy-4	1.5	0.22	0.10	-----

Right at this point of time, the embrittlement of Zircalloys due to Hydrogen was found. The sample, which had crystallographically oriented Zirconium hydrides, showed lower impact strength than that of the normal samples. Therefore, the Hydrogen content in Zirconium was restricted to 250ppm. Furthermore, accidentally, during the development of fuel element by eutectic diffusion bonding method, it was found that the Zircaloy-2 which was coated with Nickel absorbed an adequate amount of Hydrogen. Therefore, the decision was made to eliminate the 0.05% Nickel from the Zircaloy-2. Then these alloys were called as ‘Nickel free Zircaloy-2’. However, the Nickel free Zircaloy-2 did not have sufficient corrosion resistance. Therefore, the next choice was to increase the Iron content. Thus, a new alloy with the composition of 0.18% - 0.24% Fe, 1.5% Sn and 0.10% Cr called as Zircaloy-4 has been made. The chemical composition of the Zircalloys is given in Table 1.1. The development of Zircalloys is also presented in the form of flow chart (Fig.1.2).



In summary, the name “Zircaloy” was coined in the early days at the Bettis Laboratories of the Naval Nuclear Propulsion Program, and now generally represents the commercial alloys of Zirconium where Tin, Iron, Chromium and Nickel are the major alloying elements(Lustman 1979). The purpose of adding the alloying elements is to improve its mechanical properties and corrosion resistance at elevated temperatures(Kass 1964). The two major commercial Zirconium alloys used in current reactors are Zircaloy-2 and Zircaloy-4. The Zircaloy-2 and Zircaloy-4 are used as fuel element cladding and channel box structural material in boiling water reactors (BWRs), respectively(Eyler 1981). In addition, the Zircaloy-4 is also used as fuel element cladding in Pressurized Water Reactors (PWRs) and spacer grid structural material in Light Water Reactors (LWRs)(Fuloria et al. 2016). The main difference in alloying elements of both the alloys is the element Ni in Zircaloy-2 is replaced by Fe in Zircaloy-4. This has resulted in improved resistance to Hydrogen absorption under pressurized heavy water reactors (PHWR). The Zircaloy-4 is one of the promising structural alloys in nuclear industry due to its elevated temperature corrosion resistance(A. Shibata et al. 2016), low thermal neutron absorption cross section (Nagase and Fuketa 2006) and high creep strength (Cappelaere et al. 2012). Therefore, it is used as fuel cladding tubes for storing Uranium oxide pellets and the ends of tubes are sealed with resistance butt welding(Setty, Ravinder, and Murthy 2008). It is also used for manufacturing spacer grid assembly and other structural elements in nuclear industry.

#### **1.4 Applications and reasons behind them**

The Zircaloy-4 is used in various fission reactors. It is used in both light and heavy water type reactors. For example, in BWRs, it is used as fuel cladding tubes, spacer grids, and top and bottom nozzles (shown in Fig. 1.3). In pressurized heavy water reactors, it is used as 'pressure' and 'calandria' tubes. In boiling water reactors (BWR) it is in the form of channel box. During the manufacturing of the fuel cladding tubes, a cylindrical slab of Zircaloy-4 is

converted in to a thin tube. The spacer grid in LWR consists of an array of grid cells. In each cell, sheet metal is bent three times perpendicularly to form rectangular shape. Further, each strip between the bents is subjected to series of projections to enclose the cladding tubes in correct location with friction grip as shown in Fig. 1.4. The spacer grids, by supporting the structural integrity of the cladding tubes, increases the life time of the plant and therefore it is the main component in LWR (K. N. Song, Lee, Shin, et al. 2010). In the same way, the sheet material in channel box application also is subjected to severe deformation processes. All the above-mentioned applications are due to main properties of Zircaloy-4: high temperature water corrosion resistance, high neutron economy as well as good mechanical properties.

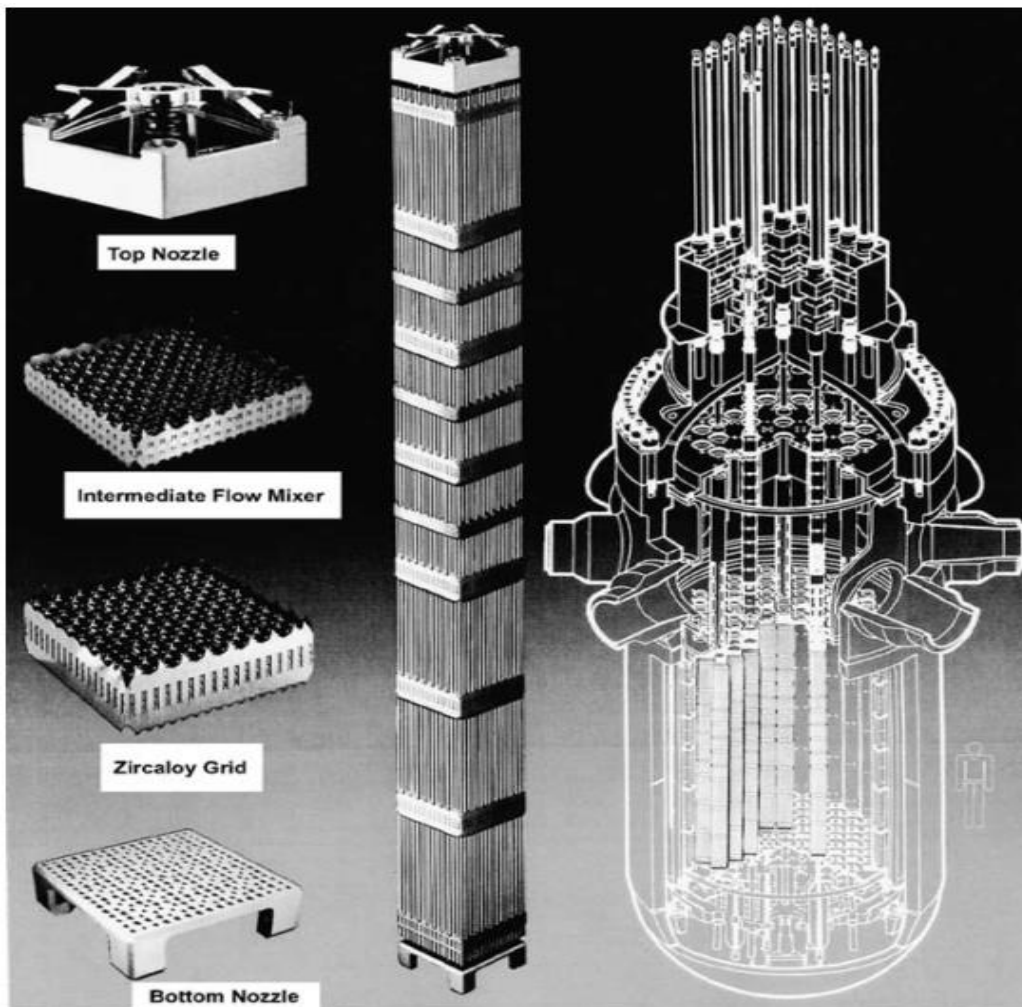


*Fig. 1.3: Applications of Zircaloy-4 in nuclear fission reactors*

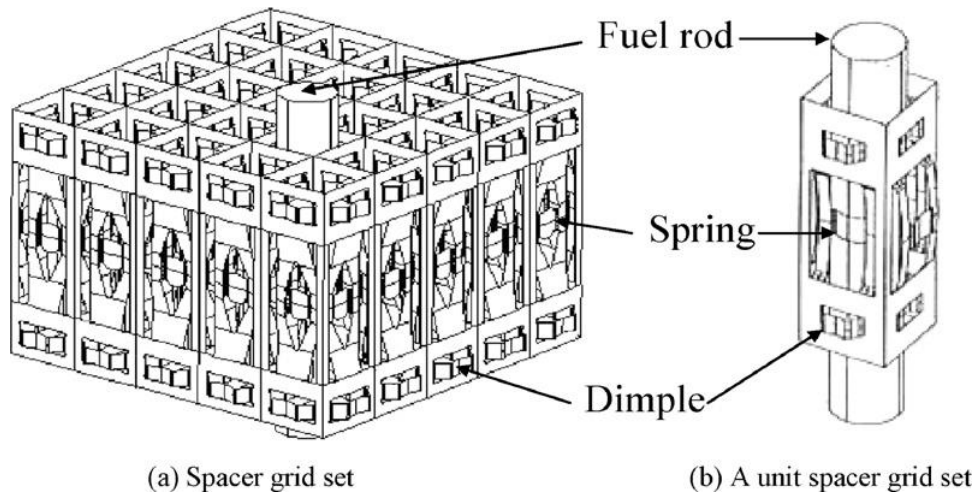


*Fig. 1.4: Schematic view of (a) spacer grid along with its details (b) a unit spacer grid set*

B. Cox (Cox 2005) extensively studied the mechanics behind the corrosion of the Zircaloy-4. The fast neutron irradiation damage alters the corrosion rate by redistributing the Iron element into a meta-stable solid solution. Therefore, the alloys which have low Iron content or the alloys where the Iron is locked in secondary phases show very less acceleration of corrosion. The corrosion film  $ZrO_2$  is independent of the effect of radiolytic radical elements and it may be dependent on redox potentials of metals present in Zircaloys. In PWRs, boric acid does not concentrate to the extent of the LiOH due to the large size of the Boron atoms and therefore it accelerates the corrosion. Furthermore, the galvanic and crevice corrosions on the Zircaloys were analyzed systematically.

These alloys are used in nuclear reactors in the form of thin-wall tubing and the sheet form to fabricate various core internals such as spacer grids for light water reactors and channel boxes. These forms of tubes or plates/sheets are commonly fabricated using thermo mechanical process that involve hot deformation (forging, extrusion and rolling) followed by heat treatments (Tenckhoff 2005). In general, cold rolling and solution treatment of hot rolled material is employed to fabricate tubes (Murty and Charit 2006a). Further, the stress-strain condition in tube reduction processes and rolling process is same when the reduction ratio (thickness to diameter ratio) is more than one (Ballinger, Lucas, and Pelloux 1984). It is known

that each stage of thermo mechanical processing either modifies or introduces crystallographic texture in the material. This has strong bearing in orientation dependent physical and mechanical properties of the materials. The spacer grid is an enclosure for the fuel tubes. The perpendicular bends and series of projections in the grid are critical points where material may fail due to work hardening of the material during deformation. Recently, the grid assembly design has numerically optimized(K. Y. Kim and Seo 2005). Crush strength and integrity of fuel rod support was tested to suggest a suitable new form and manufacturing methodology(K. N. Song, Lee, SHIN, et al. 2010).

In both cases, the grid strips and fuel cladding tubes, the Zircaloy-4 sheets require metallurgical structural integrity to enhance its performance. The microstructural changes follow a sequence with steps involved in manufacturing process. The sequence was observed as dendritic structure (after casting), widmanstatten structure (after  $\beta$  – quench), Bimodal grain size structure (after hot extrusion), heterogeneous deformed structure (after pilgering) and partial recrystallized structure (after annealing)(Tonpe and Kamachi Mudali 2017). Therefore, strength and ductility of the material varies with the grain refinement of the material. The Zircaloy-4 at elevated temperature capture Hydrogen from water and forms hydrides. The mechanism of formation of hydride blisters was studied(Long et al. 2017). The manufacturing methods and annealing temperature affects the texture of the Zirconium alloys. Annealing twins and dislocation density during deformation of the materials were observed as the main reason in evolution of texture(Xia et al. 2016). Little amount of Hydrogen (Tung, Chen, and Tseng 2016), silicon (Hong, Kim, and Lee 2002), proton irradiation (Sarkar et al. 2016) and Hydrogen isotopes (Bind, Sunil, and Singh 2016), affect the mechanical properties of the Zirconium alloys. Furthermore, the Zirconium acts as an electro deposition element (Vacca et al. 2016). Zircaloy-4 forms intermetallic compounds with 304L stainless steel during diffusion (Taouinet, Kamel, and Lebaili 2013). The hydrides on the surface of the sheet material acts as

crack initiation points and eventually the material failure occurs. Therefore, improve-EDC tests with pre-existing crack on the surface of the material were performed to analyze failures of the cladding tubes (Hiroaki Abe et al. 2015). Most of these applications, the Zircaloy-4 is used in the form of sheet material. Therefore, it is important to know the formability of the sheet material.

Formability is the ability of the material to plastically deform without any physical damage (necking and fracture). Forming Limit Diagram (FLD) is the one from which the formability of the material can be observed at all strain conditions of the material such as tension-tension, tension-compression, and plane strain case. The FLD is a curved line diagram with horizontal reference line for the measure of minor strains whereas the vertical reference line for the measure of major strain of the material. In addition, the curve joining the necking points in each strain paths in the FLD is called as Forming Limit Curve (FLC). The condition of forming above the FLC is considered as a failure whereas the condition of forming below the FLC is a safe zone. The Forming Limit Strain (FLS) is the strain at which the sheet material can bear the load without any localized necking and the FLC provides the FLS. The FLC depends on the plastic properties such as strain-rate sensitivity, directional dependent fracture strain and in-plane anisotropy. The shape of the FLC changes with the strain rate sensitivity: limit strain increases with increase in small amount of strain rate sensitivity (Zdzisław Marciniak, Kuczyński, and Pokora 1973). However, the strain based FLD's depends on loading-path. Therefore, the strain based FLD's are used only for proportional loading. Therefore, in two-step stamping processes the data points of necking or fracture may fall below the FLC or the points which come from safe region may fall above the FLC. Nevertheless, the strain measurements are easier than that of stress and therefore the strain based FLDs have become more popular in scientific community while judging the formability limits of materials.

## 1.5 Organization of thesis

The complete thesis is organized in seven different chapters.

**Chapter 1:** This chapter gives an overview of the entire thesis. It begins with motivation and background of the work and continues with the historical development of Zirconium, finally, ends with the methodology adopted for the research.

**Chapter 2:** This chapter enables us to understand work done by the scientific community from the beginning of the development of Zirconium alloys to their formability. It elaborates the texture evolution in the materials, tensile properties importance, dependence of tensile properties on strain rate and temperature, calibration of constitutive models and their predicting capacity. Furthermore, it explores the construction of forming limit diagrams for different materials and their importance. And also, it gives information about the theoretical construction of forming limit diagrams.

**Chapter 3:** This chapter gives detailed information about the tensile properties of the three types of Zircaloy-4 materials in three different sample directions at room temperatures. Also, the material properties such as yield strength, ultimate tensile strength, percentage elongation, strength coefficient, strain hardening exponent, planar anisotropy, anisotropy index are determined from the raw data obtained from the tensile tests. Furthermore, their variation with strain rate and sample direction are also studied. The tensile flow behaviour in terms of engineering stress – engineering strain, true stress – true strain, true stress – true plastic strain and derivative curves are studied very extensively. The texture and microstructure of the material are explained. Finally, the correlation between texture and tensile property variation is established.

**Chapter 4:** In this chapter, the orientation-dependent tensile properties at elevated temperature are determined. Similar to chapter 3, texture at elevated temperature is investigated. Initially,

tensile properties such as yield strength, ultimate tensile strength, percentage elongation, strength coefficient, strain hardening exponent, yield stress-dependent planar anisotropy constant, percentage elongation dependent anisotropy index is determined. The tensile properties variation with respect to the temperature and sample orientation is analyzed.

**Chapter 5:** In this chapter, stress-strain data is taken as input data to calibrate constitutive models such as Johnson-Cook (JC), Modified Zerilli Armstrong (m-ZA), modified Arrhenius (m-Arr) and KHL model. Initially, material constants of all the models are determined for all the three materials (SRS, TRS and LOS). Thereafter, by substituting the material constants, the predicted data is generated. The predicted data is validated with experimental data. Furthermore, the prediction capability of each model is determined and compared among themselves. The best suitable model among the four models is selected for better prediction of flow stress.

**Chapter 6:** In this chapter, experimental FLDs are plotted for both SRS and TRS samples. Nakajima test samples are cut from both SRS and TRS materials to conduct limiting dome height test. 5 mm dia circular grids are then screen printed to measure the strain of the material in two directions. Then the Limiting dome height test is performed on both the materials. Initially, FLDs of TRS are constructed, limiting dome height is measured and also Finite element validation is performed. Then it is extended to construct in three sample directions of TRS and SRS. Strain distribution of the material on samples is also measured with respect to curve linear distance from the pole. Finally, the forming limit diagrams and strain distribution of the TRS and SRS are compared.

**Chapter 7:** In this chapter, the essence of each chapter is extracted and presented as a salient conclusion of the entire work.

In summary, Zirconium was selected for nuclear industry structural applications due to its neutron economy. Even though initially it was thought that pure Zirconium is well suited but later experiments proved that Zirconium alloys give better performance. Then, the Zircaloy-4 stood best among the Zircaloys. In the next chapter, different aspects of Zircaloy-4 such as texture, constitutive models and formability are reviewed from the existed literature.



# Chapter 2

## Literature Review

Texture development in Zircalloys is imperative for two reasons: (i) the texture evolved at any strain step will get modified during successive strain increments and (ii) the final texture developed in the finished products will substantially affect their in-service performance as the properties such as yield strength, creep strength, fatigue and stress corrosion cracking are strongly orientation dependent (Philippe et al. 1995). Therefore, knowledge of the texture and the anisotropy in mechanical properties of the sheet are required for predicting the in-service behaviour of the fabricated components.

Zircaloy-4 material generally has equiaxed grains after pilgering and subsequent annealing processes (C. Liu et al. 2018). Once the pilgering process is completed the Zircaloy exhibits high intensity texture in such a way that it is not possible to remove the texture entirely by any amount of recrystallization with annealing. Therefore, because of the annealing texture, the anisotropy response is present in mechanical properties of the alloy. Therefore, it is important to study the anisotropy of mechanical properties and their dependence on texture history of the material.

### 2.1 Texture in Zirconium alloys

Naturally, most of the solid materials are crystalline in nature and most of them are poly crystal materials. The Zircaloy-4 material that is used in the present study is poly crystalline material. The microstructure of Zircaloy-4 or for that matter any materials microstructure represents grains, grain boundaries, secondary phases or inclusions, dislocation substructures. But the microstructure is not in complete form without the information about texture of the material. In materials science scientific community the texture means the crystallographic orientation of the grains. Since properties of materials depend on

crystallographic plane of a single crystal, textured material, which contain number of such single crystal in different orientations of groups, has important bearing on material properties. Therefore, it is important to study the texture of material and its effects on properties of the materials.

The Zircaloy-4 is used for developing so many components which are used in nuclear reactor core such as fuel cladding tubes, bottom nozzle, top nozzle, spacer grid, mixing channel and etc., and all these components are manufactured by different mechanical deformation and thermal treatments. The texture depends on the history of the material's thermomechanical deformations and heat treatment steps. Therefore, it is important to study the texture of the Zircaloy – 4 materials.

Generally, in Zirconium alloy materials basal texture will be evolved. The basal poles  $\langle 0002 \rangle$  are tilted towards (transverse direction) TD with an angle range of  $\pm 20-40^\circ$  and these are away from normal direction (Murty and Charit 2006b). Further, the  $\langle 10\bar{1}0 \rangle$  prismatic poles aligned parallelly with rolling direction by cold rolling of the material. Once the annealing is done on the material, the crystals rotate  $30^\circ$  about their c axis therefore the  $\langle 11\bar{2}0 \rangle$  poles are aligned parallel to the rolling direction. Because of this the weaker hoop stress of cladding tubes becomes stronger. The Zircaloy-4 alloy also develops strong basal structure and it does not change much with annealing (Murty and Charit 2006b). The pilgering of Zircaloy-4 cladding tubes involve reduction of thickness and diameter. Therefore, the texture evolved after the pilgering of tubes depends on thickness to diameter ratio.

A strong texture of Zircaloy-4 has both effects beneficial and detrimental too (Haggag and Murty 1997). It is because generally, in Zircaloy-4, hydrides are aligned perpendicular to the c-axis of hcp unit cells. The detrimental effect is noticed when the c-axis of hcp unit cell is aligned in circumference direction (or hoop direction). Because, when hoop stress is a

developed in the cladding cylinder the interface between hydride and matrix will open up. In first case, that is, the beneficial effect of texture, is derived when c-axis of hcp unit cell align parallel or near parallel to the radial direction of pillgered tube. It is due to resistance of the hydride alignment with the development of hoop stress.

## **2.2 Constitutive equation for flow stress**

Over the years, the Zircaloy-4 is widely used structural material in nuclear industries due to its corrosion resistance at high temperatures (A. Shibata et al. 2016), good creep strength (Cappelaere et al. 2012), low thermal neutron absorption cross section and moderate mechanical properties. This material is particularly used as cladding tube and spacer grids due to their texture dependent tensile flow behaviour. For such an important material, it is crucial to calibrate constitutive equations for flow stress which are used in finite element code for simulation of material deformation during processes.

The constitutive equations for flow stress are mainly two types: physical based and phenomenological (Y. C. Lin and Chen 2011). While physical based constitutive equations for flow are developed by the observation of physical phenomenon of deformation of the materials, the phenomenological constitutive equations for flow stress are implemented by empirical observations made from statistical mathematical tools. Generally, the physical based equations are more accurate in prediction of flow stress behaviour than that of the phenomenological equations. But the physical based equations involve a greater number of constants compared to that of the simple phenomenological constitutive equations for flow stress. Johnson-Cook (JC)(Fu et al. 2016), Modified Arrhenius (m-Arr)(Chen et al. 2019; Lei et al. 2019), Khan-Huang (KH), Khan-Huang-Liang(KHL), Khan-Liang-Farrokh (KLF), Fields-Backofen (FB), and Molinari-Ravichandran (MR) are some of the phenomenological constitutive equations for flow stress. Examples of physical based constitutive equations for flow stress are Zerilli-Armstrong (ZA), modified Zerilli-Armstrong (m-ZA) Rusinek-Klepaczko (RK), Voyiadjis-

almasri (VA), Bodner-Partom (BP) and Cellular Automation (CA), Kocks–Mecking–Estrin (KME)(Seong et al. 2020).

Many works have been reported the two types of constitutive models calibrated for different materials. Modified Johnson Cook model (m-ZC), m-ZA, m-Arr and KHL models have been calibrated for Inconel 625 super alloy for analyzing the effect of strain rate and temperature on flow stress and it has been concluded that the m-Arr is more suitable (Badrish et al. 2020). Arrhenius-type equation has been used for predicting the flow stress behaviour of Aluminum alloy 7A04 when it is subjected to isothermal compression test at elevated temperatures, and it has been resulted in good agreement with experimental data (Qiang et al. 2020). Prediction of flow stress for uniaxial isothermal and dynamic compression tests at range of 673K to 1373K has been done with m-ZA, Cowper Symonds (CS), m-JC, Arr, KHL and The m-JC has been noted as suitable model(Saxena et al. 2019). Different types of Arrhenius-type constitutive models have been used for predicting tensile behaviour of 17-PH stainless steel sheet and accurate prediction has been resulted through multi-strain modified models (Su et al. 2020). In a comparison study on prediction accuracy of m-ZA and m-JC for isothermal deformation of Aluminum 5083 + SiC composite, the m-ZA has been identified as better suitable model (Rudra, Das, and Dasgupta 2019). JC, m-JC, FB, KHL and Mechanical Threshold Stress (MTS) constitutive equations for flow stress have been calibrated for Ti-6Al-4V alloy at low strain rates and elevated temperatures. Their prediction capabilities also have been compared with statistical parameters in ref. (Kotkunde et al. 2014; Tao et al. 2018). Flow stress behaviour of friction welding of GH4169 superalloy has been predicted by m-FB, JC and Arr models. The experimental stress data has been in good agreement with the predicted stress through Arr(Geng et al. 2018). Experimental compressive stress of Al-Zn-Mg-Cu Aluminium alloy at elevated temperatures has been compared with the predicted stress through Arrhenius type equation, and it has been resulted with high coefficient of correlation (R) of 0.993(Zhang

et al. 2018). The hyperbolic-sine Arrhenius equation has been used for predicting hot compression stress of two different Titanium alloys and the prediction capacity of the model also has been improved by reduced gradient refinement method (Bodunrin 2020). Similarly, JC, m-ZA, m-Arr also calibrated for the austenitic stainless steel 316 at the temperature range of 323-623K and strain rate range are 0.05-0.3(Gupta, Anirudh, and Singh 2013). Furthermore, hot deformation behaviour of 7055 Aluminum alloy is analyzed by phenomenological models: JC, modified Fields-Backofen (m-FB), Arrhenius (Arr). It was concluded that Arr predicts well due to taking consideration of strain rate – temperature combined effect (Wang et al. 2018). In addition, JC model and ZA models have been integrated for better prediction of flow stress for Ti-6Al-4V alloy at high strain rate and elevated temperatures (Che et al. 2018). FB, Fields-Backofen-Zhang (FBZ) and modified Field-Backofen-Zhang (m-FBZ) have been used for predicting the isothermal tensile flow stress of alpha-Ti tubes. Among the three, m-FBZ model prediction is very accurate with R value of 0.9873(Y. Lin et al. 2018). JC, m-JC models have been employed to predict flow stress of Al7075 at elevated temperatures and due to the modification of temperature term in JC, the m-JC has given accurate prediction (Rasaei, Mirzaei, and Almasi 2020).

Relating to Zircaloy-4, modified Johnson Cook model has been calibrated. This model has been used for simulation of pilgering process. The results have showed that predicted flow stress is greater than the experimental flow stress (Deng et al. 2019). A macro constitutive model was calibrated for reactivity initiated accident (RIA) loading conditions by Sauxet et al(Le Saux et al. 2008; Le Saux, Besson, and Carassou 2015). Material anisotropy of Zircaloy-4 was analyzed by Hill 48 yield criteria with a combination of isotropic hardening model (Rickhey et al. 2015). None of the work, especially for the Zircaloy-4, explained the suitable model for stress prediction.

In the present work, phenomenological constitutive equations such as JC, m-Arr and physical based equation, m-ZA, are calibrated for three different types of Zircaloy-4 materials. The isothermal uniaxial tensile test data was used to determine the constant of the models and subsequently the predictability of these models for the three Zircaloy-4 materials are compared using statistical parameters such as coefficient of correlation (R) and average absolute error ( $\Delta$ ).

### **2.3 Forming limit diagrams (FLD) and finite element analysis (FEA)**

The Zirconium alloys are worldwide well-known structural materials in power plants. The balanced strength and ductility, resistance to high temperature corrosion and also low neutron absorption cross section(Nakamura et al. 2007) are main properties of Zirconium alloys and therefore they are mainly used at the core of nuclear industries. The above properties are due to their alloying elements: Tin, Iron, Niobium, Nickel, Chromium and other elements. The alloys contain Zirconium and other alloying elements more than 95% and less than 2% respectively. The development of Zirconium alloys was started in 1950's and along with the improvements in properties of the alloys; they are named as Zircaloy-1, Zircaloy-2, Zircaloy-3 and Zircaloy-4. The Zircaloy-1 and Zircaloy-3, due to their deleterious effects in corrosion resistance, have become obsolete. Presently, Zircaloy-2, Zircaloy-4, and other new alloys are in use.

In Pressurized Water Reactors (PWR) Zircaloy-4 is used as fuel cladding tube, in light water reactor (LWR), it is employed as spacer grid, and in boiling water reactors (BWR) it is used in the form of channel box. During the manufacturing of the fuel cladding tubes, a cylindrical slab of Zircaloy-4 is converted in to a thin tube. The spacer grid in LWR consists of an array of grid cells. In each cell, sheet metal is bent three times perpendicularly to form rectangular shape. Further, each strip between the bents is subjected to series of projections to enclose the cladding tubes in correct location with friction grip. The spacer grids, by supporting

the structural integrity of the cladding tubes, increases the life time of the plant and therefore it is the main component in LWR(K. N. Song, Lee, Shin, et al. 2010). In the same way, the sheet material in channel box application is subjected to severe deformation. Therefore, it is important to note that the study of deformation behaviour of the material is main concern to improve the performance of the Zircaloy-4.

The cladding tubes are generally manufactured by pilgering method. In this method initially a thick circular slab is center drilled along the length of the slab. Then a mandrel is inserted through the hole. Along with the mandrel, the slab is passed through a gap between two pilgering dies or rollers. Simultaneously two motions are given to the rollers, rotation and translation motion along the slab length. The slab is also rotated about the axis of the hole and is pushed along the direction of length towards the rollers. As a result, simultaneously, the thickness and diameter of the tube decreases and length increases. The process is characterized by Q-factor. The Q-factor is defined as the ratio between a strain resulting from thickness reduction and strain resulting from reduction of diameter. The effect of Q-factor on final product has been found that the increase of Q-factor will increase the durability of final product(Hideaki Abe and Furugen 2012). Recently, Vertikaler Massenausgleich Ringwalzei (VMR) technology is used to increase the deformation ratio and decreasing inhomogeneity of the strain distribution, thereby increasing the productivity by reducing the number of pilgering steps(Vakhitova et al. 2017).

In order to determine forming limit of sheet metal in a stamping process the FLD's came into picture in 1960's. Thereafter, there has been a lot of research underwent from experimental construction to theoretical calibration of FLDs (Kotkunde et al. 2017). Recently, Yunmi Seo et.al, (Seo et al. 2011) constructed forming limit diagram for Zircaloy-4 in 2011. In their work they have pointed out two main observations. Firstly, effect of lubrication on specimen. The samples, that were lubrication applied, showed crack at the peak of the dome

whereas others did not. Secondly, the minor strain in the FLD was decreased with the decrease of specimen width. Further, the FLD of Zircaloy-4 was compared with both FLD of Zirlo (other Zirconium alloy) and analytical FLD constructed from M-K Model. Thereafter, again in 2017, P. M. Karuppasamy et. al., constructed the FLD of Zircaloy - 4 to find out the effect of surface pit on the sample and its influence on the fuel spacer grid. The pits at the distance of 1/20 of sample length from the center of the sample were more prone to bring high risk of fracture than the pits at other locations of the sample.

The FLDs are generally constructed by using limiting dome height (LDH) test or Nakajima stretching test. The experimental stretching operations involve trial and error methods in optimizing the process parameters. The optimization process is very expensive, time consuming and laborious. Thanks to finite element (FE) simulations. The FE simulations minimize the tool design cost, time and there is no question of physical labor requirements. Therefore, the simulations are very useful even to compare different forming methods(Desu, Singh, and Gupta 2016), to predict thickness strains(Singh and Kumar 2005), to optimize design parameters(Singh, Dixit, and Kumar 2008) and to analyze limiting strains at warm conditions(Kotkunde, Gupta, and Singh 2015). The FE simulations, in the back ground of programmed code, require analytical models for accurate prediction of results. There has been decades of research undergone in developing the models starting from Hill-Swift necking criteria in 1952. In 1975, the famous Marciniak-Kuczynski (M-K) model was developed with an assumption of an initial inhomogeneity factor in the sheet metal. Thereafter, the bifurcation theories (Storen - Rice in 1975) were developed. Recently (in 2013 by Hora et al.), the modified maximum force criterion (MMFC) has been developed. All these above mentioned models incorporate a variety of constitutive models(K. Sajun Prasad et al. 2016). The constitutive models development also started in past, in 1948 by the Hill. Since then, the development has been increased and some of them are Barlat-Lian in 1989, Barlat-1991, Karafillis-Boyce-1993,



Barlat-2003, Born-Besson- 2004, Barlat-2005, Banabic-2005, and again Aretz-Barlat-2013(Lian et al. 2017). Therefore, assortment of the models in the simulation process of the sheet materials is a vital step.

In scientific community, even though the FLD concept has been started in early 1960's, there is a little focus on the formability of Zircaloy-4(Marimuthu et al. 2018; Seo et al. 2011). In the present work, the formability limits of the Zircaloy-4 at room temperature are analyzed in terms of FLDs in three different sample orientations: rolling, 45° to rolling (radial) and 90° to rolling (transverse). Limiting dome height is measured and strain distribution profiles are also plotted. Further, FE-Simulation is performed using LS-Dyna, and validated with the experimental data.

The Experimental construction of forming limit diagrams is a very big procedure and it takes lot of time. Now a days, there is a lot of demand in reducing product life cycle time, so there is not enough time to construct the experimental forming limit diagrams. Therefore, in the competitive scenario, the automotive industries demand is to quickly construct FLCs from theoretical and empirical formulas. Another problem with the experimental FLD is that large scattering of the data points. Despite of all the drawbacks of the FLD tool, it is widely used tool in industries due to its simplicity and excellent performance. Therefore, for quick understanding of the formability of material it is necessary to develop theoretical forming limit diagrams.

Now a days, theoretical models for achieving forming limit curve (FLC) in back grounds of FE code. Swift diffuse criterion and Hill local necking criterion are most commonly used criteria for developing theoretical forming limit diagrams(Hill 1952; Swift 1952). The 'maximum loading force' and 'maximum principal stress' are taken as initial assumptions in the Swift and the Hill criteria respectively to derive them. Storen and Rice (Stören and Rice

1975) considered that FLC can be derived from a vertex considered on yield surface. This vertex is obtained by force equilibrium between necked and non-necked regions of material. Another well-known model is Marciniak and Kuczynski (Zdzislaw Marciniak and Kuczyński 1967) and it is generally known as M-K model. In this model, initial geometry imperfection is assumed. The FLC obtained from M-K model depends on the size and shape of the imperfection therefore M-K model does not produce exact FLC rather it gives a band between safe and fracture (Ghazanfari and Assempour 2012). Bressan-Williams (Bressan and Williams 1983) is another alternative to the above mentioned criteria. In Bressan-Williams (BW) model localized necking is estimated by using the famous shear failure theory where maximum shear stress is calculated. In a proportional loading condition, the stress based FLCs and strain based FLCs are equally viewed to explanation and therefore, the strain based FLCs can be derived from stress based FLCs. In the present work, Hill-Swift criterion (HS), Storen-Rice bifurcation criterion (SR), Bressan and Williams (BW) model, Hill-Tresca (HT) model are calibrated for Zircaloy-4 material.

## **2.4 Research gaps**

Based on the above literature review the following research gaps are identified:

- The variation of tensile properties with respect to the sample orientation or the anisotropic behaviour of tensile properties at room temperature and elevated temperatures of Zircaloy-4 have to be studied.
- Effects of processing routes of the Zircaloy-4 sheets on tensile properties need more attention.
- The correlation of anisotropic behaviour of Zircaloy-4 with texture has to be studied.
- Suitable constitutive model to well predict the stress-strain data at room and elevated temperatures is not identified for Zircaloy-4.
- Experimental forming limit diagrams in different orientation of the Zircaloy-4 sheet material have to be explored.

- Effect of processing routes of the Zircaloy-4 sheet materials on formability limits is to be given more attention.

## **2.5 Scope of objectives**

Using the above-mentioned research gaps, the five objectives are set. In the following sections, these objectives and their scopes are discussed.

1. Study of mechanical properties and deformation behaviour of Zircaloy-4 sheets produced by rolling and pilgering process.
2. Studies related to the effect of texture and microstructure on formability of Zircaloy-4 sheets.
3. Calibration of constitutive models for Zircaloy-4.
4. Experimental studies of forming limit diagrams (FLDs) using limiting dome height (LDH) test of Zircaloy-4
5. Calibration of theoretical FLD for Zircaloy-4.

**Objective 1:** Study of mechanical properties and deformation behaviour of Zircaloy-4 sheets produced by rolling and pilgering process.

In this objective, mechanical properties such as ultimate tensile strength, yield strength, percentage elongation, planar anisotropy, anisotropy index, strength coefficient, strain hardening exponent and their variation with respect to strain rate will be observed. Some of these values will be used as input to the finite element simulations, theoretical forming limit diagrams and calibration of constitutive models will be done. The tensile flow behaviour in terms of engineering stress vs engineering strain, true stress vs true strain, true stress vs true plastic strain and differential curves will be discussed.

**Objective 2:** Studies related to the effect of texture and microstructure on formability of Zircaloy-4 sheets.

In the present study, there are three types of Zircaloy-4 sheets used. The presence of intensity of the texture in all the three types of the sample will be examined. Using EBSD technique, microstructure indicating texture presence and main texture component will also be determined. The results obtained from the texture and microstructure analysis will be correlated with tensile properties such as yield strength and elongation dependent anisotropy values.

**Objective 3:** Calibration of constitutive models for flow stress in Zircaloy-4.

In the present study, constitutive models such as Johnson-Cook (JC), modified Zerilli Armstrong (m-ZA), modified Arrhenius (m-Arr), and Khan-Hang-Liang (KHL) will be Calibrated for predicting the flow stress. A comparative study will be carried out using statistical parameters. Out of the four constitutive equations the best suitable one for better prediction of flow stress will be found out.

**Objective 4:** Experimental studies of forming limit diagrams (FLDs) using LDH test of Zircaloy-4.

The formability limits can be visualized pictorially by constructing the forming limit diagrams. By using the forming limit diagrams, the complete deformation ranges from tension-tension region to tension-compression region will be analyzed for SRS and TRS materials. The forming limit curves of the Zircalloy-4 alloy will be studied with respect to sample orientation to bring correlation between anisotropy in forming limits and texture history of the materials.

**Objective 5:** Calibration of theoretical FLD.

Theoretical FLDs using Hill-Swift criterion, Storen-Rice criterion, Bressan – Williams shear instability criterion, and Hill-Tresca criterion is calibrated. These theoretical

FLDs will be compared with experimental FLDs. Out of all the theoretical FLDs, the criteria which predicts well will be analyzed.

## 2.6 Methodology

To achieve all the objectives that are mentioned above a brief methodology is given below.

**Objective 1: Study of mechanical properties and deformation behaviour of Zircaloy-4 sheets produced by rolling and pilgering process.**

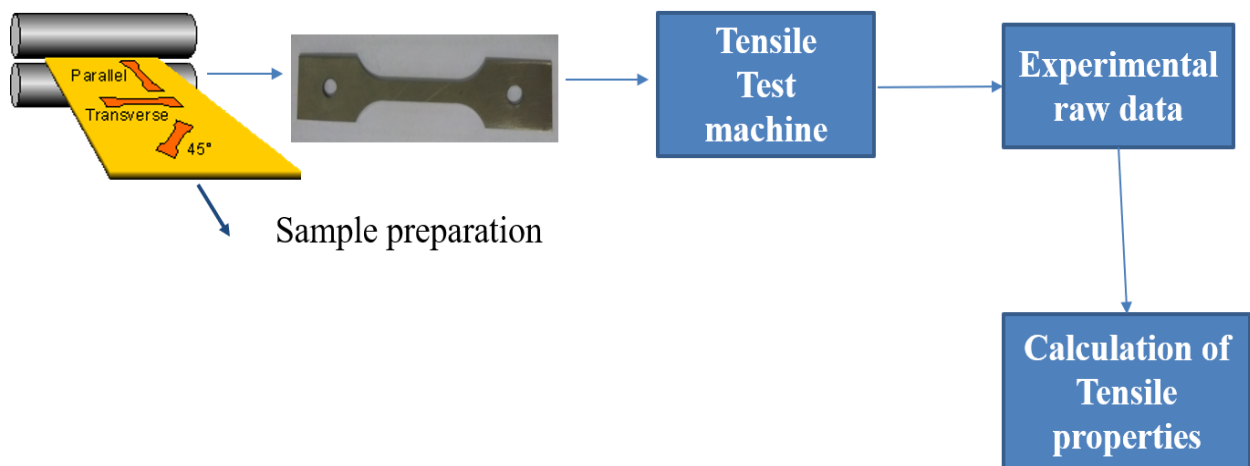


*Fig. 2.1: Flow diagram representing tensile tests*

As shown in the Fig. 2.1, the tensile test samples in three different sample directions will be cut. Then, by using ELecra-50 Biss hot forming machine with 50-ton capacity will be used to do the experiments. From the raw data obtained from the tensile tests, the material properties such as ultimate tensile strength, yield strength, strength coefficient, strain hardening, anisotropy index and planar anisotropy at room temperature will be evaluated. Further, their variation with respect to strain rate and sample direction will also be studied.

**Objective 2: Studies related to the effect of texture and microstructure on formability of Zircaloy-4 sheets.**

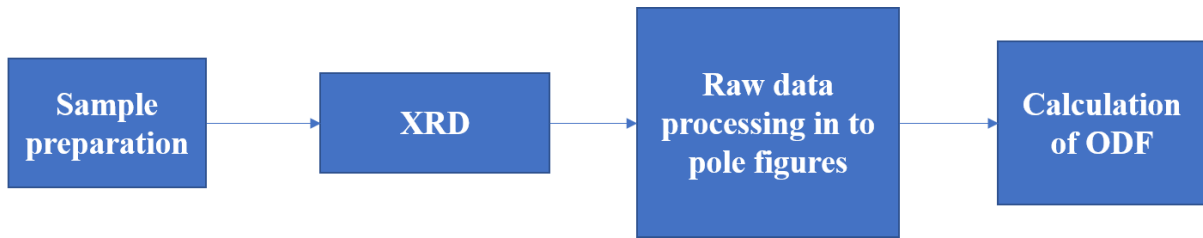


*Fig. 2.2: Flow diagram representing calculation of ODF by XRD tests*

From Fig 2.2, X-ray diffraction (XRD) studies on the as-received sheets will be performed using an inel equinox diffractometer with Cu K $\alpha$  radiation equipped with the position-sensitive detector. The texture will be measured on sheet specimens of 25 $\times$ 15 mm<sup>2</sup> size. Initially, pole figures are determined and then from the pole figure data the orientation distribution functions are to be calculated. Furthermore, the fibre texture of the three materials will be compared.

**Objective 3: Calibration of constitutive models for Zircaloy-4.**

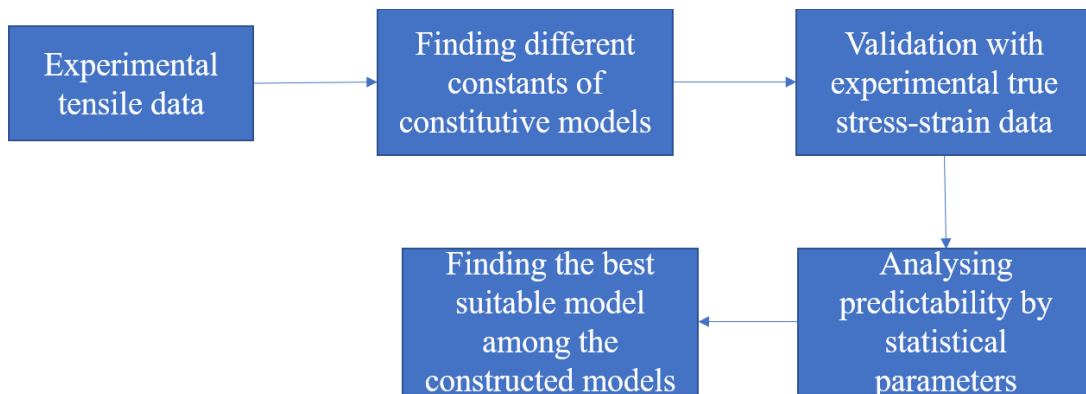


*Fig. 2.3: Calibration of constitutive models for Zircaloy-4 material*

As shown in the Fig 2.3, stress-strain data obtained from tensile tests will be used for constructing the constitutive models. Initially, a selected range of stress-strain data will be taken to find out different material constants of the model. Then by substituting the constants, the model will be calibrated and predicted data is generated. The predicted data will be validated with the experimental data. The predicting capacity of the model is analyzed by

calculating the statistical parameters. Thereafter, a comparison study will be done to select the suitable model for the best prediction of the flow stress.

**Objective 4: Experimental studies of FLDs using LDH test.**

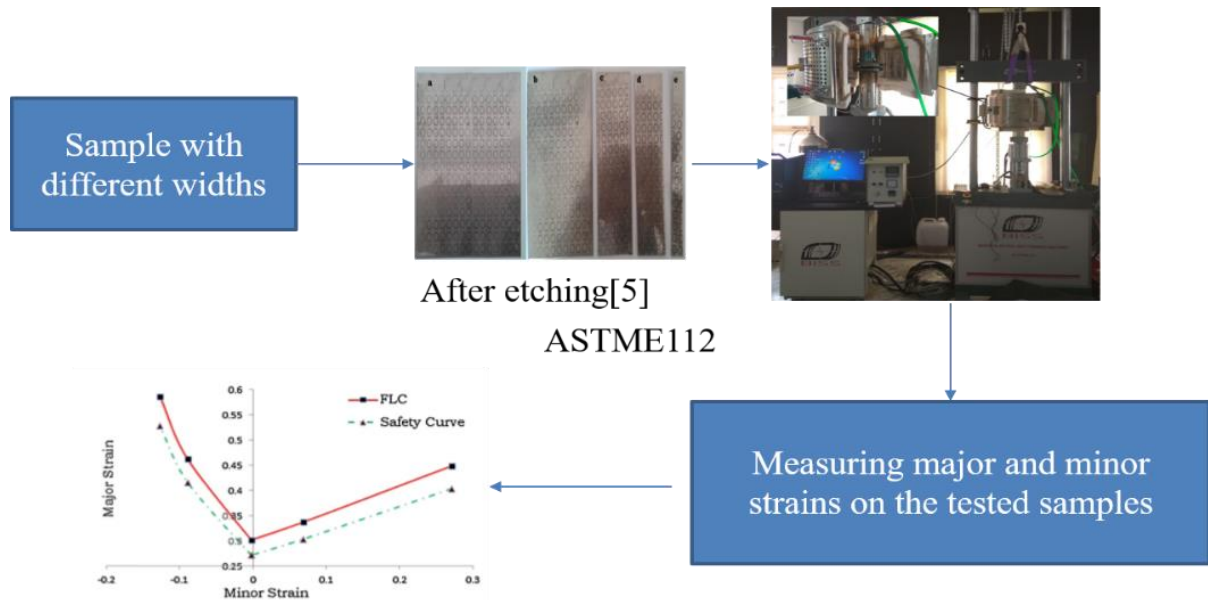


*Fig. 2.4: Flow diagram representing experimental construction of forming limit diagram*

Fig. 2.4 shows the flow diagram of the construction of the experimental forming limit diagram. Initially, the Zircalloy sheets are cut into varying widths. Then the samples are chemically etched to form circles on the surface of the samples. These are subjected to stretching operation. After the crack initiation on the samples, the major and minor strains are measured by a travelling microscope. Major strain as y-axis and minor strains as x-axis separating the safe and fracture zone forming limit curve is drawn. The complete diagram is called forming limit diagram.

**Objective 5:** Calibration of theoretical forming limit diagrams.

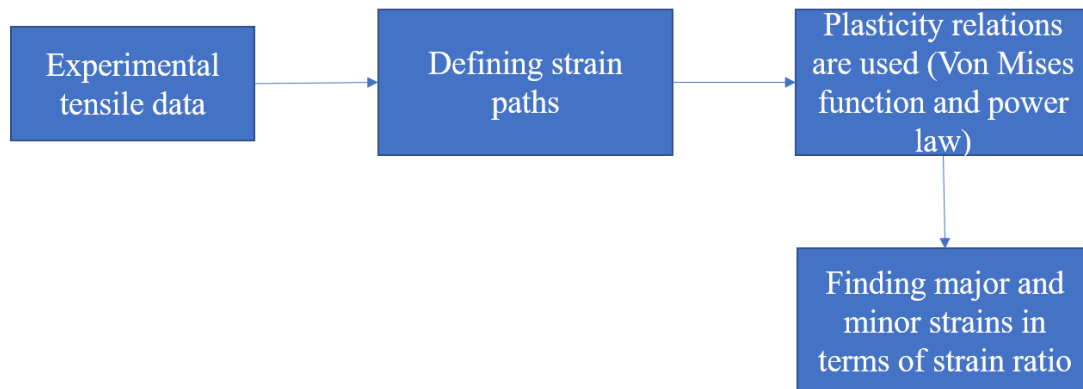


*Fig. 2.5: Flow diagram representing construction of theoretical forming limit diagrams*

Experimental tensile data will be used for developing theoretical forming limit diagrams (Fig. 2.5). Strain paths will be defined in the range between tension-compression region to tension-tension region. Plasticity relations of the Von-Mises function and power-law would be used to establish the relation between the major and minor strains and strain ratios. Once the relationship is established, the minor and major strains are determined. By plotting at least four theoretical FLDs, they will be compared with experimental data. Further, the best suitable criterion will be determined for the material. The comprehensive methodology in achieving all the above mentioned five objectives and their correlations are represented in the Fig. 2.6.

In summary, a detailed literature review is conducted. The details are ranged from choice of Zirconium in nuclear industries to its recent alloy Zircaloy-4 development, properties and applications. Furthermore, recent studies related to constitutive models and forming limit diagrams and its FE analysis are also reviewed. Finally, the research gaps are identified, then the objectives are framed with their scope and suitable methodology is designed. The first step in the methodology is to find the properties of the given Zircaloy-4 sheet materials. These are



elaborately explained in the upcoming chapters. The detailed description of room temperature tensile properties of Zircaloy-4 is given in next Chapter 3.

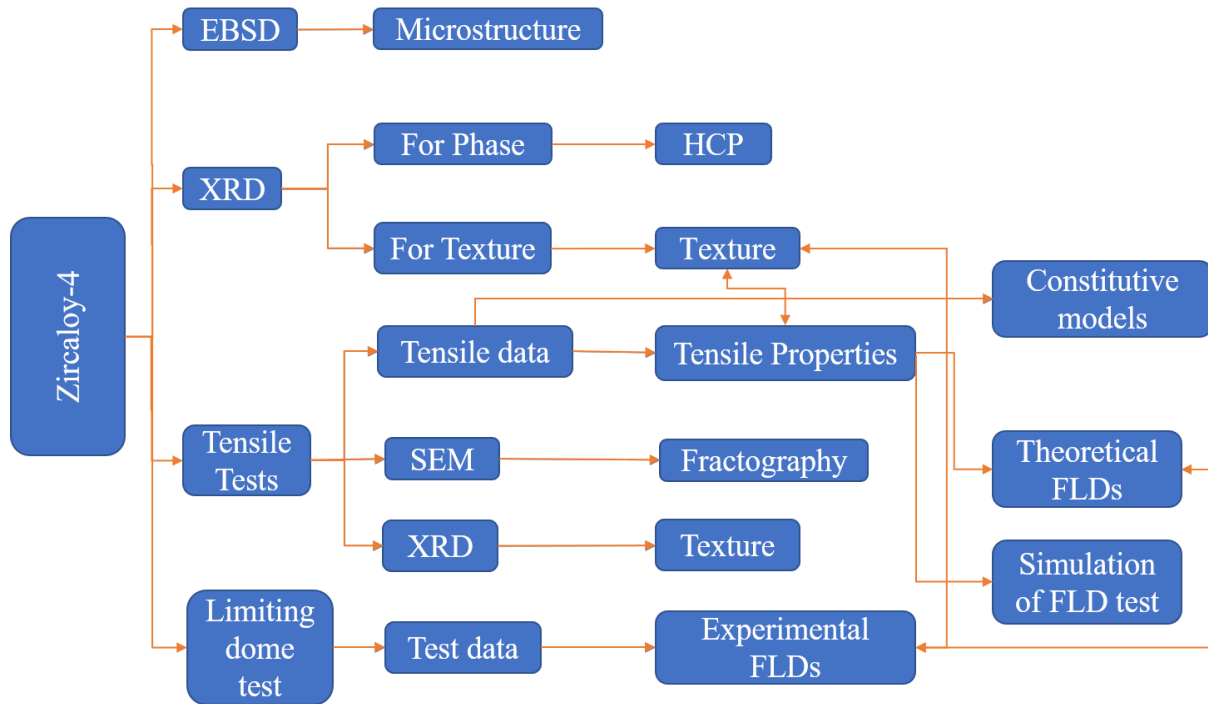


Fig. 2.6: Comprehensive methodology

## **Chapter 3**

# **Orientation dependent tensile flow behaviour of Zircaloy-4 at room temperature**

### **3.1 Introduction**

Tensile properties of Zircaloy-4 materials are important to study because the accurate values of tensile properties are used as input data for calibrating constitutive models. Since the Zircaloy-4 material is hexagonal close packed structured material, limited slip systems are activated during deformation. Therefore, the material properties depend on the direction of applied load or in other words texture influences the tensile properties of the material. In this chapter, tensile properties of the three Zircaloy-4 materials at room temperature are presented. The influence of load direction and strain rate on the tensile properties is explained. Furthermore, the correlation between the tensile properties and texture also expressed.

### **3.2 Experimental details**

#### **3.2.1 Materials used and its composition**

The Zircaloy-4 sheet materials were supplied by Nuclear Fuel Complex (NFC), Hyderabad, India. The sheets of 0.8 mm thickness were produced by three routes namely slab route sheet (SRS), tube route sheet (TRS) and low oxygen sheet (LOS). The SRS and TRS sheet materials were produced by normal rolling and pilgering processes. The LOS was a normal rolled sheet with relatively low Oxygen content in comparison to those of SRS and TRS. The chemical compositions of the three different sheet materials provided by NFC are presented in Table 3.1.

*Table 3.1: Chemical composition of Zircaloy-4*

Material	Composition (wt.%)				
	Sn	Fe	Cr	Balance	O (ppm)
Slab Route Sheet (SRS)	1.33	0.22	0.11	Zr	1280
Tube Route Sheet (TRS)	1.34	0.21	0.12	Zr	1292
Low Oxygen Sheet (LOS)	1.33	0.22	0.11	Zr	834

### 3.2.2 Experimental procedure of microstructure and texture

Microstructural characterization of as-received material was carried out using EBSD (Electron Back Scatter Diffraction). The specimen preparation for EBSD was carried out using standard metallographic technique followed by electropolishing in a perchloric acid solution (20% Perchloric acid + 80% Methanol). A voltage of 21 Volts has been used during electropolishing of the samples. EBSD measurements are performed using an HKL system (Nordlys) mounted on a Carl Zeis Dual Beam FEG microscope (Auriga). X-ray diffraction (XRD) studies on the as-received sheets are performed using an inel equinox diffractometer with Cu K $\alpha$  radiation equipped with a position-sensitive detector. The texture was measured on sheet specimens of 25×15 mm<sup>2</sup> size. An inel G3000 texture goniometer coupled with a curved position sensitive detector has employed for texture measurement based on Schulz reflection technique. Five incomplete pole figures {10 $\bar{1}$ 0}, {0002}, {10 $\bar{1}$ 1}, {10 $\bar{1}$ 2} and {10 $\bar{1}$ 3} were measured from 1/2 thickness level of the normal direction (ND) plane. An oscillation stage was employed with 20 mm specimen translation to increase the measured area. From the pole figure data, the complete orientation distribution function (ODF) plots are obtained. The results are presented in terms of {0002} pole figures and ODF plots of constant  $\varphi_2$  sections ( $0^0$  and  $30^0$ ) with iso-intensity contours in the Euler space defined by three Euler angles ( $\varphi_1$ ,  $\Phi$ ,  $\varphi_2$ ).

### 3.2.3 Experimental procedure for tensile tests of SRS, TRS and LOS at room temperature

The tensile properties of the as-received sheet materials were evaluated in three sample directions, namely the longitudinal (L or 0°), R or 45° (specimen axis at 45° to the rolling direction) and transverse (T or 90°) directions. The longitudinal and transverse directions correspond to rolling direction (RD) and the direction perpendicular to the rolling direction, respectively. The sub size tensile specimens of ASTM standard E8/E8M-11 considered for testing. The samples were cut from raw sheet material by wire-cut electro-discharge machine for high accuracy. The dimensions of the tensile sample is shown in Fig. 3.1. The tensile tests conducted as per ASTM E8 standard on Electra-50 BISS servo-electric universal testing machine of 50 kN capacity at three different strain rates ( $0.001s^{-1}$ ,  $0.005s^{-1}$  and  $0.01s^{-1}$ ) at room temperature for three different sample orientations. The different test parameters have been shown in Table 3.2. The universal testing machine is computerized and has a split furnace facility, as shown in Fig. 3.2. After conducting the tensile tests, the load vs displacement data was taken as the raw data and then converted into true stress and true strain data. The true stress and true strain data is then converted to true stress vs true plastic strain by excluding the elastic component of the data. The experiments are carried out with constant strain rates by varying the cross-head velocity exponentially with the help of a feedback control system. The cross-head velocity is as given in the Eq. 3.1.

$$v = \dot{\epsilon}L \exp(\dot{\epsilon}t) \quad (3.1)$$

where  $v$ ,  $L$  and  $t$  are crosshead velocity, gauge length of specimen and time respectively.

Three specimens are tested from each set of test parameters and average values of yield strength ( $\sigma_Y$ ), ultimate tensile strength ( $\sigma_{UTS}$ ), %elongation are calculated. Further, tensile

fracture surfaces are examined under the scanning electron microscope (Carl Zeiss Sigma FE: SEM).

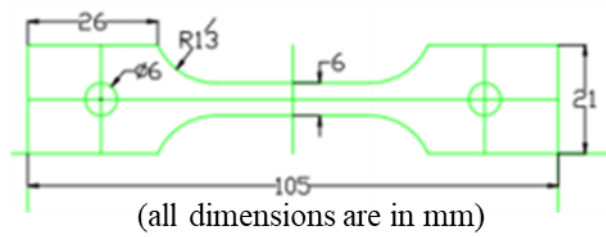


Fig. 3.1: Schematic diagram of the tensile sample used in the present study

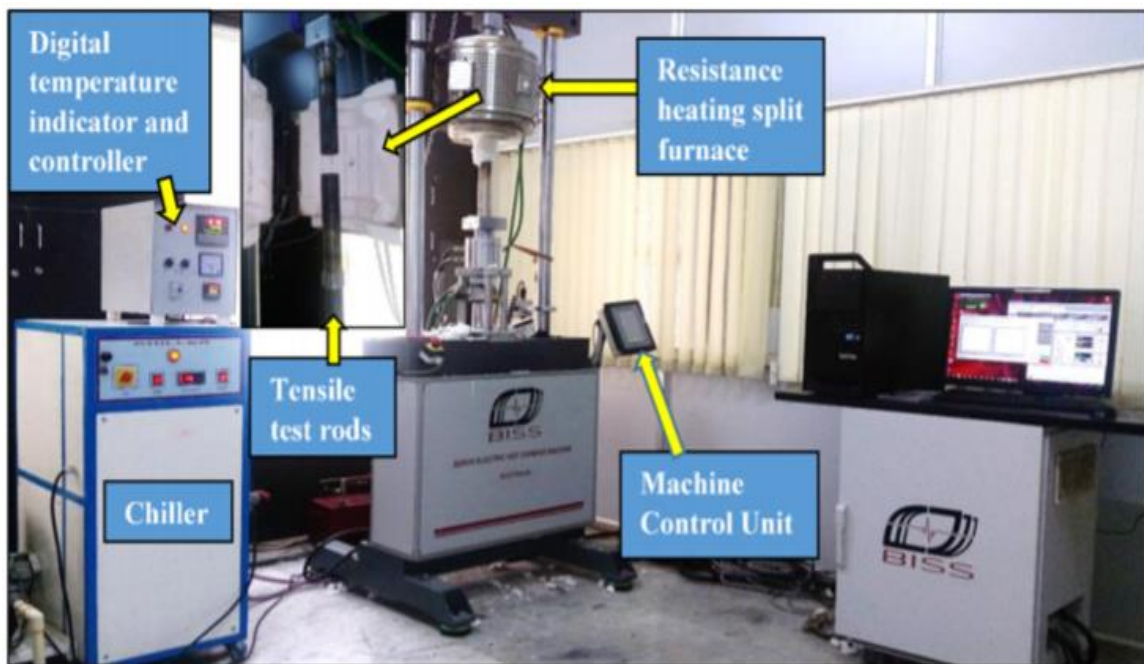


Fig. 3.2: Electra-50 BISS servo-electric universal testing machine of 50 kN capacity

Table 3.2: Tensile test parameters.

Zircaloy - 4	Strain rates ( $s^{-1}$ )	Orientations	Temperature
Slab Route Sheet (SRS), Tube Route Sheet (TRS), Low Oxygen Sheet (LOS)	0.001, 0.005, 0.01	Longitudinal (L or $0^\circ$ ), Radial (R or $45^\circ$ ), Transverse (T or $90^\circ$ )	Room Temp.

### 3.3 Results and Discussion

#### 3.3.1 Microstructure and texture study

The microstructures of the present alloys are displayed in Fig. 3.3. It can be seen that all the samples exhibited equiaxed grain structures typical of a well-recrystallized microstructure. It is also clear that the majority of the grains have their basal poles parallel to N=sheet plane normal (the red grains). The XRD patterns of all the three alloys reveal the presence of only close-packed hexagonal Zr phase (Fig. 3.4). The textures present in the three materials are shown in Fig. 3.5(a). The intensity and location of poles in {0002} pole figures are different. The sample TRS display maximum intensity. The basal pole figures do not display perfect c-type texture, i.e. pole in basal pole figure located at  $(0^\circ, 0^\circ)$ . The location of poles in basal pole figures are  $(9.3^\circ, 358.8^\circ)$ ,  $(9.2^\circ, 68.4^\circ)$  and  $(10.1^\circ, 112.0^\circ)$  in SRS, TRS and LOS samples respectively. The locations of the main texture components in ODF are  $(\varphi_1=90.0^\circ, \Phi = 9.7^\circ, \varphi_2 = 55.0^\circ [f(g) = 4.7])$ ,  $(\varphi_1= 155.4^\circ, \Phi= 10.6^\circ, \varphi_2 = 15.0^\circ [f(g) = 6.5])$  and  $(\varphi_1= 200.0^\circ, \Phi = 25.0^\circ, \varphi_2 = 15.0^\circ [f(g) = 4.8])$  in SRS, TRS and LOS samples respectively. The intensities  $f(g)$  of the texture components reported as “times random” and the corresponding [0001] || ND fibre plots of all the three materials are displayed in Fig.3.5(b). Interestingly, the [0001]||ND fibre exhibits maximum intensity for TRS sample. The [0001] || ND fibre of the LOS sample is nearly homogeneous, and the extent of inhomogeneity is more for TRS.

From Fig. 3.5 (b), the overall intensity of texture in both the ODF and [0001] ||ND fibre is very high in TRS sample in comparison to those of SRS and LOS. This can be due to a large amount of deformation associated with TRS sample produced by pilgering process. It is essential to mention here that the processes involved in both SRS and LOS samples are the same except for the presence of Oxygen content. As a result, the overall intensities of both the samples in ODF do not display a significant difference.

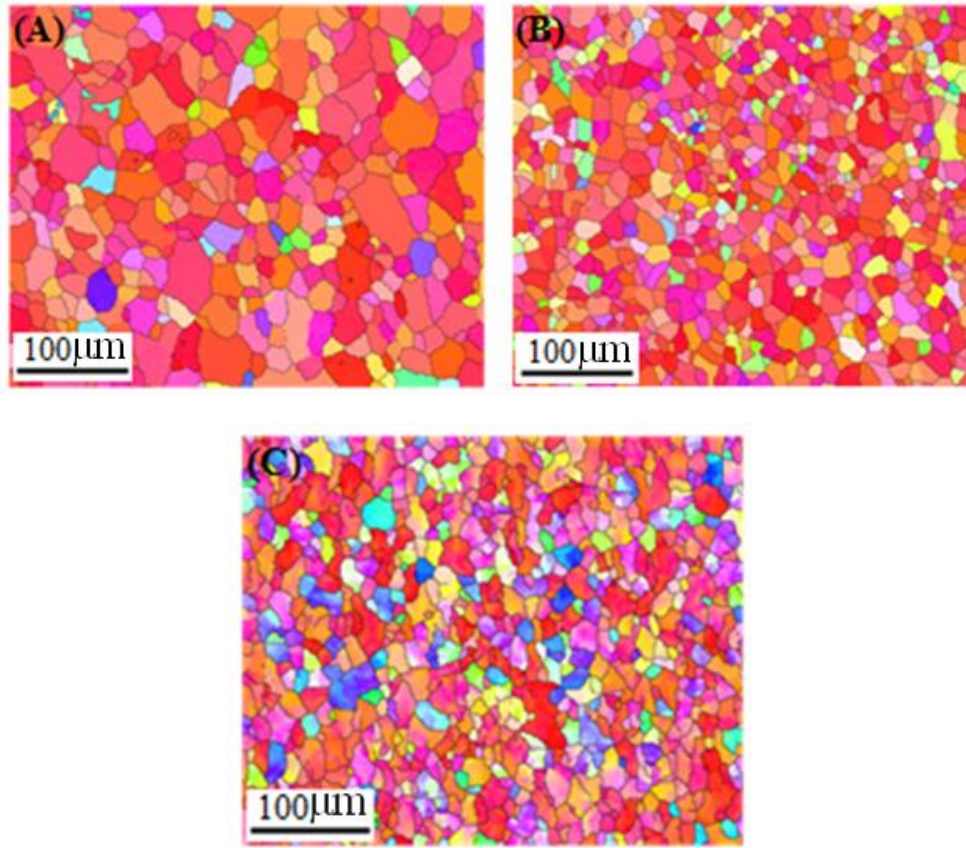


Fig. 3.3: Microstructure of the alloys: (A) SRS, (B) TRS and (C) LOS

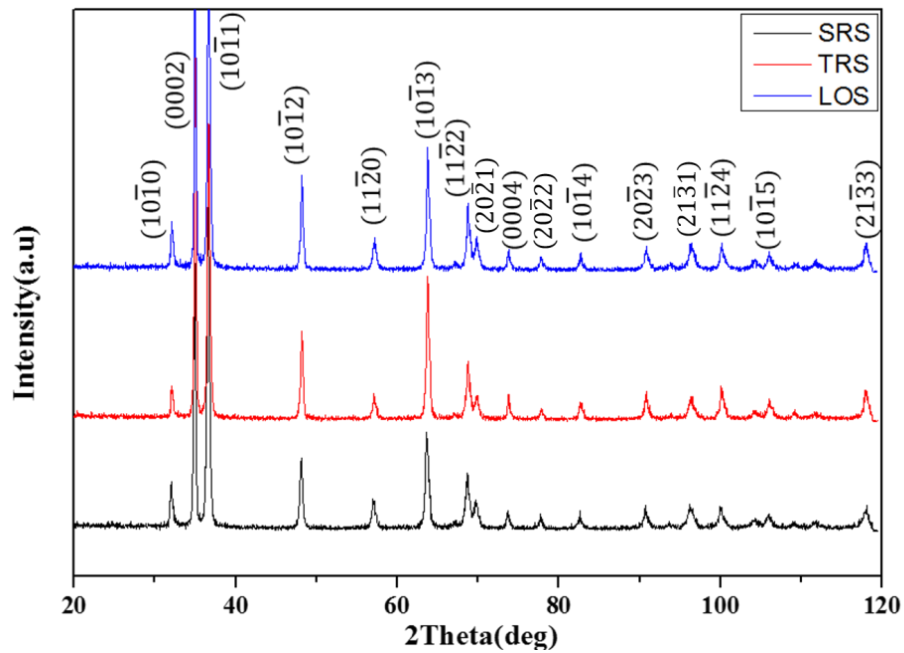


Fig. 3.4: XRD patterns of the SRS, TRS and LOS alloys

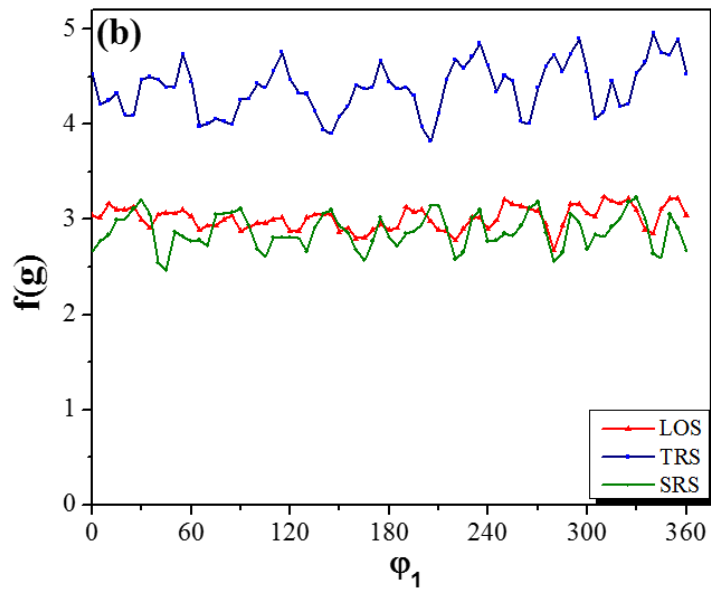
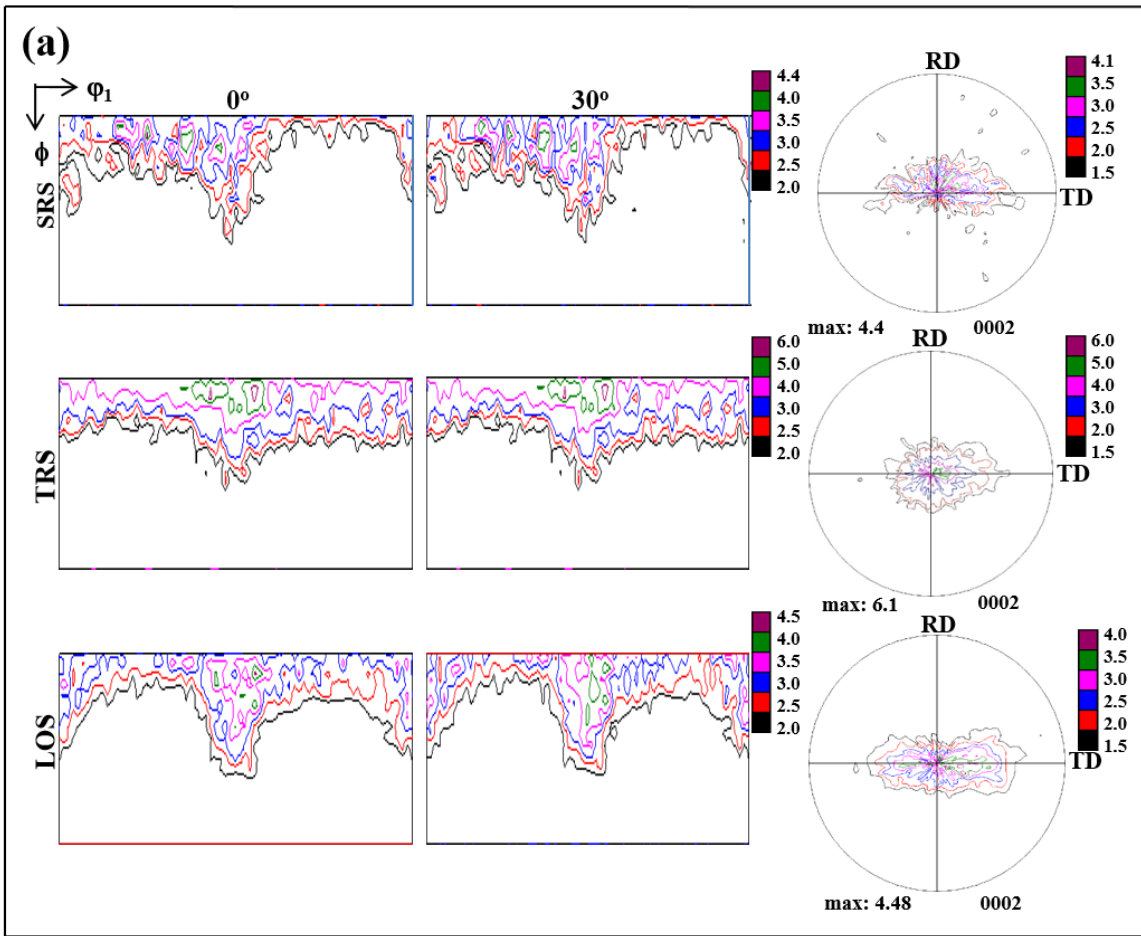


Fig. 3.5: Texture of all the three alloys (SRS, TRS and LOS): (a) ODF ( $\varphi_2 = 0^\circ$  and  $30^\circ$  sections) and (b)  $[0001] \parallel ND$  fibre plots.



### 3.3.2 Tensile properties of Zircaloy-4 at room temperature

The tensile properties of all the three alloys listed in Tables 3.3 – 3.5 and their variation with respect strain rate in L direction is shown in Fig.3.6. The TRS and LOS samples display overall high maximum strength and total percentage elongation values respectively. The  $\sigma_Y$  values are always maximum for all the alloys along T direction in all the three strain rates employed. On the other hand, the  $\sigma_{UTS}$  values do not exhibit significant variation as a function of sample orientation and strain rate. The total percentage elongation values are decreasing with increase in strain rate.

Table 3.3: Room temperature tensile properties of slab route sheet Zircaloy-4

Strain rate ( $s^{-1}$ )	Orientation	$\sigma_{YS}$ (MPa)	$\sigma_{UTS}$ (MPa)	Total Percent Elongation (%)	K	n	R <sup>2</sup>	A <sub>IP</sub>	$\delta$
0.001	L	318.66±0.07	455.62±0.01	27.94±0.02	722.70	0.145	0.999	10.706	0.161
	R	358.49±0.01	443.53±.02	30.22±0.08	746.15	0.139	0.999		
	T	379.17±0.02	438.65±0.01	27.16±0.07	631.36	0.098	0.998		
0.005	L	341.22±0.02	466.23±0.05	24.42±0.09	715.92	0.128	0.998	9.982	0.192
	R	374.65±0.08	451.78±0.09	27.14±0.02	639.94	0.094	0.995		
	T	397.63±0.01	454.22±.05	24.95±0.06	647.67	0.094	0.996		
0.01	L	340.87±0.07	468.12±0.09	23.43±0.02	718.90	0.123	0.999	11.279	0.114
	R	382.24±0.07	459.64±0.05	24.01±0.09	653.50	0.095	0.998		
	T	407.52±0.02	455.76±0.01	22.31±0.09	614.32	0.077	0.999		

Table 3.4: Room temperature tensile properties of tube route sheet Zircaloy-4

Strain rate ( $s^{-1}$ )	Orientation	$\sigma_{YS}$ (MPa)	$\sigma_{UTS}$ (MPa)	Total Percent Elongation (%)	K	n	R <sup>2</sup>	A <sub>IP</sub>	$\delta$
0.001	L	355.43±0.01	479.43±0.96	29.77±0.03	718.70	0.112	0.999	7.089	0.098
	R	387.6±0.07	471.67±0.03	27.84±0.07	674.77	0.098	0.998		
	T	399.86±0.01	464.90±0.07	26.9±0.09	653.17	0.090	0.997		
0.005	L	378.41±0.03	490.34±0.05	24.49±0.02	711.27	0.101	0.997	8.724	0.051
	R	399.09±0.02	477.45±0.02	22.11±0.07	672.66	0.089	0.998		
	T	425.90±0.03	482.87±0.07	24.49±0.08	673.89	0.088	0.998		
0.01	L	389.9±0.02	489.56±0.01	21.75±0.09	694.91	0.093	0.999	4.511	0.038

	R	404.45±0.07	486.77±0.07	21.70±0.08	678.40	0.087	0.998		
	T	415.94±0.08	473.89±0.02	22.93±0.07	650.35	0.081	0.999		

Table 3.5: Room temperature tensile properties of low oxygen Zircaloy-4

Strain rate (s <sup>-1</sup> )	Orientation	$\sigma_{YS}$ (MPa)	$\sigma_{UTS}$ (MPa)	Total Percent Elongation (%)	K	n	R <sup>2</sup>	A <sub>IP</sub>	$\delta$
0.001	L	330.77±0.09	473.78±0.05	29.58±0.07	746.48	0.139	0.999	13.748	0.234
	R	355.15±0.08	437.92±0.08	30.07±0.02	644.51	0.111	0.999		
	T	397.63±0.07	451.98±0.05	25.48±0.05	651.25	0.109	0.998		
0.005	L	338.44±0.03	481.90±0.01	25.25±0.08	729.72	0.118	0.999	12.261	0.148
	R	369.08±0.07	450.89±0.02	25.8±0.07	634.13	0.090	0.998		
	T	403.2±0.06	456.67±0.04	24.6±0.06	629.66	0.083	0.998		
0.01	L	344.707±0.09	483.65±0.04	23.79±0.07	738.32	0.122	0.999	11.446	0.233
	R	387.88±0.01	457.23±0.05	23.65±0.09	632.47	0.084	0.996		
	T	413.64±0.01	464.56±0.04	23.42±0.09	647.78	0.087	0.994		

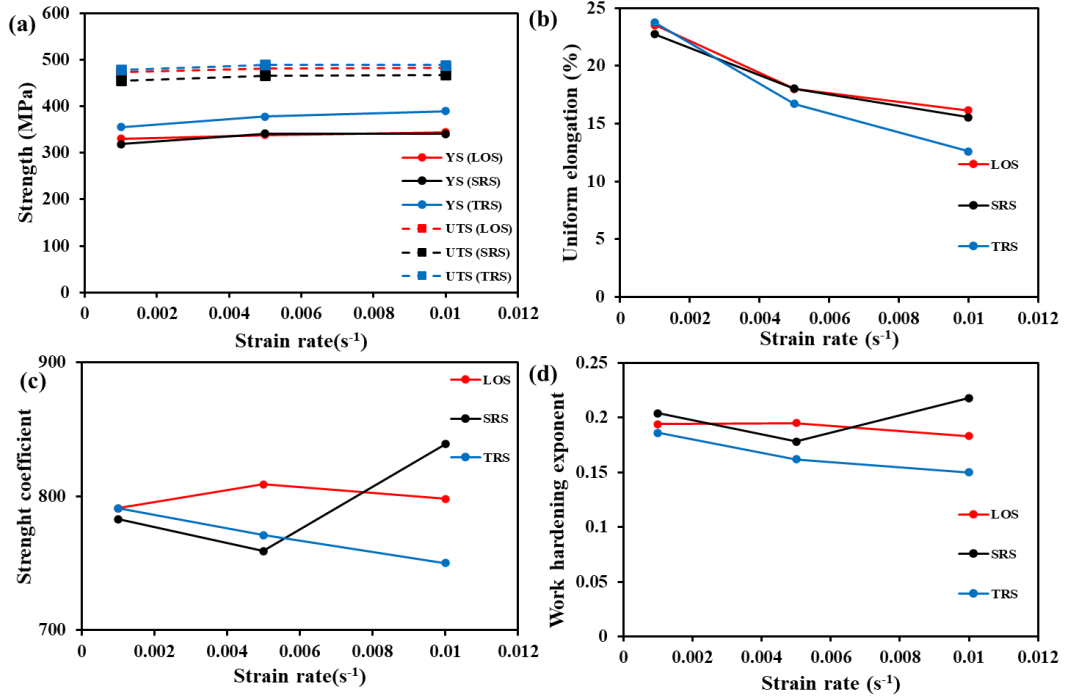


Fig. 3.6: Effect of strain rate on (a) strength (yield and ultimate), (b) uniform elongation, (c) strength coefficient, (d) work hardening exponent.

From Tables 3.3 – 3.5, it can be observed that the strength parameters ( $\sigma_Y$  and  $\sigma_{UTS}$ ) of TRS samples are higher than those of the SRS and LOS samples. In contrast, uniform elongation values of all the three alloys are nearly the same. The higher strength of TRS samples can be attributed to the relatively higher extent of deformation associated with the pilgering process. It also appears that the strain rates have marked influence on both the strength and ductility of the alloys. The strength parameters ( $\sigma_Y$  and  $\sigma_{UTS}$ ) and elongation values increase and decrease with an increase in strain rate correspondingly. The  $\sigma_Y$  values exhibit a systematic trend as a function of sample orientation irrespective of variation in strain rate. The  $\sigma_Y$  values are maximum and minimum along T and L directions respectively. This observation is not unexpected, since the yield strength is susceptible to the presence of crystallographic texture in the materials (Dieter and Bacon 1962). It is to be noted that the present alloys do exhibit the appearance of moderate-intensity texture. On the other hand, the  $\sigma_{UTS}$  and elongation values do not show systematic variation as a function of sample orientation.

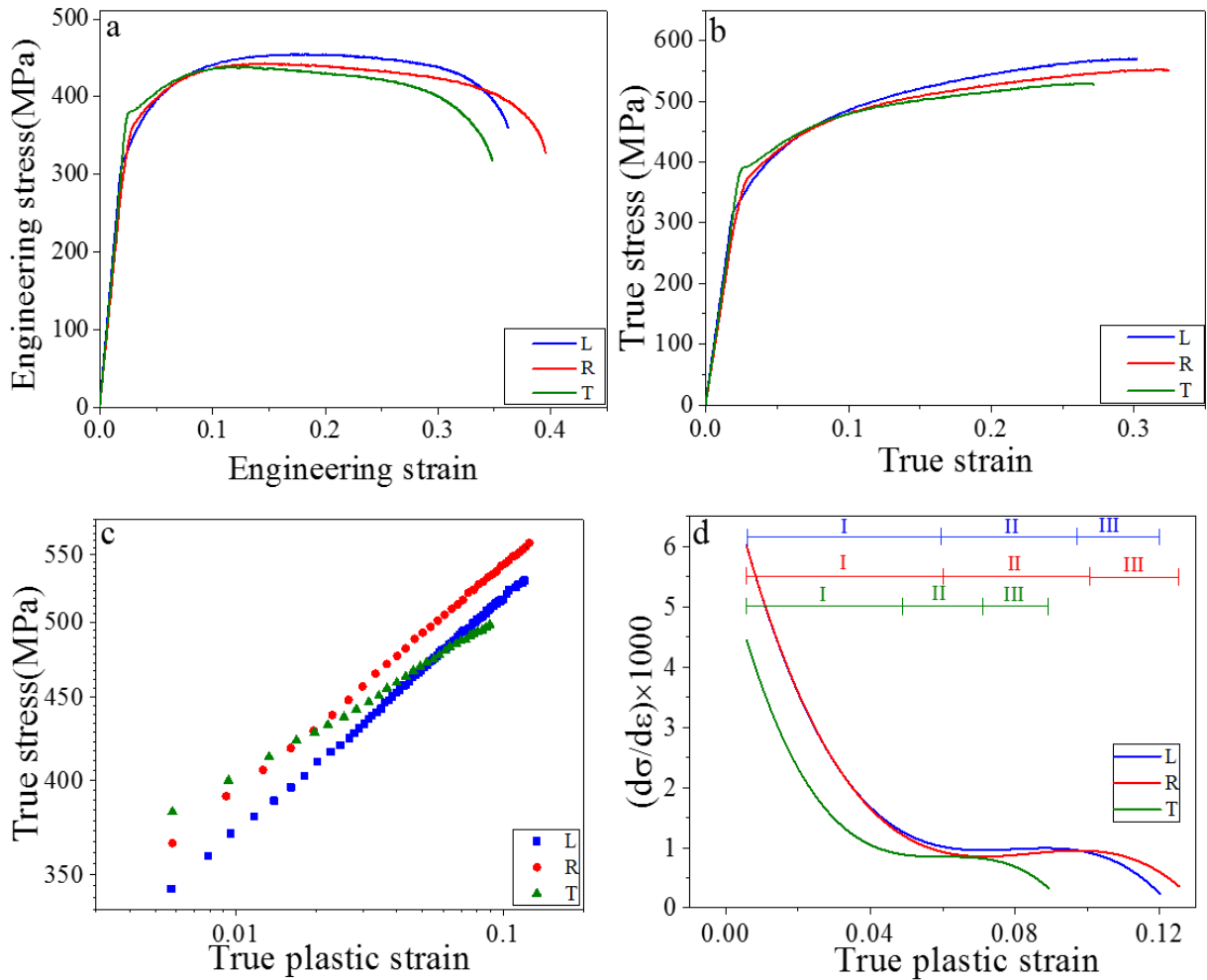


Fig. 3.7: Tensile properties of the sample SRS at  $0.001 \text{ s}^{-1}$  strain along L, R and T directions: (a) Engineering stress – Engineering strain curves, (b) True stress – True strain curves (c) True stress – True plastic strain and (d) Differential curves.

The nature of engineering and true stress-strain curves is the same for three alloys in all sample orientations and strain rates. It indicates continuous work hardening up to  $\sigma_{UTS}$  and subsequent softening till fracture. However, plastic flow paths between  $\sigma_Y$  and  $\sigma_{UTS}$  are different along three sample directions at all strain rates. It can attribute to both the orientation-dependent work hardening and lattice resistance (Peierls stress) provided by the solute atoms (Sn, Fe, Cr and O) which are responsible for influencing the entire stress-strain curve. It can be understood that the Peierls stress is the shear stress which is crystallographic directional dependent for dislocation movement [Dieter, 1988]. The directional dependence of engineering stress-strain curves of the present alloys can thus, attribute to moderate intensity texture present

in all the three alloys. Further, these results also reflect the directional dependence of engineering stress-strain curves which are independent of strain rates employed during tensile testing.

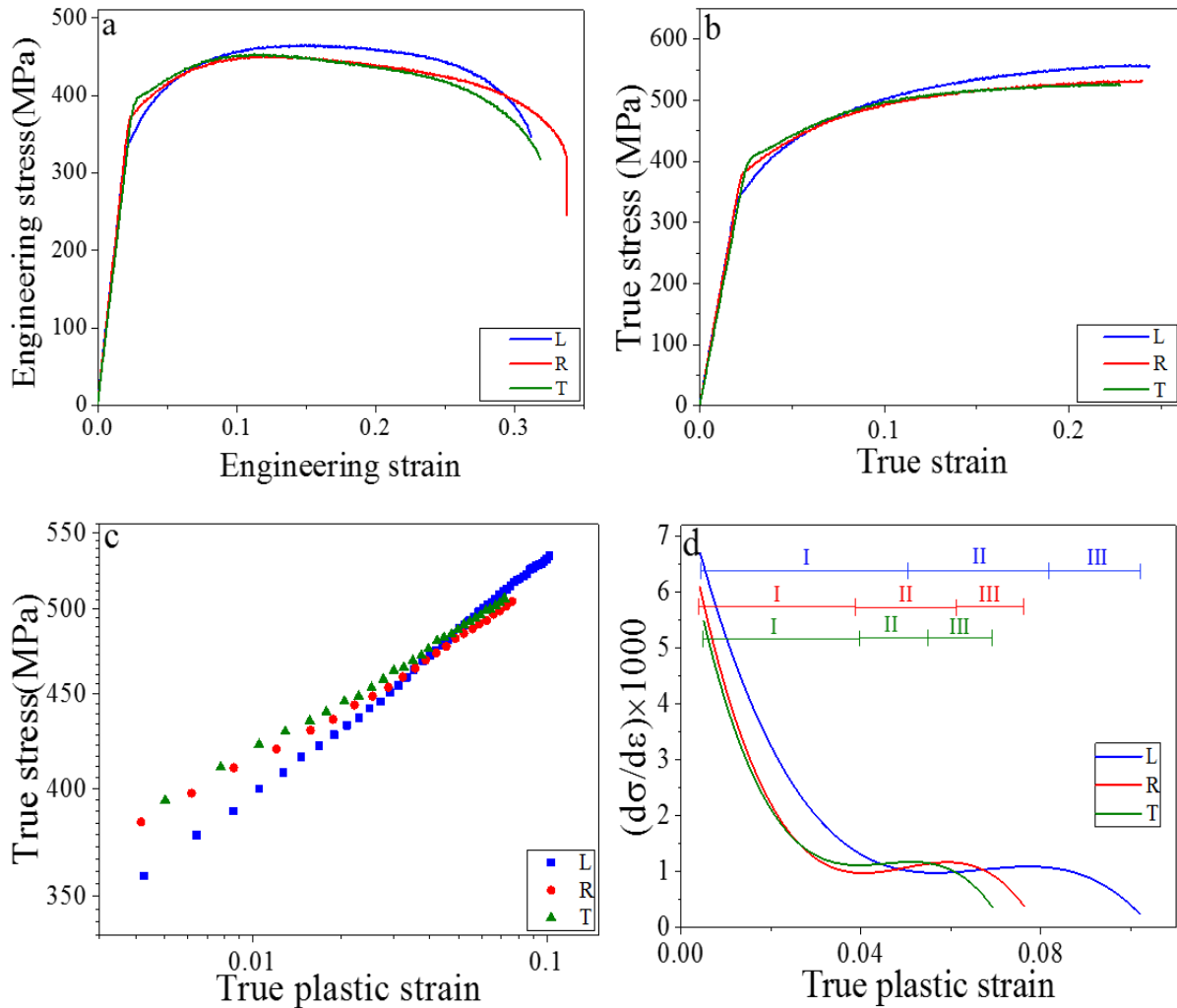


Fig. 3.8: Tensile properties of the sample SRS at  $0.005 \text{ s}^{-1}$  strain along L, R and T directions: (a) Engineering stress – Engineering strain curves, (b) True stress – True strain curves (c) Log True stress – Log True plastic strain and (d) Differential curves

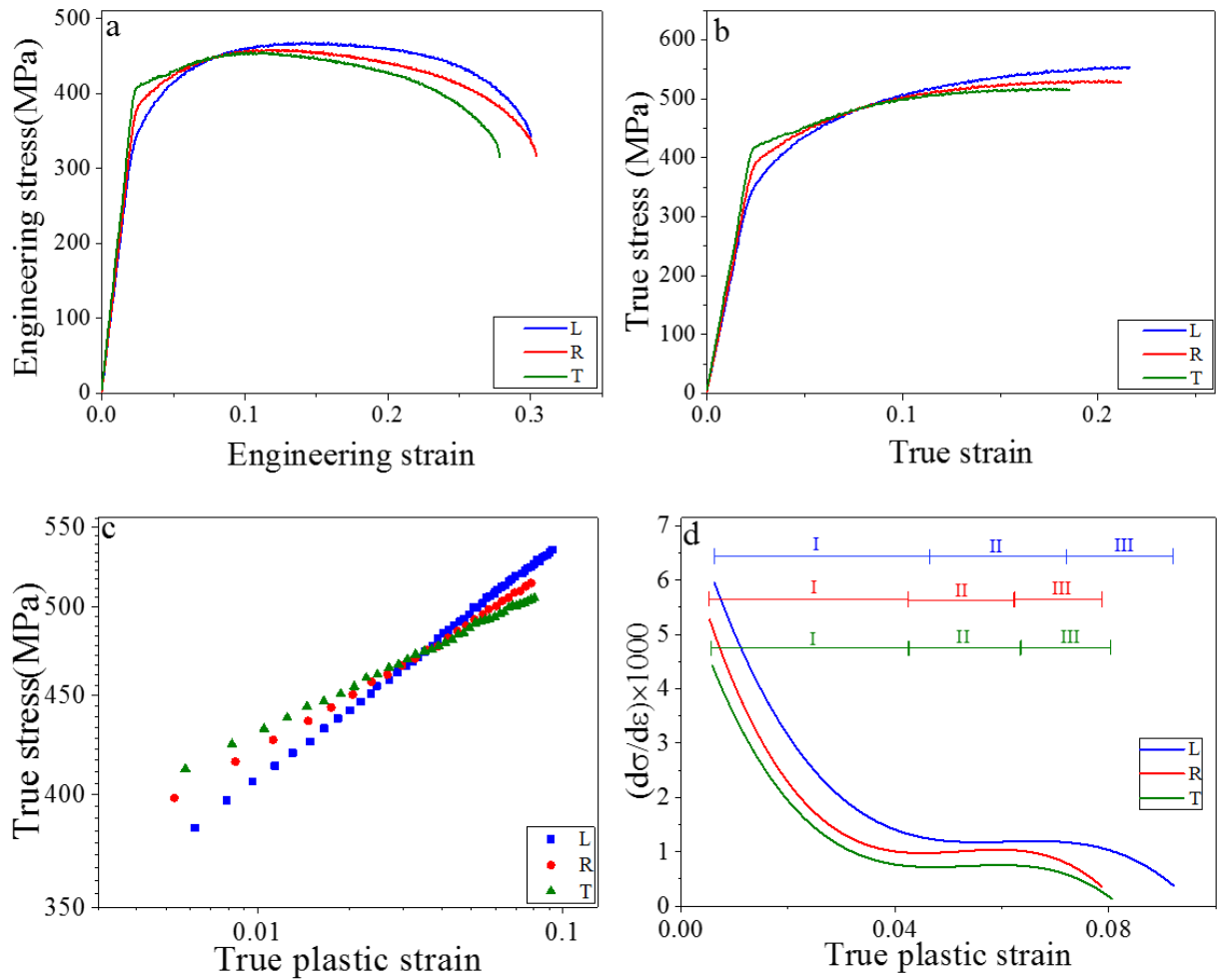


Fig. 3.9: Tensile properties of the sample SRS at  $0.01 \text{ s}^{-1}$  strain along L, R and T directions: (a) Engineering stress – Engineering strain curves, (b) True stress – True strain curves (c) Log True stress – Log True plastic strain and (d) Differential curves.

From Fig 3.7 -3.15, true stress-true plastic strain curves on log scales also display similar behaviour in all specimen orientations for all the three alloys. These curves exhibit straight lines indicating one deformation mechanism which occurs during the tensile test. To understand this, the true stress-true plastic strain curves are fitted using Hollomon constitutive equation (Zener and Hollomon 1944).

This relation can be written as:

$$\sigma = K\epsilon^n \quad (3.2)$$

where K and n are strength coefficient and strain hardening exponent, respectively.

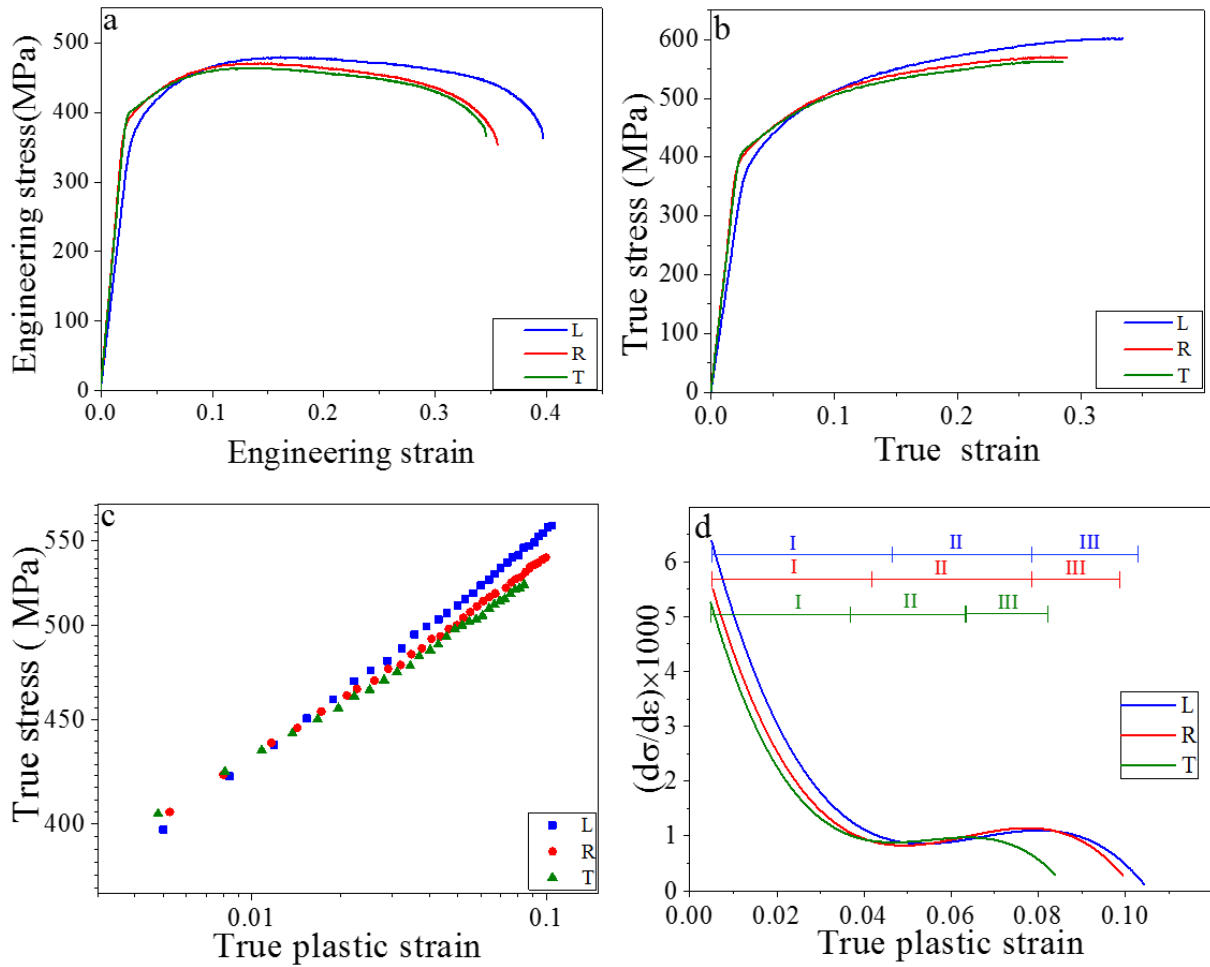


Fig. 3.10: Tensile properties of the sample TRS at  $0.001 \text{ s}^{-1}$  strain along L, R and T directions: (a) Engineering stress – Engineering strain curves, (b) True stress – True strain curves (c) Log True stress – Log True plastic strain and (d) Differential curves.

The flow curve parameters of all the three alloys derived using equation (2) and the corresponding values of fit parameters and resultant coefficient of determination ( $R^2$ ) are given in Table 3.3-3.5. It can be figured out that the values of  $R^2$  lie in the range of 0.994 to 0.999 indicating an excellent fit of data of the flow curves. Furthermore, this points out that a very large fraction of observed variations in true stress-true plastic strain can be accommodated in the fitted flow curves given by eq. (3.2).

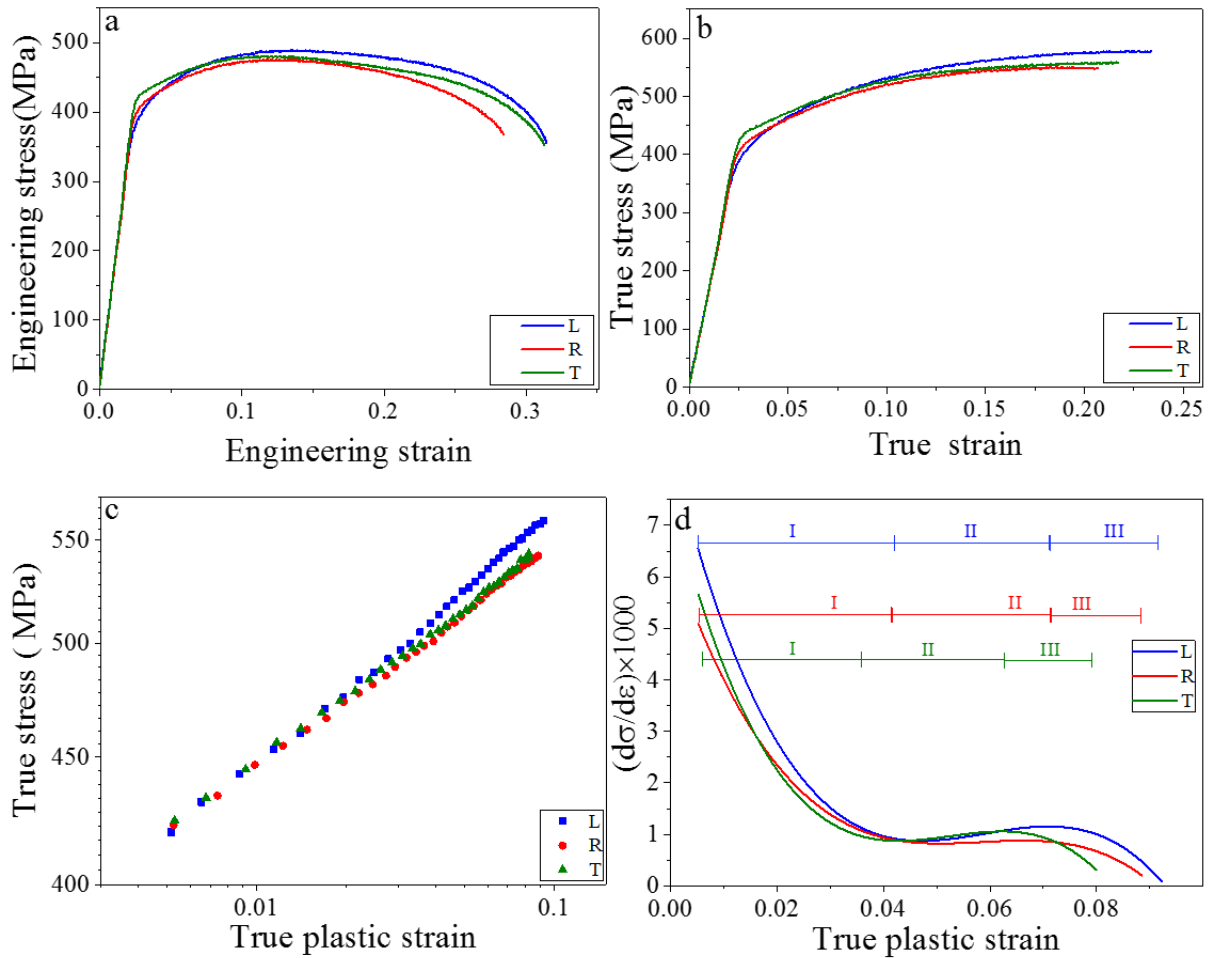


Fig. 3.11: Tensile properties of the sample TRS at  $0.005 \text{ s}^{-1}$  strain along L, R and T directions: (a) Engineering stress – Engineering strain curves, (b) True stress – True strain curves (c) Log True stress – Log True plastic strain and (d) Differential curves.

The values of K and n decrease from L to T directions except in alloy LOS at  $0.01 \text{ strain}$  rate. However, the n values display a systematic change as a function of strain rate. These results also reveal that the K and n values are sample orientation dependent. The n values decrease with increase in strain rates and are also associated with the ductility of the alloys. The higher n value corresponds to higher ductility.

The true stress – true strain and log true stress – log true plastic strain curves, in general, demonstrate qualitative information about the variation of work hardening rate during plastic flow. The instantaneous work hardening rate curves are constructed to have information regarding the quantitative description of work hardening rates. These curves also utilized to



address issues related to micro deformation mechanisms. These curves are obtained by numerically differentiating the true stress with respect to plastic strain values and are plotted against plastic strain or flow stress for all the sample orientations i.e. L, R and T.

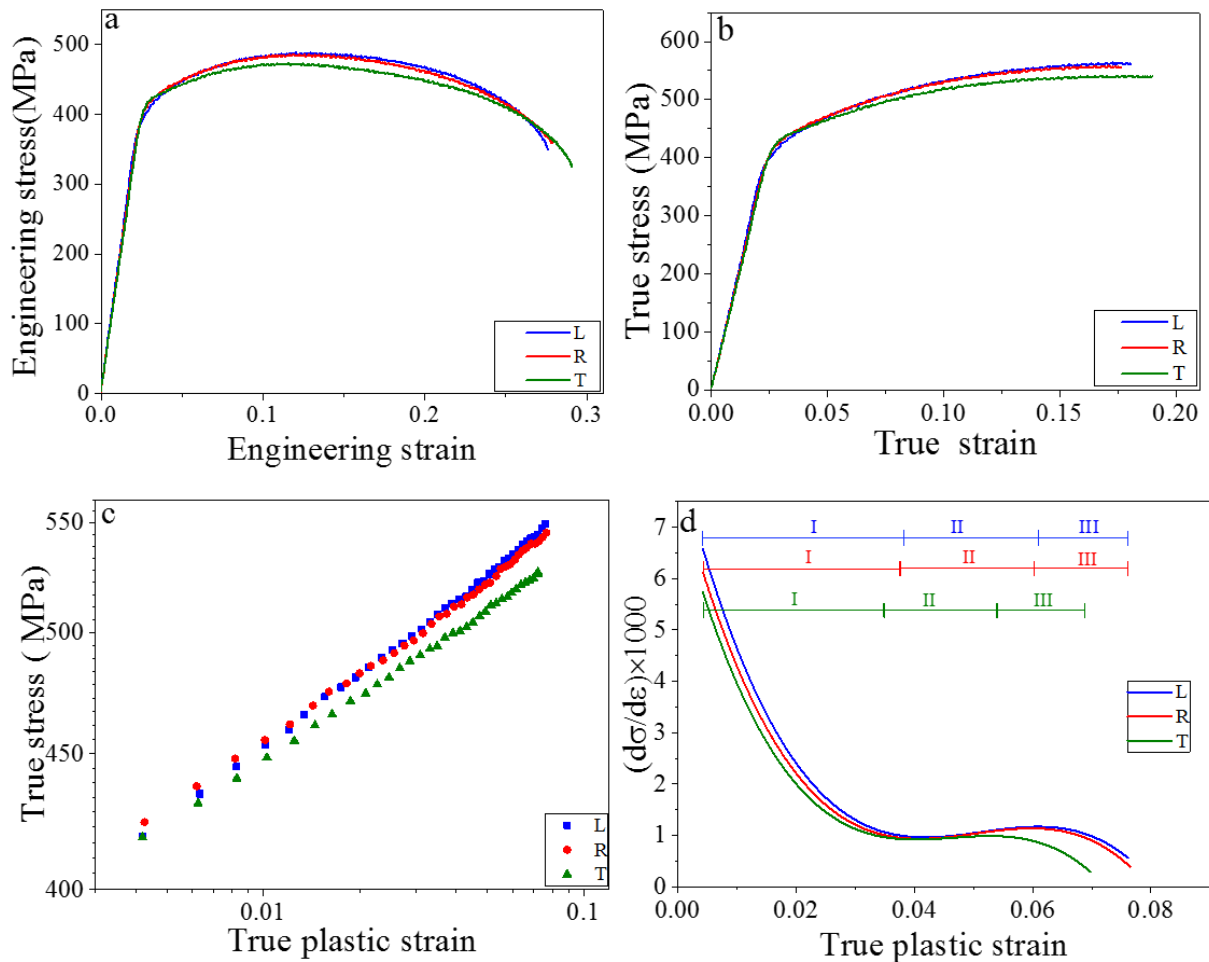
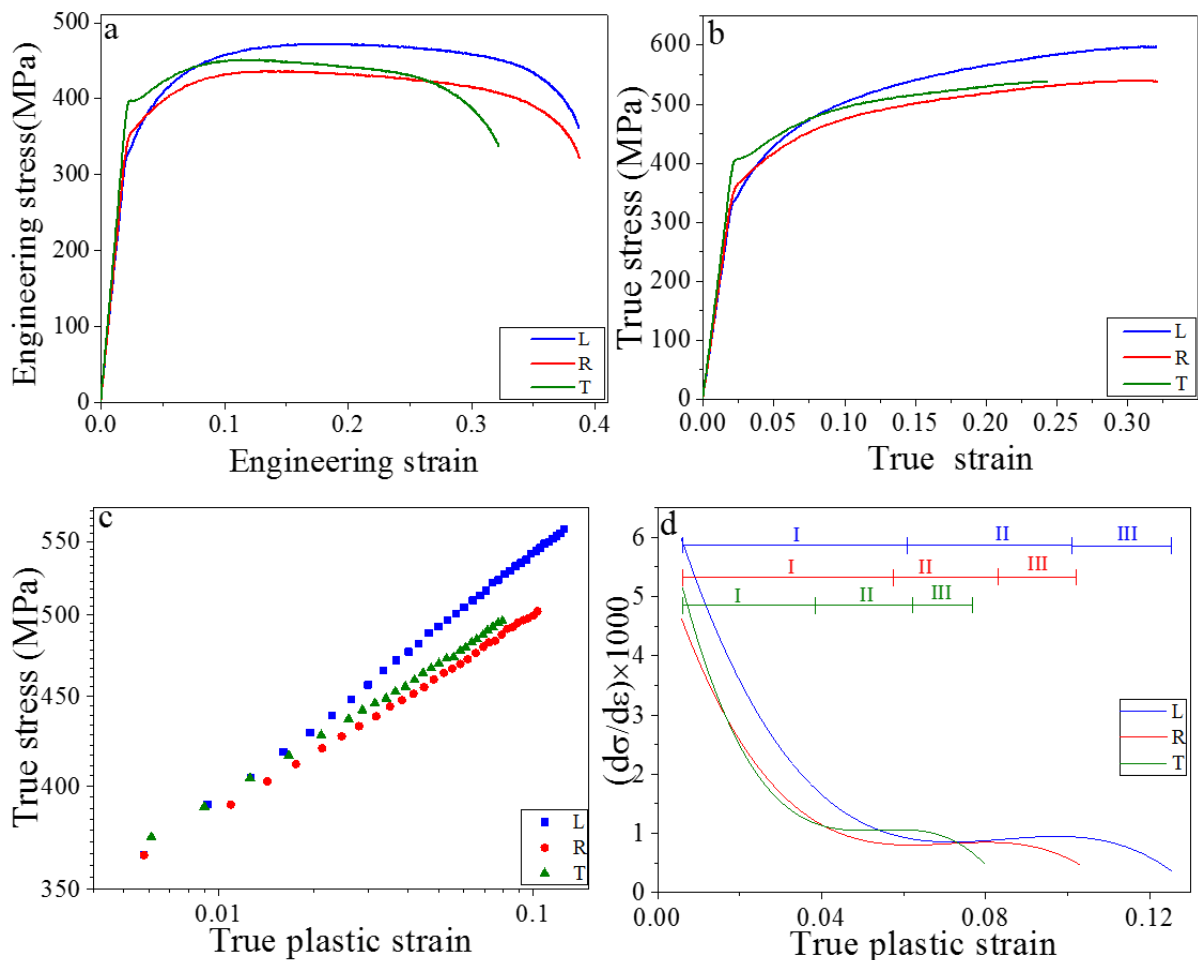


Fig. 3.12: Tensile properties of the sample TRS at  $0.01 \text{ s}^{-1}$  strain along L, R and T directions: (a) Engineering stress – Engineering strain curves, (b) True stress – True strain curves (c) True stress – True plastic strain and (d) Differential curves

The overall nature of instantaneous curves in the present alloy is nearly the same, although the curve paths are slightly different as observed in Fig. 3.7 – 3.15 (d). As discussed above, the divergent paths of instantaneous curves are due to the presence of moderate texture present in all the three experimental alloys. The differential curves can be divided into three distinct regimes (I, II and III) of work hardening rate. The stage I corresponds to the

elastoplastic transition of flow curves corresponding to a very rapid decrease in work hardening rate with increment in true plastic strain and flow stress. The regime I, in general associates with microstructural parameters such as grain size, grain shape, precipitates, solute atoms, subgrains, macro and micro textures and initial dislocation density (Mondal et al. 2013). The regime I of all the three alloys do not overlap instead follow slightly different paths attributing to different initial microstructures as well as solute contents of all the three alloys. As mentioned above, all three alloys exhibit a single crystal structure (hcp) in the corresponding XRD patterns.



*Fig. 3.13: Tensile properties of the sample LOS at  $0.001 \text{ s}^{-1}$  strain along L, R and T directions: (a) Engineering stress – Engineering strain curves, (b) True stress – True strain curves (c) Log True stress – Log True plastic strain and (d) Differential curves.*

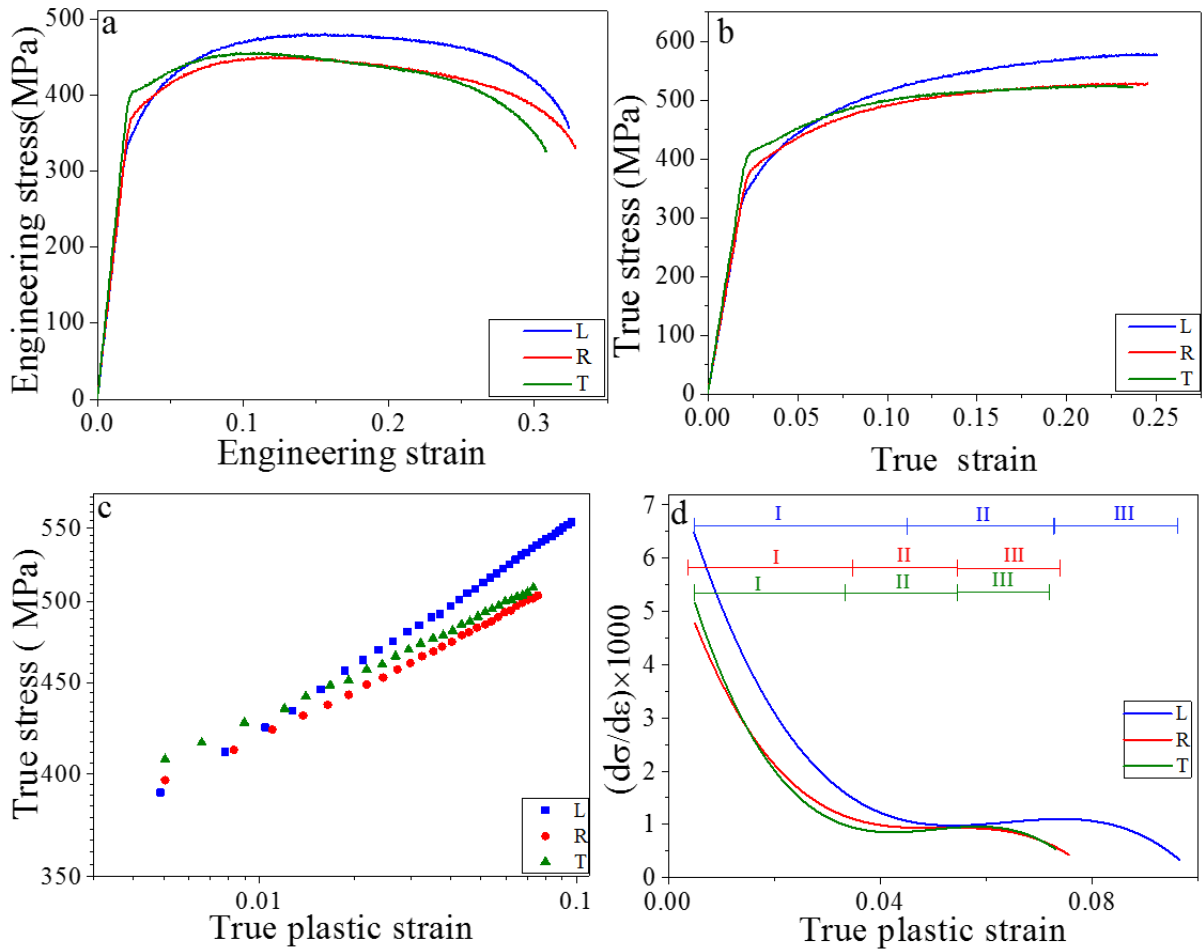


Fig. 3.14: Tensile properties of the sample LOS at  $0.005 \text{ s}^{-1}$  strain rate along L, R and T directions: (a) Engineering stress – Engineering strain curves, (b) True stress – True strain curves (c) True stress – True plastic strain and (d) Differential curves

The work hardening rate subsequently becomes almost constant in regime II (Figs. 3.6 -3.15 (d)). The flat regime II is maximum and minimum in L and T direction samples, respectively. This part of the curve is known as easy glide stage wherein local work hardening occurs due to planar slip movements. The regime II generally exhibits a constant value of  $d\sigma / d\varepsilon$  (i.e.  $\mu / 200$ ) where  $\mu$  is the shear modulus of the material (Keller, Hug, and Chateigner 2009). The calculated average values of the  $d\sigma / d\varepsilon$  are in agreement with  $\mu / 200$ . The flat nature of the regime II in the present study can ascribe to the movement of planar slip.

The regime III of the instantaneous curves is associated with stress at which dynamic recovery process starts with sufficient pile-up of dislocations. The nature of regime III of all

the three alloys is nearly the same except the slope of the linear part. The regime III exhibits a direct relationship between the hardening rate and flow stress at higher strain levels.

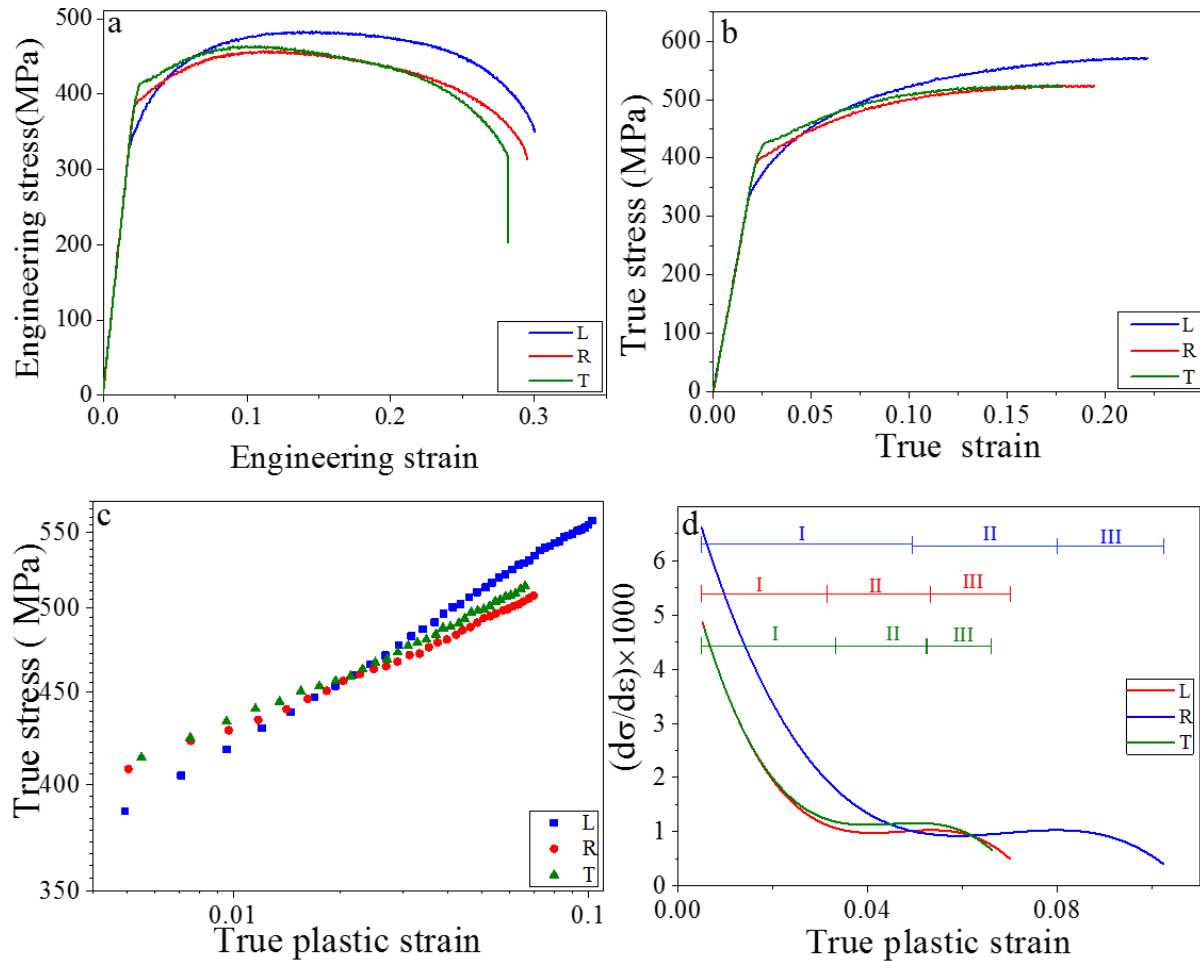


Fig. 3.15: Tensile properties of the sample LOS at  $0.01 \text{ s}^{-1}$  strain along with L, R and T directions: (a) Engineering stress – Engineering strain curves, (b) True stress – True strain curves (c) True stress – True plastic strain and (d) Differential curves.

### 3.3.3 Anisotropy of Zircaloy - 4 at room temperature and fractography

The anisotropy of as-received materials is calculated by “% in-plane anisotropy ( $A_{IP}$ )” (Banumathy, Mandal, and Singh 2009a) and “anisotropy index ( $\delta$ )” (Wu and Koo 1997). The  $A_{IP}$  and  $\delta$  values are associated with yield strength and elongation anisotropy, respectively.

$$A_{IP} = \frac{2 \times \sigma_{YS}(T) - \sigma_{YS}(L) - \sigma_{YS}(R)}{2 \times \sigma_{YS}(T)} \times 100 \quad (3.3)$$

This definition based on the values of  $\sigma_{YS}$  in different sample directions, are large along T sample direction for the present alloy. The eq. (3.3) shows that  $A_{IP}$  is zero for isotropic

materials and its value increases with an increase in the extent of anisotropy. The  $A_{IP}$  of the as-received material has been calculated and given in Tables 3.3 – 3.5.

Tensile anisotropy can also be estimated using the parameter “anisotropic index” as proposed by Wu and Koo (Wu and Koo 1997) which is defined as

$$\delta = \frac{|\% \epsilon_U (L) - \% \epsilon_U (T)|}{\% \epsilon_U (L) + \% \epsilon_U (T)} \times 100 \quad (3.4)$$

where  $\% \epsilon_U (L)$  and  $\% \epsilon_U (T)$  are the percentage uniform elongation of the tensile specimens along the L and T directions. The value of  $\delta$  is zero for isotropic materials where  $\% \epsilon_U (L) = \% \epsilon_U (T)$ . On the other hand, maximum value of  $\delta$  is 1 (100%) which corresponds to either  $\% \epsilon_U (L) \gg \% \epsilon_U (T)$  or  $\% \epsilon_U (T) \gg \% \epsilon_U (L)$ . The anisotropic index  $\delta$  for the present alloy has been calculated and given in Tables 3.3 – 3.5.

Both the anisotropy parameters do not exhibit a systematic trend with an increase in strain rate. However, all three alloys display moderate values of both the parameters at all the strain rates. In LOS samples the  $A_{IP}$  and  $\delta$  are maximum of 13.75 and 0.23 respectively at a strain rate of  $0.001s^{-1}$ . These moderate values of anisotropy parameters in present alloys thus be attributed to the presence of moderate-intensity texture in SRS, TRS and LOS materials.

As mentioned above, all the post tensile test fracture surfaces of the materials display ductile dimples in the SEM images (Fig. 3.16 - 3.18) and the effect of strain rate on fracture behaviour is almost invisible on all the three alloys. The images illustrate the size of the dimples and length of tear ridges are larger and smaller in the case of TRS as compared to that of the other two. The larger tear ridges, the white portion in the image of fractography, indicate more ductility of the materials, which in turn are attributed to less degree of deformation in the case of SRS and LOS.

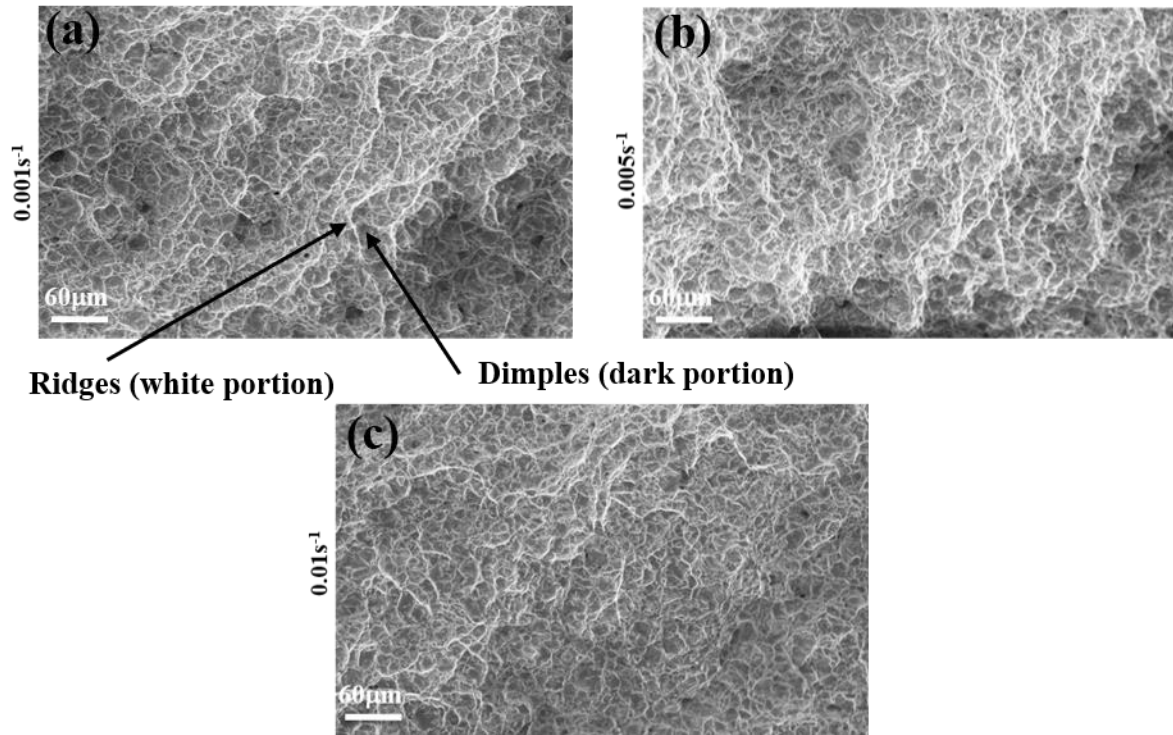


Fig. 3.16: The fracture surface of SRS tensile samples along L direction with different strain rates: (a) 0.001, (b) 0.005 and (c) 0.01 s<sup>-1</sup>.

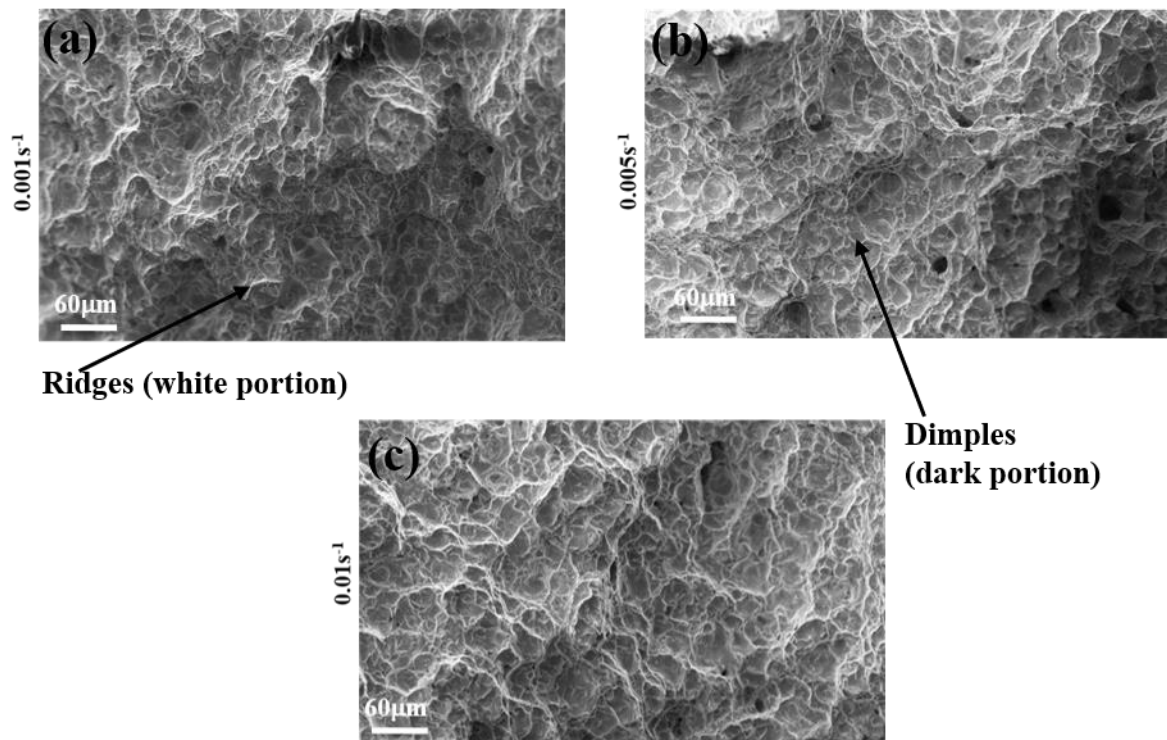


Fig. 3.17: The fracture surface of TRS tensile samples along L direction with different strain rates: (a) 0.001, (b) 0.005 and (c) 0.01 s<sup>-1</sup>.

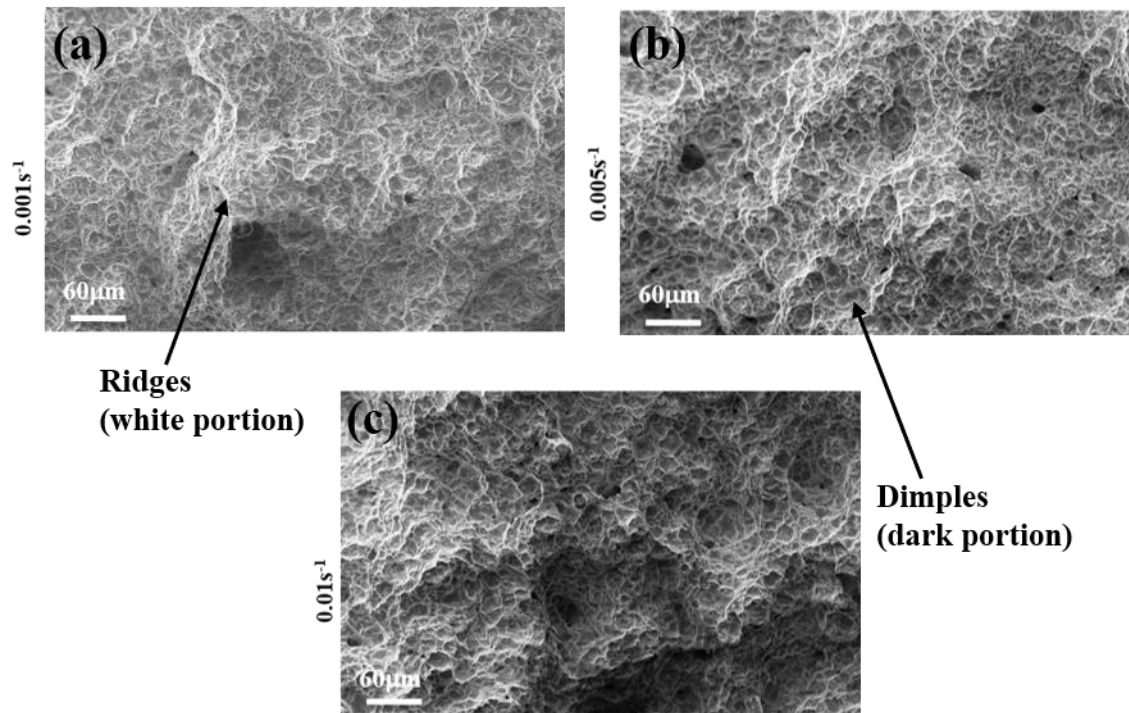


Fig. 3.18: The fracture surface of LOS tensile samples along L direction with different strain rates: (a) 0.001, (b) 0.005 and (c) 0.01  $s^{-1}$ .

### 3.4 Summary

A correlation between texture and sample orientation-based flow parameters has been established in three different Zircaloy-4 sheet materials.

- All the three samples exhibit the presence of moderate texture. The intensity is maximum in TRS samples in comparison to those of the SRS and LOS.
- With an increase in strain rate, the strength parameters ( $\sigma_Y$  and  $\sigma_{UTS}$ ) increased while elongation values decreased.
- Present alloys show moderate values of anisotropy parameters ( $A_{IP}$  and  $\delta$ ) values.
- The flow behaviour of the alloys follow a typical Holloman equation.
- The instantaneous work hardening rate curves of the present alloys exhibit all the three typical regimes (i.e. regime I, regime II and regime III)

Hence, the tensile properties of Zircaloy-4 and their correlation with applied load direction, texture and strain rate at room temperature are explained. The tensile properties at high temperature are explained in the next chapter.



## Chapter 4

# Orientation dependent tensile flow behaviour of Zircaloy-4 at elevated temperatures

### 4.1 Introduction

The tensile properties of the Zircaloy-4 were studied by Grigoriev et al in 2012 and Shinozaki in 2016. But it is very limited. Therefore, the present research focuses on studying the orientation-dependent tensile flow behaviour of Zircaloy-4 at elevated temperatures in relation to the processing routes. Three different Zircaloy-4 sheet materials in three different directions are tested under uniaxial tension at elevated temperatures between 298K and 423K with an increment of 75K, to investigate the tensile properties and their anisotropy. The texture of these alloys processed by different routes are studied in terms of pole figures and ODF's using XRD and the results are correlated with the tensile properties. Fracture surface morphology of post tensile test samples are studied using SEM.

### 4.2 Experimental details

#### 4.2.1 Materials used

Nuclear Fuel Complex, Hyderabad, India uses three types of Zircaloy-4 sheet materials namely, slab route sheet (SRS), tube route sheet (TRS) and Low oxygen sheet (LOS) for manufacturing varied sizes of sheets for spacer grid applications. The SRS and TRS sheet materials produced by normal rolling and pilgering processes. The LOS is a typically rolled sheet with relatively low Oxygen content in comparison to those of SRS and TRS. The chemical composition of different Zircaloy-4 sheets is given in Table 3.1.

#### 4.2.2 Experimental procedure of texture analysis at elevated temperatures.

An Inel equinox diffractometer with Cu K $\alpha$  radiation equipped with a position-sensitive detector has been used to perform X-ray diffraction (XRD) studies on the samples. The samples of sheet materials were taken from the gripping head of post tensile test samples so that the ambient conditions of tensile samples and XRD samples were the same. Hence correlating their results becomes easy. The size of the specimen used for texture measurements is 25×15mm, followed from Schulz reflection technique (Talia and Povolo 1977), An Inel G3000 texture goniometer coupled with curved position sensitive detector has been employed in texture measurements. {10 $\bar{1}$ 0}, {0002}, {10 $\bar{1}$ 1}, {10 $\bar{1}$ 2} and {10 $\bar{1}$ 3} incomplete pole figures were measured from 1/2 thickness level of the normal direction (ND) plane. The enhancement of measured area is obtained by employing an oscillation stage with 20mm specimen translation. Complete Orientation Distribution Function (ODF) plots have taken from the pole figure data. The results of {0002} pole figures and ODF plots of constant  $\varphi_2$  sections ( $0^\circ$  and  $30^\circ$ ) with iso-intensity contours in the Euler space are well-defined by three Euler angles ( $\varphi_1$ ,  $\Phi$ ,  $\varphi_2$ ).

#### 4.2.3 Experimental procedure for tensile tests at elevated temperatures

The tensile properties of the three Zircaloy-4 sheet materials were evaluated at elevated temperatures in three different directions, namely the Longitudinal (L or  $0^\circ$ ), Radial (R or  $45^\circ$  or specimen axis at  $45^\circ$  to the rolling direction) and Transverse (T or  $90^\circ$ ) directions. The longitudinal direction is same as rolling direction (RD) whereas the transverse is perpendicular to the rolling direction. Tensile tests were performed at temperatures 298K, 423K and 498K at a constant strain rate of  $0.001\text{s}^{-1}$  on a Bangalore integrated system software (BISS) servo electric hot forming machine (Electra-50) with 50kN capacity as per ASTM E8 standards. The servo electric hot forming machine setup and tensile test sample are shown in previous chapter 3 (Fig. 3.1 and Fig. 3.2). Three specimens were tested for each set of test parameters. The

resultant average values of yield strength ( $\sigma_Y$ ), ultimate tensile strength ( $\sigma_{UTS}$ ) and % elongation are reported in Tables 4.1-4.3.

### 4.3 Results and discussion

#### 4.3.1 Texture analysis of Zircaloy - 4

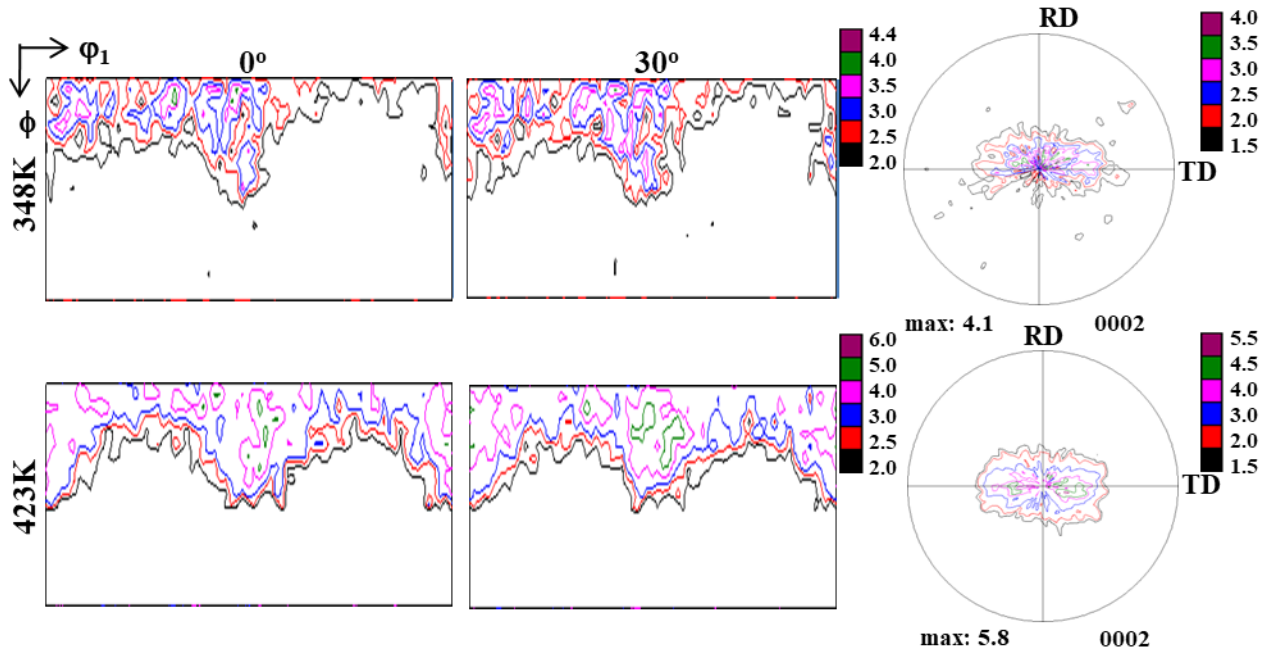


Fig. 4.1: Texture of SRS in terms of ODF sections ( $\varphi_2 = 0^\circ$  and  $30^\circ$ ) and test temperatures (348K and 423K).

The texture of all the three materials at two different temperatures are illustrated in terms of  $\{0002\}$  pole figures and ODF plots ( $\varphi_2 = 0^\circ$  and  $30^\circ$  sections) as shown in Figs. 4.1 – 4.3. The LOS sample shows maximum intensity among the three. The basal pole figures do not exhibit perfect c-type texture i.e., pole in basal pole figure is located at  $(0^\circ, 0^\circ)$ . The location of the poles in basal pole diagrams are  $(4.4^\circ, 59.9^\circ)$ ,  $(19.5^\circ, 105.9^\circ)$ ;  $(19.6^\circ, 98.1^\circ)$ ,  $(5.4^\circ, 87.9^\circ)$ ;  $(25.0^\circ, 100.4^\circ)$ ,  $(0^\circ, 0^\circ)$  in SRS, TRS and LOS at 348K and 423K respectively. Similarly, the location of main texture components in ODF are  $(\varphi_1=150.0^\circ, \Phi = 5.0^\circ, \varphi_2 = 20.0^\circ [f(g) = 4.5])$ ,  $(\varphi_1= 195.0^\circ, \Phi= 20.0^\circ, \varphi_2 =20.0^\circ [f(g) = 6.4])$ ;  $(\varphi_1= 180.0^\circ, \Phi = 8.8^\circ, \varphi_2 = 55.0^\circ [f(g) = 6.4])$ ,  $(\varphi_1=174.7^\circ, \Phi = 5.0^\circ, \varphi_2 = 45.0^\circ [f(g) = 6.0])$ ; and  $(\varphi_1= 190.^\circ, \Phi= 25.0^\circ, \varphi_2 =15.0^\circ [f(g) = 5.4])$ ,  $(\varphi_1= 200.0^\circ, \Phi = 0.0^\circ, \varphi_2 = 5.0^\circ [f(g) = 17.4])$  in SRS, TRS and LOS at

348K and 423K respectively. The intensities of the texture components (f (g)) are reported in terms of “times random”. The subsequent [0001]||ND fibre plots are depicted in Fig 4.4. The 423K plot display more intensity in LOS compared to that of SRS and TRS.

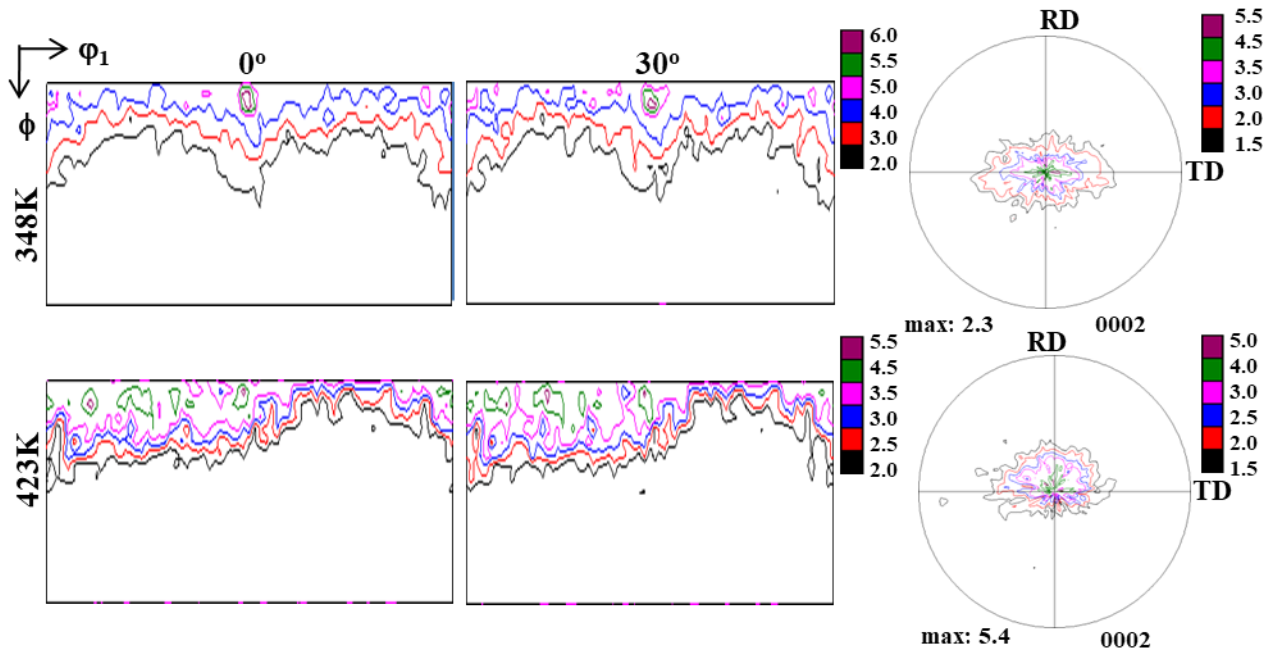


Fig. 4.2: Texture of TRS in terms of ODF sections ( $\varphi_2 = 0^\circ$  and  $30^\circ$ ) and test temperatures (348K and 423K).

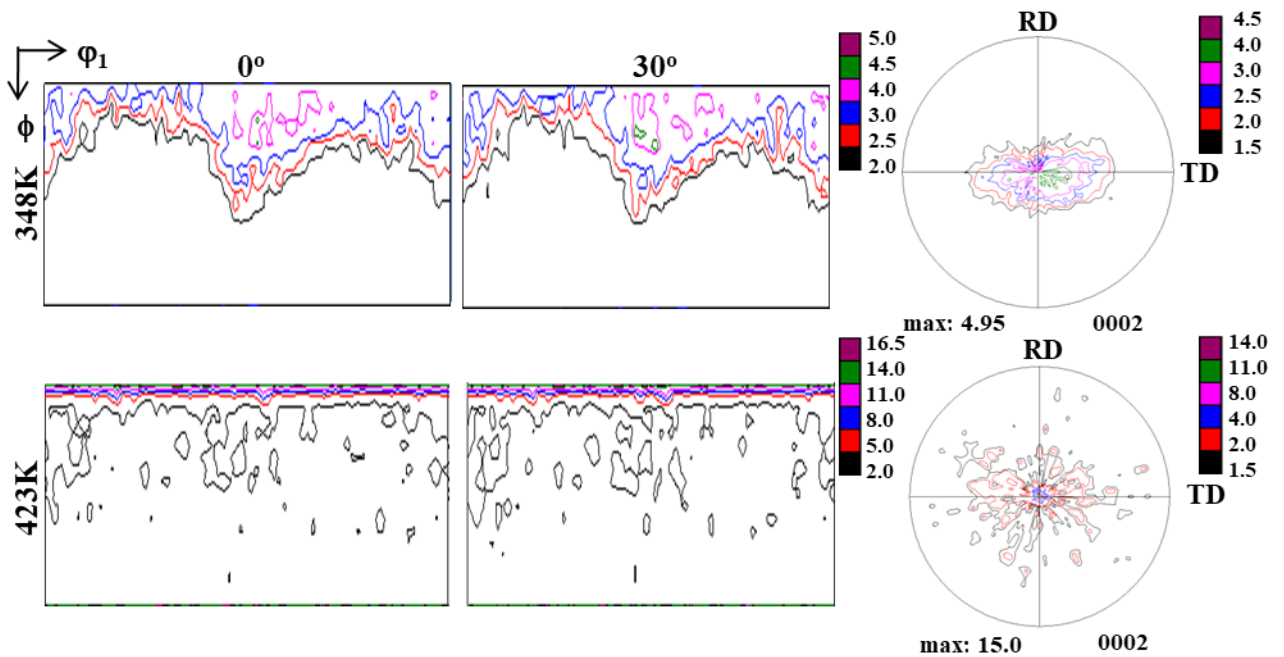


Fig. 4.3: Texture of LOS in terms of ODF sections ( $\varphi_2 = 0^\circ$  and  $30^\circ$ ) and test temperatures (348K and 423K).

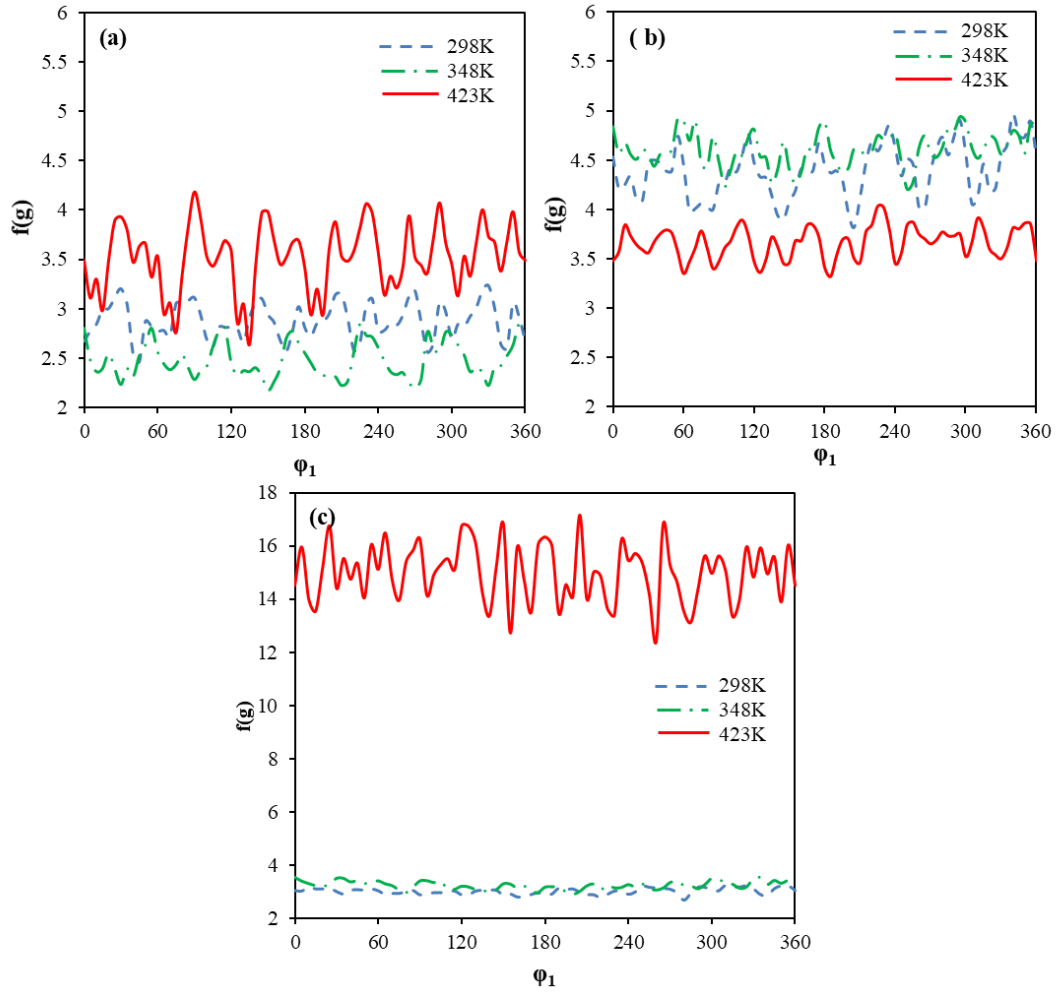


Fig. 4.4: Texture in terms of  $[0001] \parallel ND$  fibre plots at different temperature: (a) SRS, (b) TRS and (c) LOS.

The ODF sections and  $[0001] \parallel ND$  indicates that LOS has a maximum intensity at 423K, and it is almost three times more than that of SRS and TRS (Fig. 4.1 – 4.4). It is important to note here that the LOS has variation in chemical content when compared to others. The maximum intensity in the LOS can therefore be attributed to the lower Oxygen content. This can also be seen in the strength parameters that the LOS displays higher yield strength at 423K than that of the others. As a result, there was no significant variation found in intensities of SRS and TRS samples.

### 4.3.2 Tensile properties of Zircaloy-4 at elevated temperatures

The tensile properties of the material with respect to temperature and sample direction are listed in Table 4.1-4.3 and their variation with respect to temperature in L direction is shown in Fig. 4.5. The orientation-dependent tensile flow behaviour in terms of engineering stress – engineering strain, true stress – true strain, log true plastic stress – log true plastic strain and derivative curves of all the three alloys are depicted in Fig. 4.6 - 4.14. It is observed that out of these three alloys LOS and TRS alloys show higher ultimate tensile strength and percentage elongations. In all the three alloys, irrespective of temperature variation, the yield stress( $\sigma_y$ ) is more in T sample direction compared to the other two directions. The  $\sigma_{UTS}$  values do not show any specific trend with sample direction. The percentage of elongation values increase with increasing temperature and do not display a specific trend with the sample direction.

*Table 4.1: Tensile properties and anisotropy parameters of slab route sheet*

Temp (K)	O	$\sigma_{ys}$ (MPa)	$\sigma_{UTS}$ (MPa)	% $\epsilon_U$	K	n	R <sup>2</sup>	A <sub>IP</sub>	$\delta$
348	L	297.91±0.01	421.31±0.03	30.7±0.01	666	0.14624	0.99399	11.19565	0.026
	R	328.12±0.08	403.10±0.05	32.5±0.03	597	0.11748	0.99959		
	T	352.21±0.02	354.91±0.09	29.16±0.01	571	0.09353	0.99129		
423	L	258.12±0.02	363.22±0.06	35.78±0.09	580	0.15201	0.99768	7.824428	0.0113
	R	280.30±0.08	339.80±0.07	37.18±0.07	513	0.12439	0.99764		
	T	291.81±0.02	335.21±0.08	34.6±0.05	484	0.10493	0.99584		
498	L	214.11±0.01	304.14±0.02	36.21±0.02	501	0.16358	0.99896	7.126437	0.0131
	R	235.91±0.09	281.12±0.09	37.3±0.09	426	0.12714	0.99851		
	T	242.40±0.02	286.70±0.06	35.27±0.01	425	0.11327	0.99439		

Temp\* is temperature, O\* is Orientation of sample

Table 4.2: Tensile properties and anisotropy parameters of tube route sheet

Temp (K)	O	$\sigma_{YS}$ (MPa)	$\sigma_{UTS}$ (MPa)	% $\epsilon_U$	K	n	R <sup>2</sup>	A <sub>IP</sub>	$\delta$
348	L	328.21±0.08	421.14±0.08	26.93±0.01	645	0.12248	0.99299	5.217391	0.0556
	R	340.10±0.09	403.30±0.06	30.42±0.02	610	0.11191	0.99402		
	T	351.82±0.03	407.31±0.05	30.1±0.01	584	0.09587	0.99049		
423	L	283.22±0.08	362.92±0.09	33.91±0.09	564	0.12543	0.99389	5.808081	0.0244
	R	289.41±0.06	340.13±0.07	33.82±0.06	520	0.11444	0.98593		
	T	303.30±0.02	335.14±0.03	35.61±0.02	498	0.09845	0.99497		
498	L	225.10±0.03	304.20±0.05	36.17±0.03	456	0.13185	0.99591	4.166666	0.0210
	R	232.73±0.05	281.11±0.09	36.56±0.08	408	0.12819	0.99039		
	T	239.32±0.08	287.22±0.08	37.72±0.09	403	0.08966	0.99376		
Temp* is temperature, O* is Orientation of sample									

Table 4.3: Tensile properties and anisotropy parameters of low oxygen sheet

Temp (K)	O	$\sigma_{YS}$ (MPa)	$\sigma_{UTS}$ (MPa)	% $\epsilon_U$	K	n	R <sup>2</sup>	A <sub>IP</sub>	$\delta$
348	L	301.13±0.07	433.11±0.09	30.83±0.09	693	0.15259	0.99763	13.24942	0.0814
	R	324.30±0.09	399.21±0.08	32.13±0.09	592	0.11726	0.99147		
	T	360.12±0.08	411.32±0.07	26.19±0.07	580	0.0974	0.99629		
423	L	266.00±0.04	377.89±0.09	32.96±0.09	607	0.15385	0.99921	9.074074	0.0504
	R	281.14±0.03	336.31±0.02	36.59±0.09	498	0.11893	0.9953		
	T	301.22±0.01	343.97±0.03	36.46±0.07	496	0.1046	0.99248		
498	L	221.13±0.07	309.87±0.08	35.74±0.09	503	0.16167	0.99925	12.90672	0.0265
	R	227.24±0.06	275.11±0.09	37.24±0.09	415	0.12758	0.99744		
	T	257.14±0.03	285.99±0.08	37.68±0.07	413	0.11372	0.99588		
Temp* is temperature, O* is Orientation of sample									

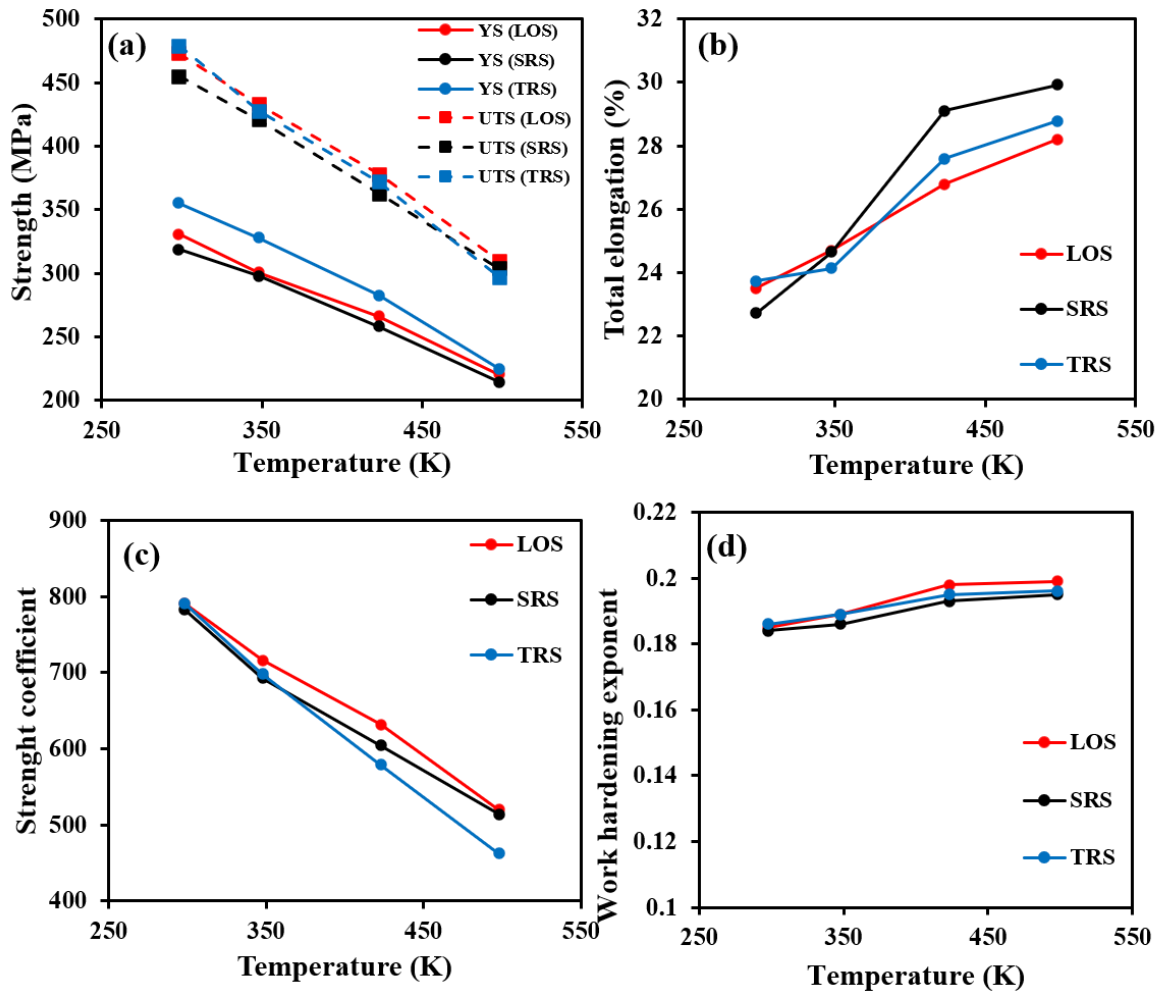


Fig. 4.5: Effect of temperature on (a) strength (yield and ultimate), (b) total elongation, (c) strength coefficient, (d) work hardening exponent



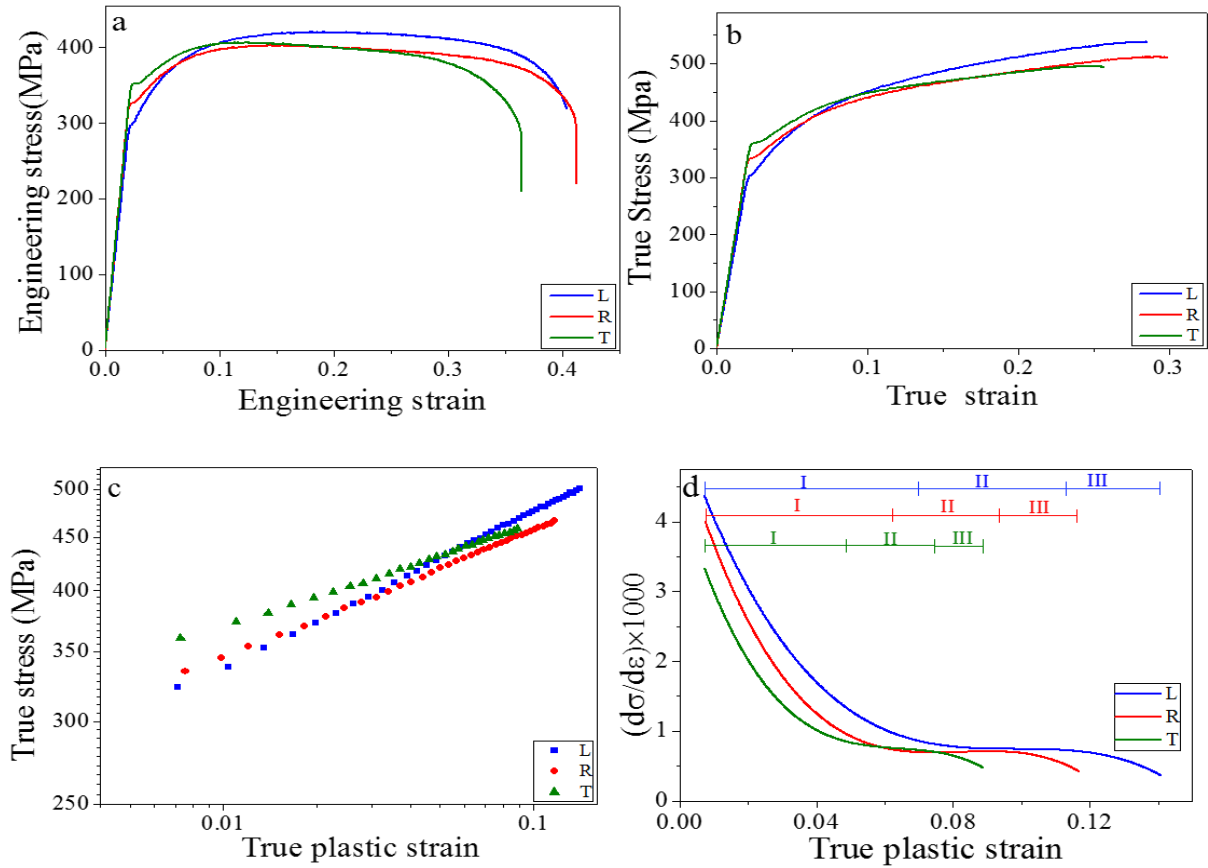
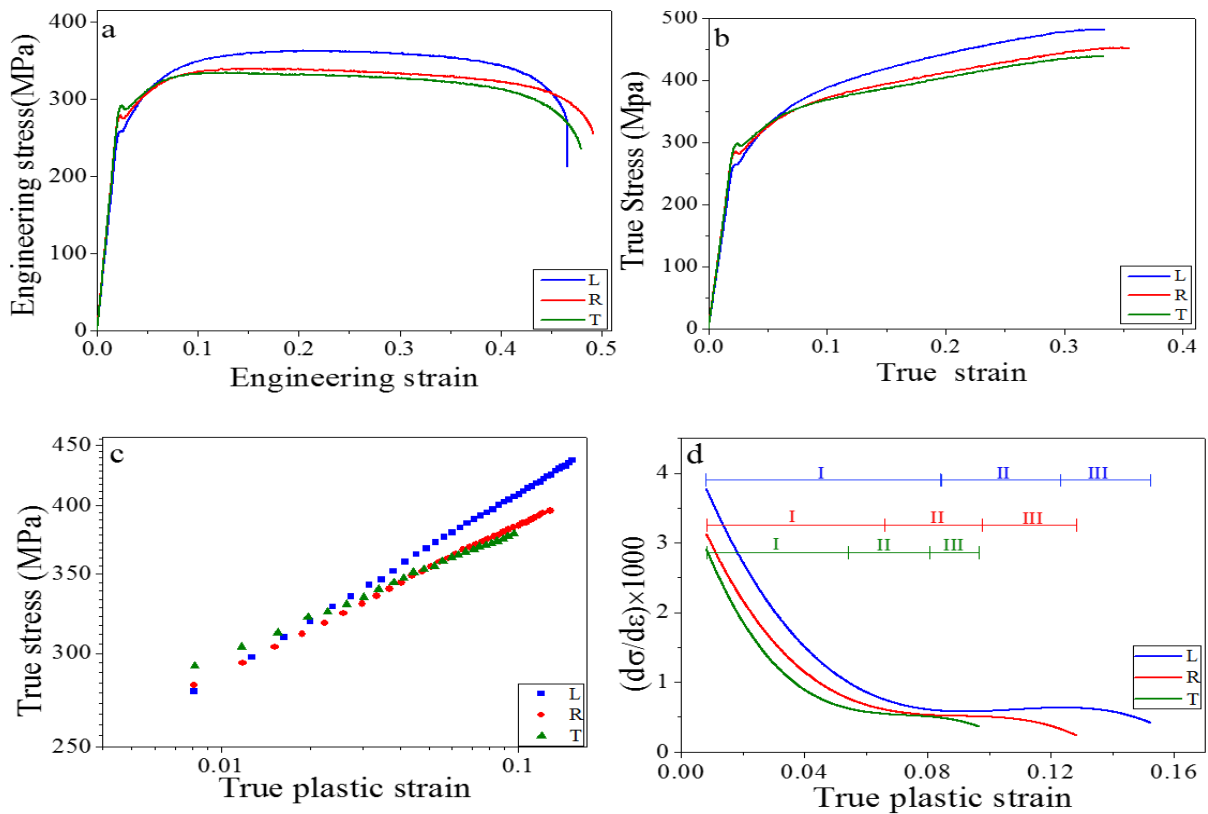


Fig. 4.6: Tensile properties of SRS sample at 348K along L, R and T directions: (a) Engineering stress – Engineering strain curves, (b) True stress – True strain curves (c) Log True stress – Log True plastic strain and (d) Differential curves

The tensile properties of LOS samples exhibit higher values when compared to those of SRS and TRS. The explanation of this lies in understanding the multiplication of dislocations during the deformation and the alloying effect of alloying elements (Pshenichnikov, Stuckert, and Walter 2015). At this point, it is important to note that the LOS has less Oxygen content than that of SRS and TRS. Even though comparatively the higher Oxygen content in SRS and TRS which will lock the dislocation due to segregation of Oxygen content into dislocation sites (Pshenichnikov, Stuckert, and Walter 2015) but this will also result in a decrease of multiplication of the dislocations and thereby causing the decline in the density of dislocations by modifying its substructure (Pshenichnikov, Stuckert, and Walter 2015). The higher strength parameters of LOS can therefore, attribute to the higher multiplication of dislocations than that

of the SRS and TRS (Pshenichnikov, Stuckert, and Walter 2015). The maximum and minimum values of  $\sigma_Y$  are observed in both LOS and SRS at 348K and 498K along T and L sample directions, respectively. The  $\sigma_Y$  follows a specific trend that it is maximum in T and minimum in L sample directions in all the three alloys irrespective of temperature variation. This observation is not so surprising because the  $\sigma_Y$  is very sensitive due to the presence of texture (Akhiani and Szpunar 2013). However, the  $\sigma_{UTS}$  and percentage elongation values do not show any specific trend with sample direction even though they decrease and increase with an increase in temperature, respectively. The observed ductile dimples of post tensile tested specimens of all the alloys support the total elongation (Tables 4.1-4.3, and Fig. 4.15 – 4.17). Because, elongation gives the idea of ductility.



*Fig. 4.7: Tensile properties of SRS sample at 423K along L, R and T directions: (a) Engineering stress – Engineering strain curves, (b) True stress – True strain curves (c) Log True stress – Log True plastic strain and (d) Differential curves*

The engineering stress – strain, true stress – true strain curves of all the three alloys show similar nature i.e., increasing stress with increasing strain until UTS thereafter subsequent softening till fracture. However, the plastic flow paths between  $\sigma_Y$  and  $\sigma_{UTS}$  are varying with sample direction. This can be ascribed to Peierls stress (lattice resistance) given by solute atoms (Fe, Cr, Sn and O) which are accountable to effect the complete stress - strain curve (Banumathy, Mandal, and Singh 2009b). It is well established that the lattice resistance is a shear stress which is dependent on crystallographic directions for dislocation motion (Banumathy, Mandal, and Singh 2009b). Hence, the directional dependent tensile flow curves can attribute to the moderate texture present in the material. Further, the results also reflect that the stress values are decreasing with increasing test temperature.

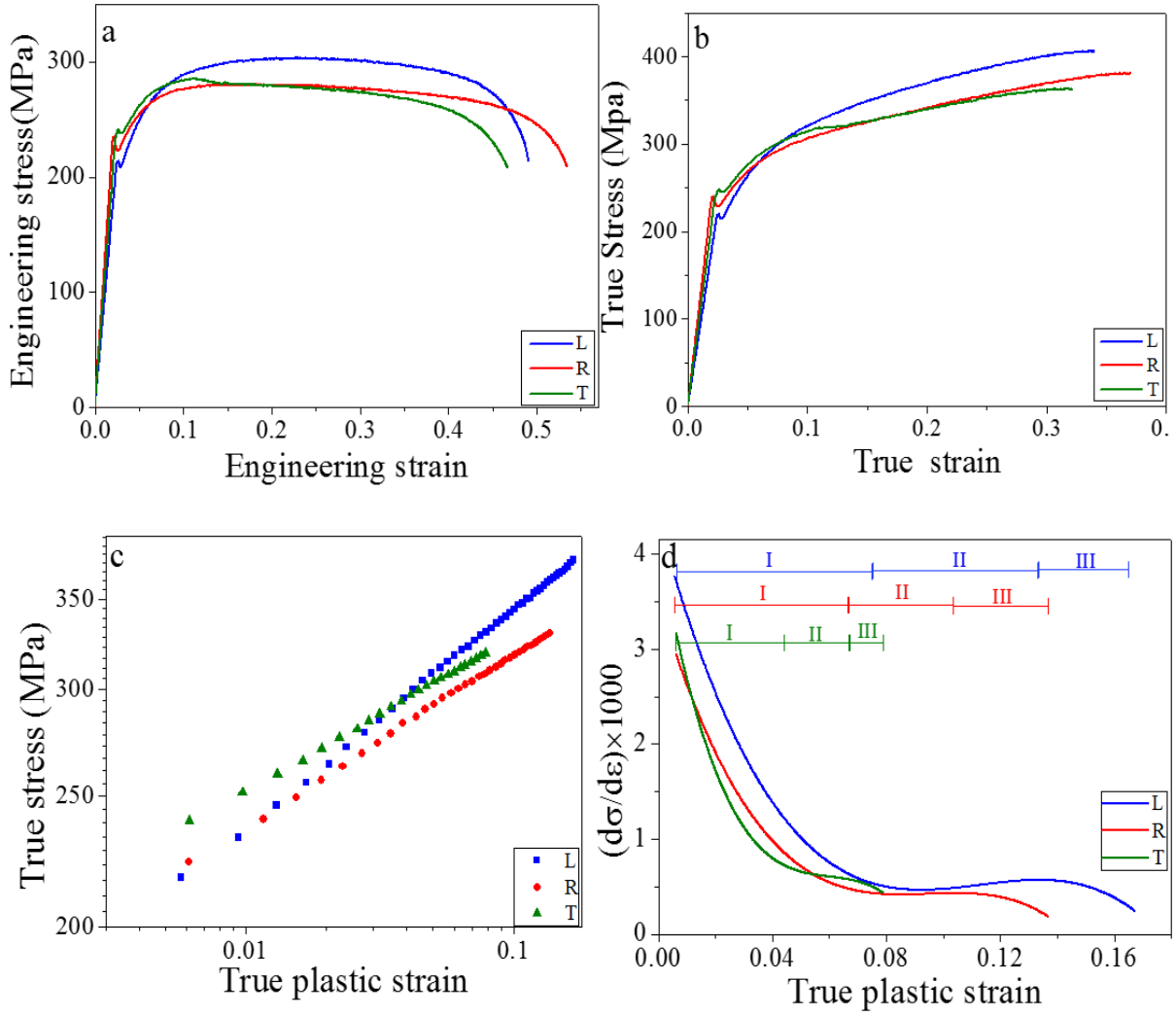


Fig. 4.8: Tensile properties of SRS sample at 498K along L, R and T directions: (a) Engineering stress – Engineering strain curves, (b) True stress – True strain curves (c) Log True stress – Log True plastic strain and (d) Differential curves

True stress – true plastic strain curves on a log scale of all the three materials depict straight line variation (Figs. 4.5 – 4.13). The single slope of the curves indicates that during the deformation, only deformation mechanism is under activation in the sample. To explain the behaviour, it has been fitted with the Hollomon equation, given as

$$\sigma = K\epsilon^n \quad (4.1)$$

Where,  $n$  and  $K$  are strain hardening and strength coefficients respectively.

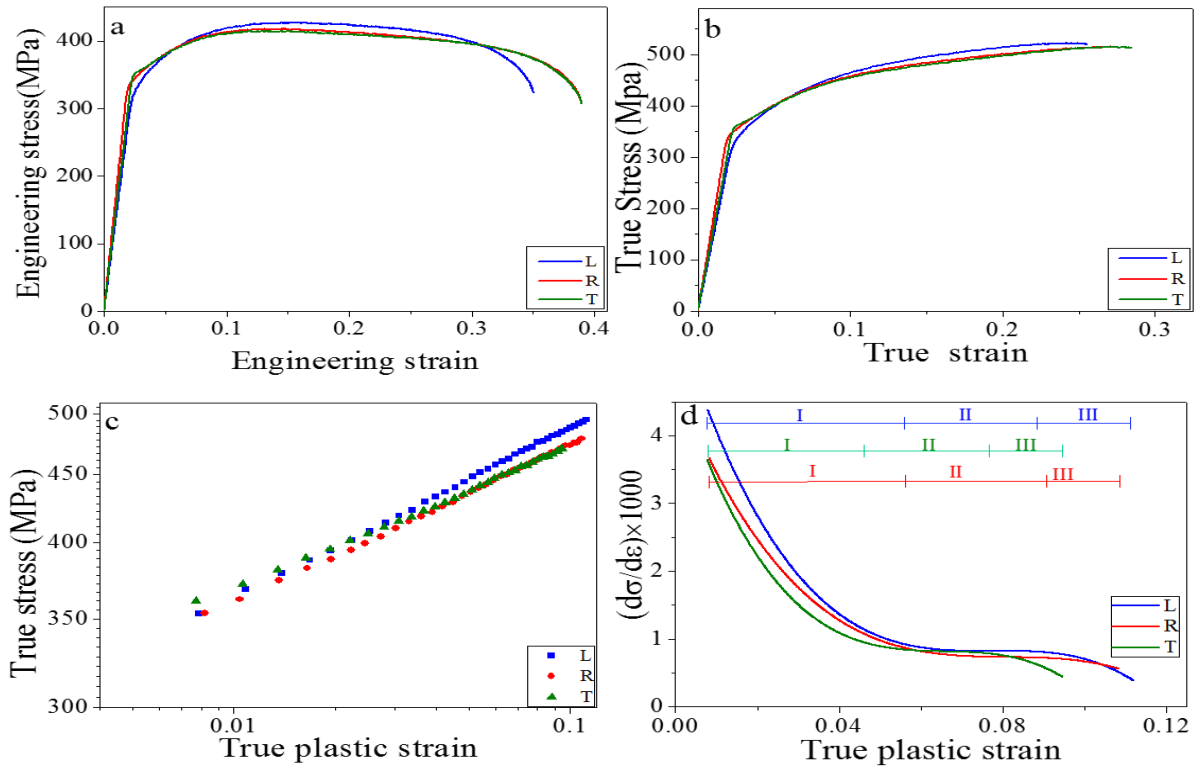
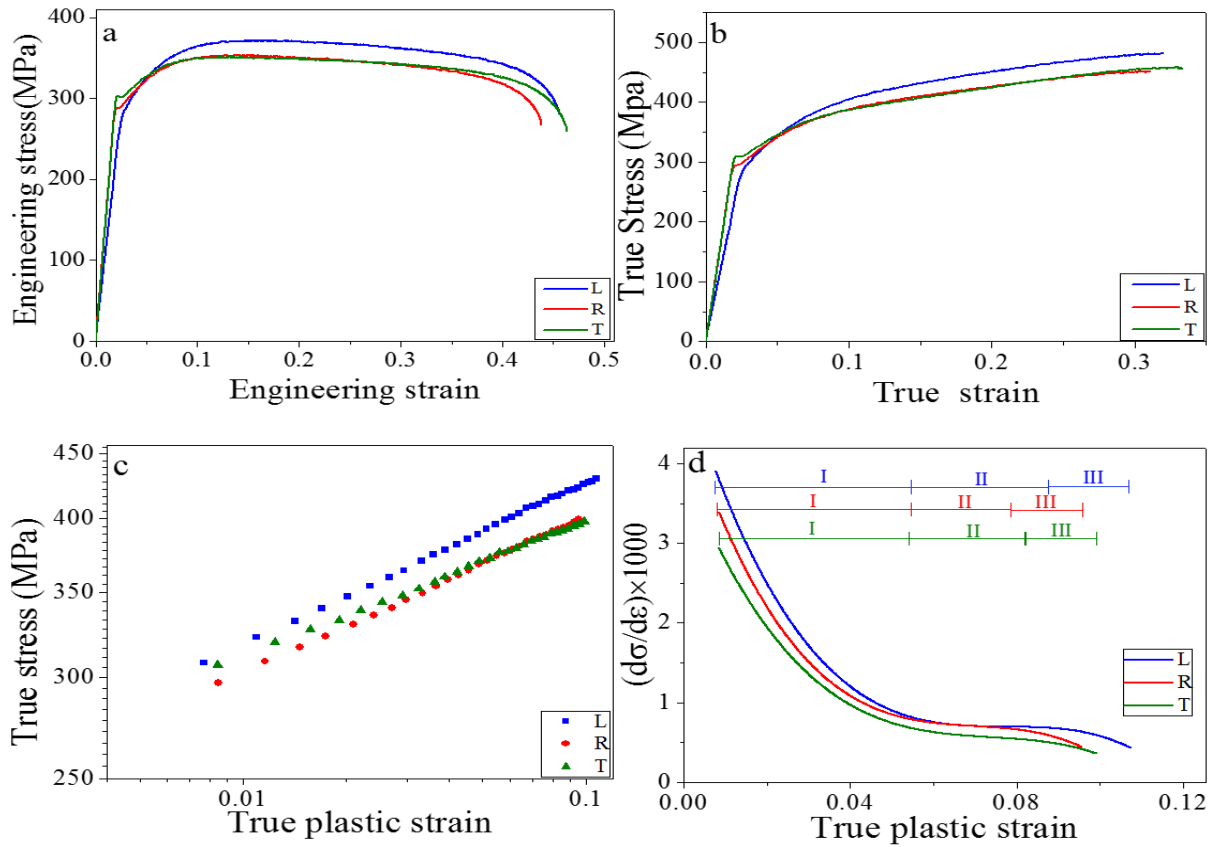


Fig. 4.9: Tensile properties of TRS sample at 348K along L, R and T directions: (a) Engineering stress – Engineering strain curves, (b) True stress – True strain curves (c) Log True stress – Log True plastic strain and (d) Differential curves

The  $K$  and  $n$  values are determined from the equation (4.1), and the coefficient of determination ( $R^2$ ) are listed in Tables 4.1-4.3. It is to be noted here that the  $R^2$  range is between 0.99039 and 0.99959. The  $R^2$  range is quite high and therefore it is an excellent fit of the data of the flow curves of all the alloys. The  $n$  value is maximum and minimum in SRS and TRS respectively. The  $K$  is maximum and minimum in LOS and TRS. For all the three alloys, irrespective of operating temperature maximum and minimum values of  $n$  are found in L and T directions respectively. In addition,  $n$  value also exhibited direct relation with ductility of the alloys i.e. higher the ductility of the alloy higher is the  $n$  value.



*Fig. 4.10: Tensile properties of TRS sample at 423K along L, R and T directions: (a) Engineering stress – Engineering strain curves, (b) True stress – True strain curves (c) Log True stress – Log True plastic strain and (d) Differential curves*

In general, the log true stress – log true plastic strain curves qualitatively demonstrate work hardening of the material. However, the instantaneous work hardening rate curves, which are obtained by numerically differentiating the true stress with respect to true plastic strain and plotted against true plastic strain, are a quantitative description of work hardening rate of materials. These curves have also been used to identify and solve the issues related to micro deformation mechanisms of the materials.

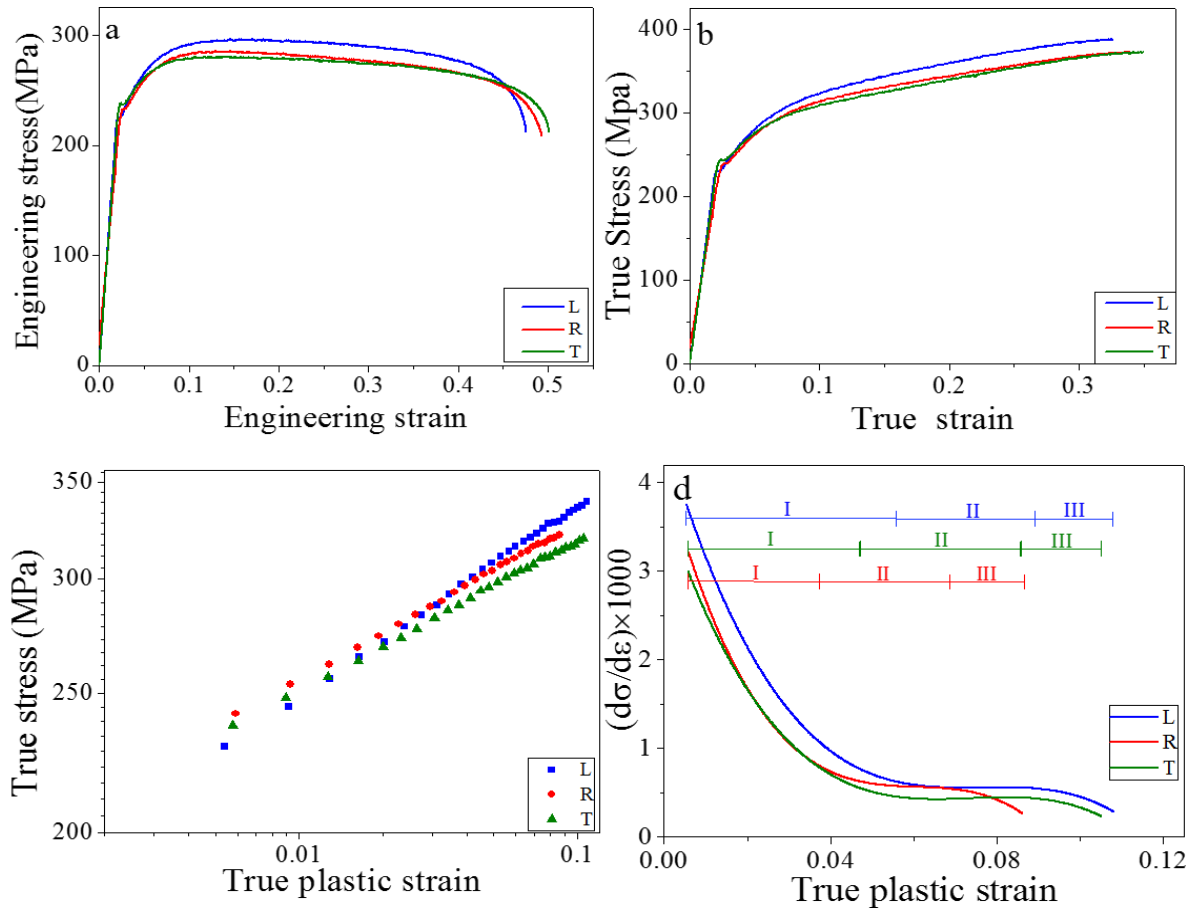


Fig. 4.11: Tensile properties of TRS sample at 498K along L, R and T directions: (a) Engineering stress – Engineering strain curves, (b) True stress – True strain curves (c) Log True stress – Log True plastic strain and (d) Differential curves.

Irrespective of direction, the nature of all the differential curves of all the alloys is similar (Figs. 4.5d – 4.13d). However, the curve paths are different for the sample direction in all the three experimental alloys. These curve paths are not overlapping with each other. Instead, they are in different sizes in different sample directions. The orientation dependant differential curves of the sample are due to the presence of moderate texture in the alloys. All the differential curves divided into three distinct regions, namely: Elasto-plastic transformation (I), Easy glide stage (II), Dynamic recovery (III). The stage I displays the change of elastic to plastic flow of the alloy during deformation. In this stage, there is a rapid decrease in the work hardening rate with increment in true plastic strain and true stress. The regime I is a consequence of changes in microstructural parameters such as crystal size, crystal shape,

inclusions, solute atoms, sub-grain structures, initial dislocation densities, macro and micro textures (Manda, Chakkingal, and Singh 2016). The regime I of the curves show that they are distinct from one another without overlapping. The distinct flow paths in regime I can be attributed to the various proportions of solute atoms in the original materials. The constant work hardening rate can be in the regime II (Figs. 4.5d – 4.13d). The length of the regime II is maximum in L direction and minimum in T direction. The local work hardening occurs as a result of planar slip movements in this region and therefore, it is called an easy glide stage.

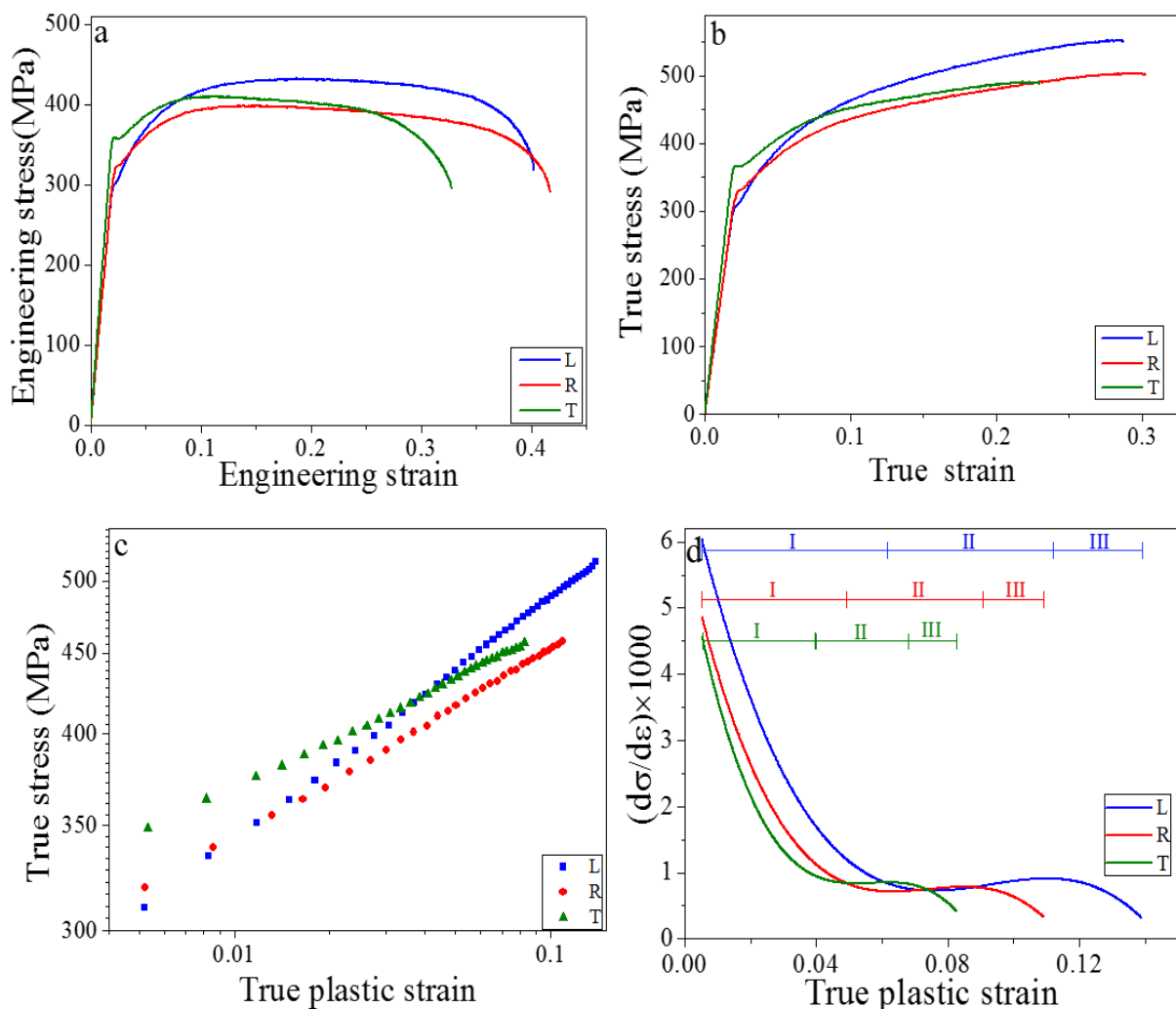


Fig. 4.12: Tensile properties of LOS sample at 348K along L, R and T directions: (a) Engineering stress – Engineering strain curves, (b) True stress – True strain curves (c) True stress – True plastic strain and (d) Differential curves.



The stage III of the differential curves is related to the stress at which dynamic recovery process begins with required pile-up of dislocations. Even though all the three samples show similar regime III in differential curves, the slope of the end part (linear) of the regime III varies.

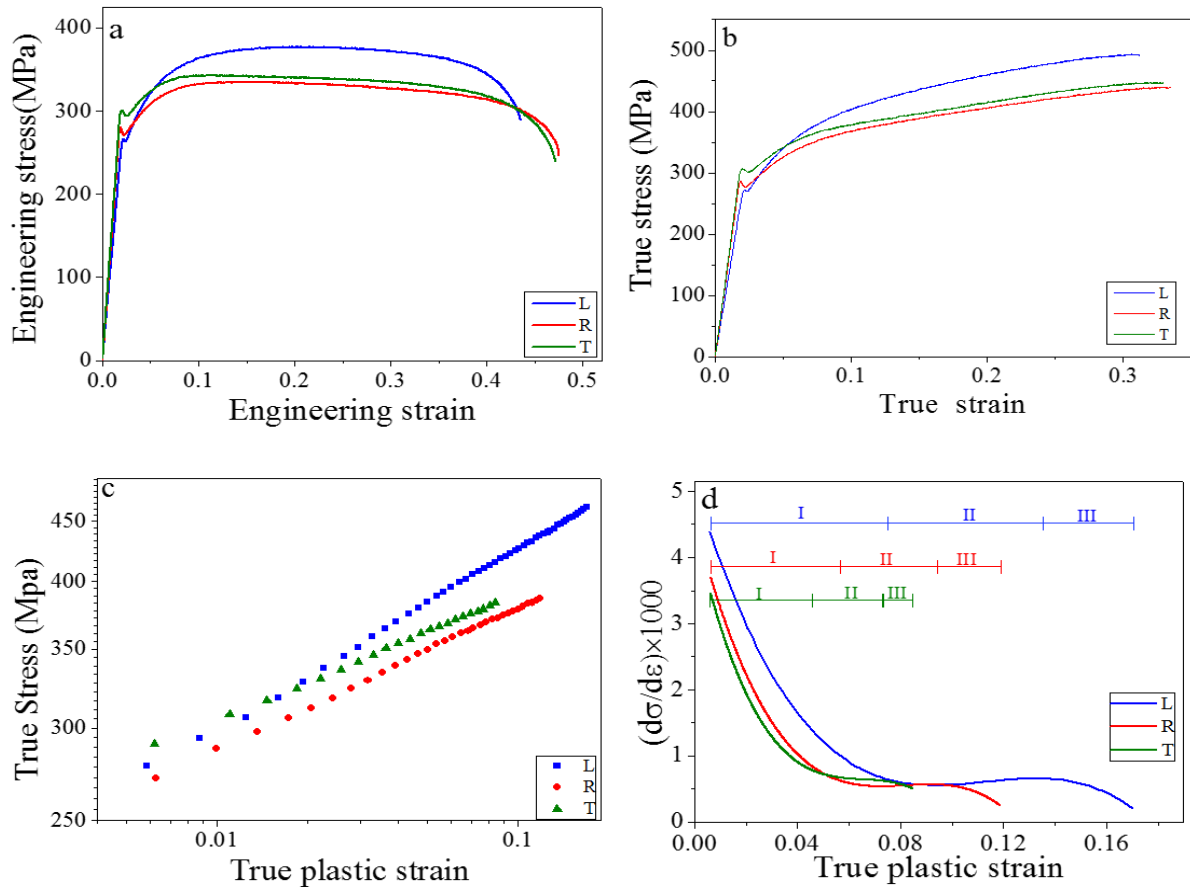


Fig. 4.13: Tensile properties of LOS sample at 423K along L, R and T directions: (a) Engineering stress – Engineering strain curves, (b) True stress – True strain curves (c) Log True stress – Log True plastic strain and (d) Differential curves

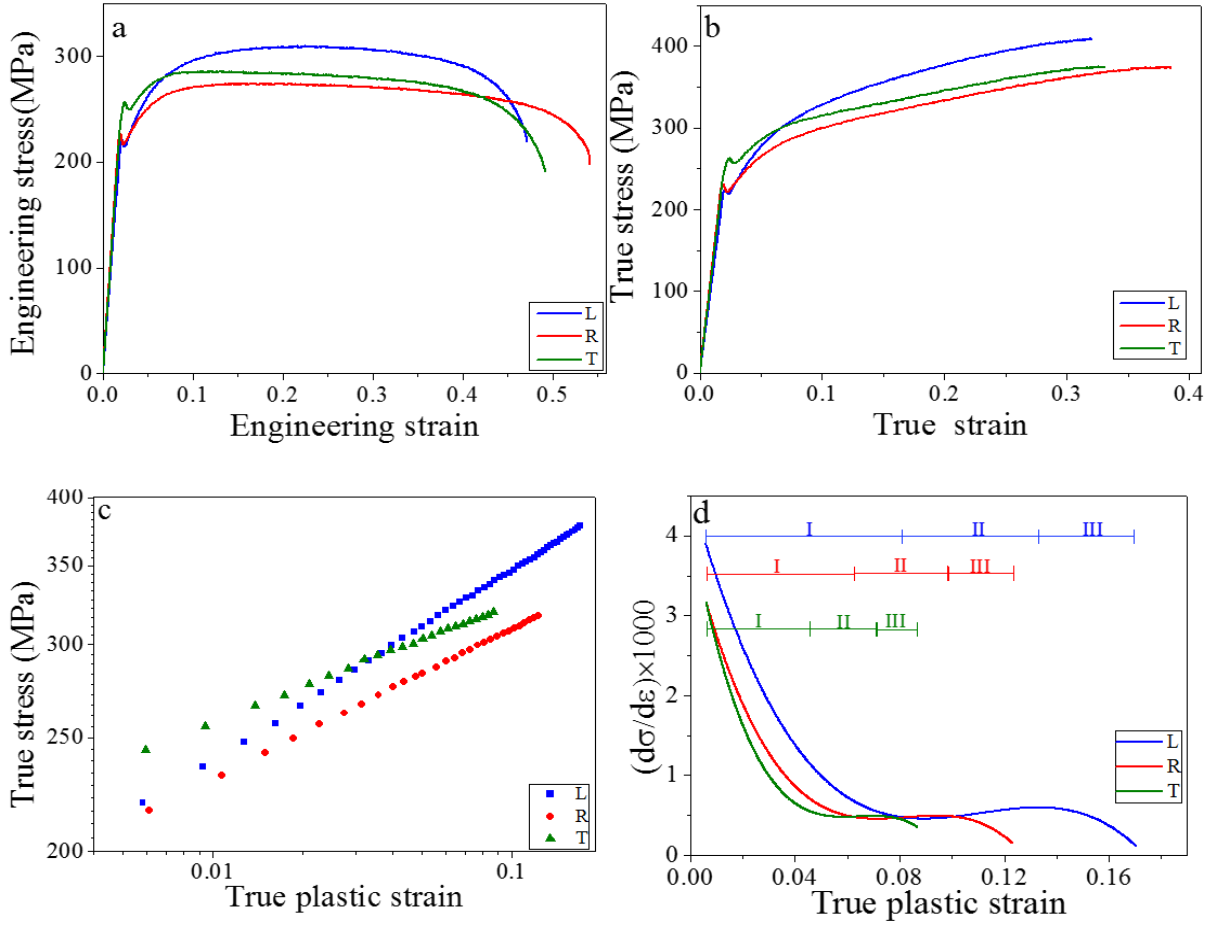


Fig. 4.14: Fig. 4.13: Tensile properties of LOS sample at 498K along L, R and T directions: (a) Engineering stress – Engineering strain curves, (b) True stress – True strain curves (c) Log True stress – Log True plastic strain and (d) Differential curves

### 4.3.3 Anisotropy of Zircaloy - 4 at room temperature and fractography

The “% of in-plane anisotropy ( $A_{IP}$ ) (Kelly and Smith 1973) and “anisotropy index ( $\delta$ ) (Manda, Chakkingal, and Singh 2016)” are two terms used to calculate the anisotropy of the present alloys. The anisotropy expressed in  $A_{IP}$  and  $\delta$  is associated with yield strength and elongation, respectively. The  $A_{IP}$ , depends on the  $\sigma_{YS}$  in different sample directions, is defined in equation (4.1) for the present alloys in which  $\sigma_{YS}$  value is more in T sample direction than that of the other directions.

$$A_{IP} = \frac{2 \times \sigma_{YS}(T) - \sigma_{YS}(L) - \sigma_{YS}(R)}{2 \times \sigma_{YS}(T)} \times 100 \quad (4.2)$$

The equation (4.2) illustrates that the  $A_{IP}$  value rises with an increase in the extent of anisotropy, and it is zero for isotropic materials. The calculated  $A_{IP}$  of all the three materials are listed in Table 4.1-4.3.

Wu and Koo (Manda, Chakkingal, and Singh 2016) proposed that the tensile anisotropy of material can also be expressed from the “anisotropy index” parameter, which is defined in equation (2) in terms of uniform percentage elongation.

$$\delta = \frac{|\% \epsilon_U(T) - \% \epsilon_U(L)|}{\% \epsilon_U(T) + \% \epsilon_U(L)} \times 100 \quad (2)$$

where  $\% \epsilon_U(T)$  and  $\% \epsilon_U(L)$  are the percentage uniform elongation of the tensile specimens along T and L directions respectively. The isotropic materials display  $\delta$  value as zero where  $\% \epsilon_U(T) = \% \epsilon_U(L)$ . However, it is in-between zero and 1(100%) for normal anisotropic materials and in the extreme case it is 1(100%) where  $\% \epsilon_U(T) \gg \% \epsilon_U(L)$  or  $\% \epsilon_U(L) \gg \% \epsilon_U(T)$ . The calculated anisotropy index ( $\delta$ ) values for the present alloys are listed in Tables 4.1-4.3.

Even though both the anisotropy parameters do not show any specific trend with the temperature and sample direction, they do exhibit moderate values in all the three materials (Tables 4.1-4.3). The  $A_{IP}$  and  $\delta$  are maximum in LOS samples at all the temperatures 75 °C, 150 °C and 498K when compared to the other alloys. Therefore, the presence of moderate values of the anisotropy parameters of all the three alloys can attribute to the presence of moderate-intensity texture in SRS, TRS and LOS materials.

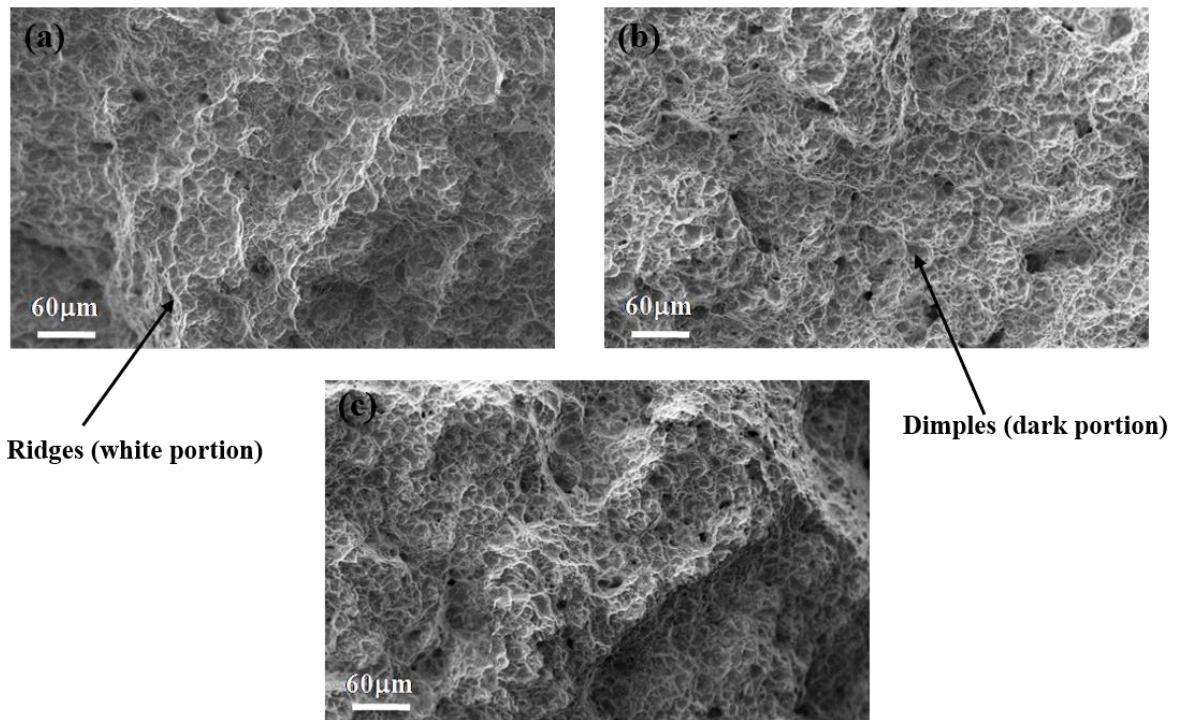


Fig. 4.15: The fracture surface of SRS tensile samples along longitudinal direction at: (a) 348K, (b) 423K and (c) 498K.

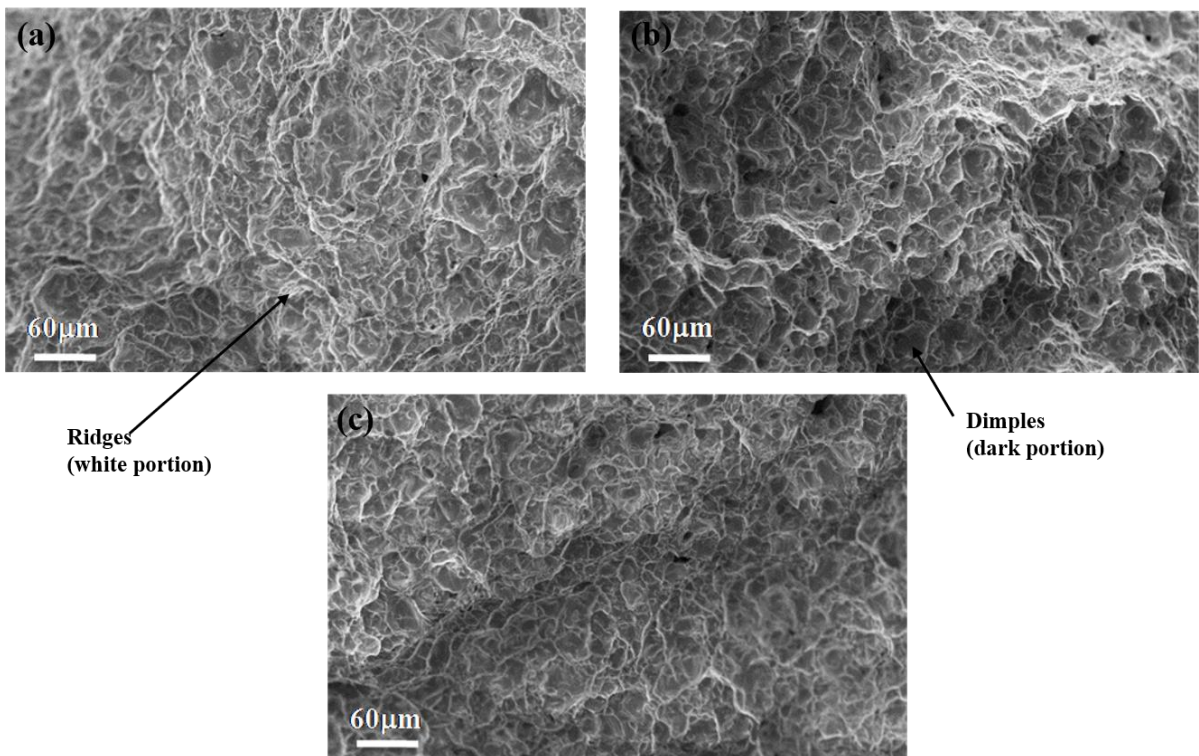
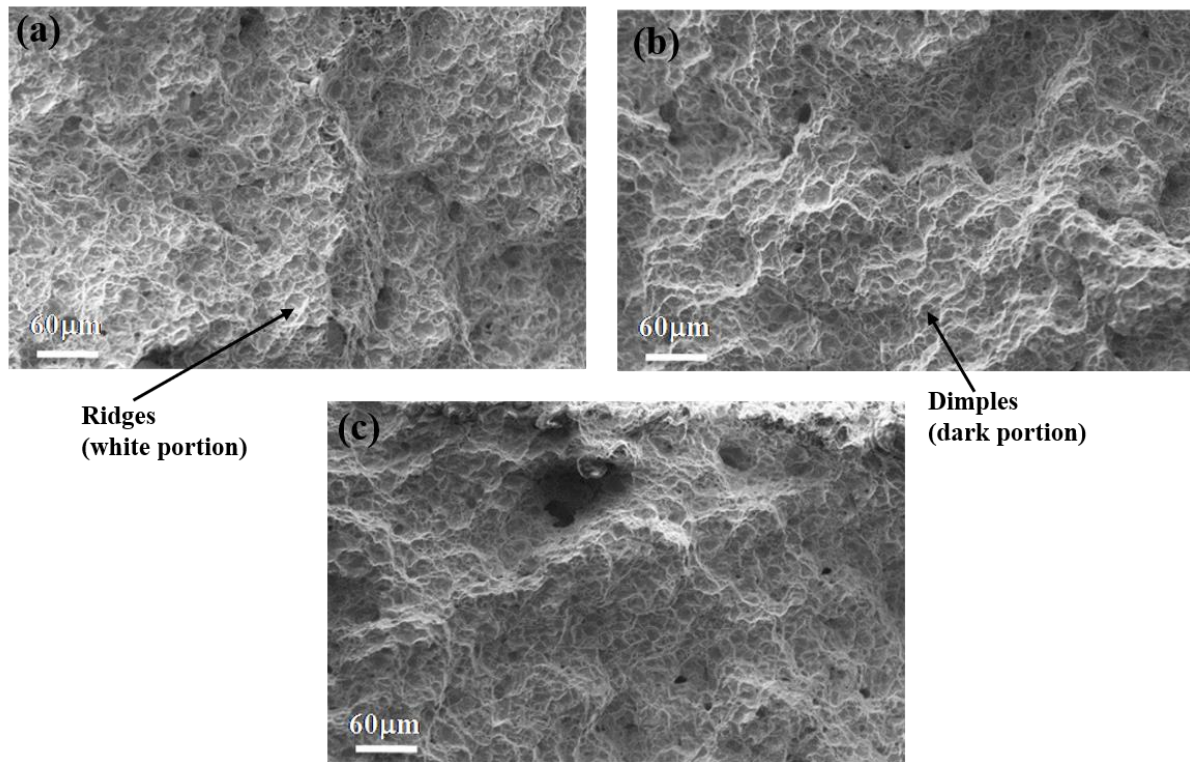


Fig. 4.16: The fracture surface of TRS tensile samples along longitudinal direction at: (a) 348K, (b) 423K and (c) 498K.



*Fig. 4.17: The fracture surface of LOS tensile samples along longitudinal direction at: (a) 348K, (b) 423K and (c) 498K.*

The SEM images (Fig. 4.15 – 4.17) of post tensile tested fracture surfaces show typical ductile fracture surfaces with equiaxed ductile dimples. The ductile dimples in all the three materials without any facets indicate the same mechanism of initial void nucleation, growth and coalescence (Qiu et al. 2001). The results reflect the depth of the ductile dimple, which indicate ductility of a material, that might vary from material to material irrespective of the variation in the temperature

#### **4.4 Summary**

Three different Zircaloy-4 sheet materials along three directions are subjected to tensile tests at elevated temperatures. The texture of the material was analysed by determining pole figures and ODF's. The following points are drawn.

- The correlation between sample direction, dependent tensile flow parameters and texture have been established in all the three alloys.

- All the three materials exhibit moderate texture, and the LOS material shows maximum texture intensity among the three. The basal pole figures do not display perfect c-type texture.
- In all the three alloys, irrespective of temperature variation, the yield strength ( $\sigma_Y$ ) follows a specific trend, that it is maximum and minimum along T and L sample directions respectively.
- The  $A_{IP}$  and  $\delta$  values are determined, and the calculated moderate values indicate the presence of moderate texture in all the three alloys at different temperatures.
- The true plastic stress and true plastic strain values are best fitted with the Holloman equation and the  $R^2$  ranges between 0.99039 and 0.99959.
- The derivative curves of all the three alloys exhibits the three typical work hardening regimes (i.e., Regime I, II and III).
- The three materials show ductile failure at high temperature.

However, now a days, in finite element codes, constitutive models are used for predicting the tensile behaviour of material at any intermediate temperature and strain rate. Therefore, using the tensile data form 3<sup>rd</sup> chapter and 4<sup>th</sup> chapter, constitutive models are calibrated for the Zircaloy-4 materials. The models are discussed in the next chapter.

# Chapter 5

## Constitutive models for Zircaloy-4

### 5.1 Introduction

Flow stress of material depends mainly on the temperature, strain rate and strain. Therefore, to know the flow stress behaviour of the material, at a specific strain rate and temperature tensile test need to be conducted. So, to study flow stress behaviour in a range of temperature and strain rates, it requires lot of tensile tests to be conducted. Now a days, people study stress behaviour predicting from finite element method where constitutive models are used. Because of the FE method it is easy to analyse the flow stress behaviour of material at any intermediate temperature and strain rate. The constitutive modes are two types, physical based and phenomenological. Recently, modified Johnson Cook model is calibrated for Zircaloy-4 material to simulate pilgering method by Deng et al. A macro constitutive model was calibrated for reactivity-initiated accident (RIA) loading conditions by Sauxet et al.

In the present work, phenomenological constitutive equations such as JC, m-Arr and physical based equation, m-ZA, are calibrated for three different types of Zircaloy-4 materials. The isothermal uniaxial tensile test data was used to determine the constant of the models and subsequently the predictability of these models for the three Zircaloy-4 materials are compared using statistical parameters such as coefficient of correlation (R) and average absolute error ( $\Delta$ ).

### 5.2 Experimental details

Tensile tests at different temperatures and strain rates are conducted. During the experiments the constant strain rates are obtained by varying the cross-head velocity in

exponential manner with the help of feedback control system. The cross-head velocity is as given in the Eq. 5.1.

$$v = \dot{\epsilon}L \exp(\dot{\epsilon}t) \quad (5.1)$$

where  $v, L$  and  $t$  are cross head velocity, gauge length of specimen and time respectively. The detailed discussion is given in chapter 3 and chapter 4.

### 5.3 Calibration of constitutive models

The constitutive models trace out the flow stress behaviour of materials. The constitutive models are input to the Finite Element (FE) codes. The simulation process mainly depends on the predictability of the constitutive model that is used in the code. In the present work, two phenomenological constitutive models namely JC and m-Arr and one physical based constitutive model namely ZA are calibrated. The JC model includes isotropic strain hardening, strain rate hardening and thermal softening effect on flow stress independently while the m-ZA considers the coupled effect of strain rate and temperature effect on flow stress behaviour of material. The m-Arr equation considers the coupled effect of strain rate and temperature in the form of Zener-Holloman parameter and also to include the strain effect on the flow stress an exponential function is included. A nonlinear regression was performed to predict constants included in the exponential function using the experimental data.

#### 5.3.1 Johnson Cook (JC) model

According to the original JC model (Gupta et al. 2013) the flow stress can be expressed as in the form of the Eq. 5.2.

$$\sigma = (A + B\epsilon^n)(1 + C \ln \dot{\epsilon}^*) (1 - T^{*m}) \quad (5.2)$$

Here the  $(A + B\epsilon^n)$ ,  $(1 + C \ln \dot{\epsilon}^*)$  and  $(1 - T^{*m})$  terms represents isothermal hardening, strain rate hardening and thermal softening respectively.  $\sigma$  stands for flow stress,  $\epsilon$  stands for true



plastic strain,  $A$  is the yield stress at reference temperature and strain rate,  $B$  is the coefficient of strain hardening,  $n$  is the strain hardening exponent,  $C$  is the coefficient of strain rate hardening,  $m$  stands for thermal softening exponent.  $\dot{\epsilon}^* = \dot{\epsilon}/\dot{\epsilon}_o$ , where  $\dot{\epsilon}$  is strain rate and  $\dot{\epsilon}_o$  is reference strain rate.  $T^*$  is homologous temperature as given in Eq. 5.3.

$$T^* = \frac{T_a - T_{ref}}{T_m - T_{ref}} \quad (5.3)$$

where  $T_a$  is absolute temperature,  $T_{ref}$  is reference temperature,  $T_m$  is melting temperature and always holds the  $T_a \geq T_{ref}$ . Generally, the  $T_{ref}$  is taken as the lowest temperature from the experimental values. Since the JC model accounts for the isolation from each of the phenomenon for isothermal hardening, strain rate hardening and thermal softening the expression can be written as the multiplication of the three terms.

**Case 1:** At reference temperature and reference strain rate

At reference temperature and reference strain rate both the thermal softening and strain rate hardening terms becomes equal to 1 and the Eq. 5.2 can be expressed as Eq. 5.4

$$\sigma = A + B\epsilon^n \quad (5.4)$$

The value of  $A$  is yield stress at reference temperature of 298K and reference strain rate of  $0.001s^{-1}$  for all the three Zircaloy-4 materials. Now, by plotting line between  $\ln(\sigma - A)$  and  $\ln(\epsilon)$  at reference strain rate and reference temperature the slope gives  $n$  value.  $B$  value can be calculated from intercept.

**Case 2:** At reference temperature and fixed strain

At reference temperature the isothermal softening term equals to 1 and the Eq. 1 reduces to Eq. 5.5

$$\sigma = (A + B\epsilon^n)(1 + C\ln\dot{\epsilon}^*) \quad (5.5)$$

Since it is fixed strain condition, for each value of strain, line is plotted between  $\frac{\sigma}{A+B\varepsilon^n} - 1$  and  $\ln \dot{\varepsilon}^*$ , from which the slope ‘C’ value is obtained. Here, for each value of  $\varepsilon$  the ‘C’ value is obtained.

**Case 3:** At reference strain rate and fixed strain

At reference strain rate, the strain rate hardening contribution in Eq. 5.2 becomes equal to 1, therefore, the Eq. 5.2 reduced to Eq. 5.6.

$$\sigma = (A + B\varepsilon^n)(1 - T^{*m}) \quad (5.6)$$

It is also fixed strain condition, therefore, for each value of  $\varepsilon$ , a line between  $\ln \left[ 1 - \frac{\sigma}{A+B\varepsilon^n} \right]$  and  $\ln (T^*)$  is plotted to get the slope ‘m’ value. Here again, for each value of  $\varepsilon$  there is a m value.

**Case 4:** Optimization of C and m values

Since there are a number of C and m values obtained, the optimized values can be determined by method of least squares. This approach works on constrained optimization by minimization of average absolute error ( $\Delta$ ) between experimental stress ( $\sigma_{exp}$ ) and predicted stress ( $\sigma_p$ ) as given in Eq. 5.7.

$$\Delta = \frac{1}{N} \sum_{i=1}^{i=N} \left| \frac{\sigma_{exp}^i - \sigma_p^i}{\sigma_{exp}^i} \right| \times 100 \quad (5.7)$$

where N is total number of data points,  $\sigma_{exp}$  is experimental stress,  $\sigma_p$  is predicted stress by using each couple of C and m values corresponding to their strain values. The prediction capacity of the constitutive equation can also be obtained by calculating the coefficient of correlation (R). The coefficient correlation is a statistical parameter obtained from the linear

relation between experimental stress values and predicted stress values. The mathematical expression of the  $R$  value is given in Eq. 5.8.

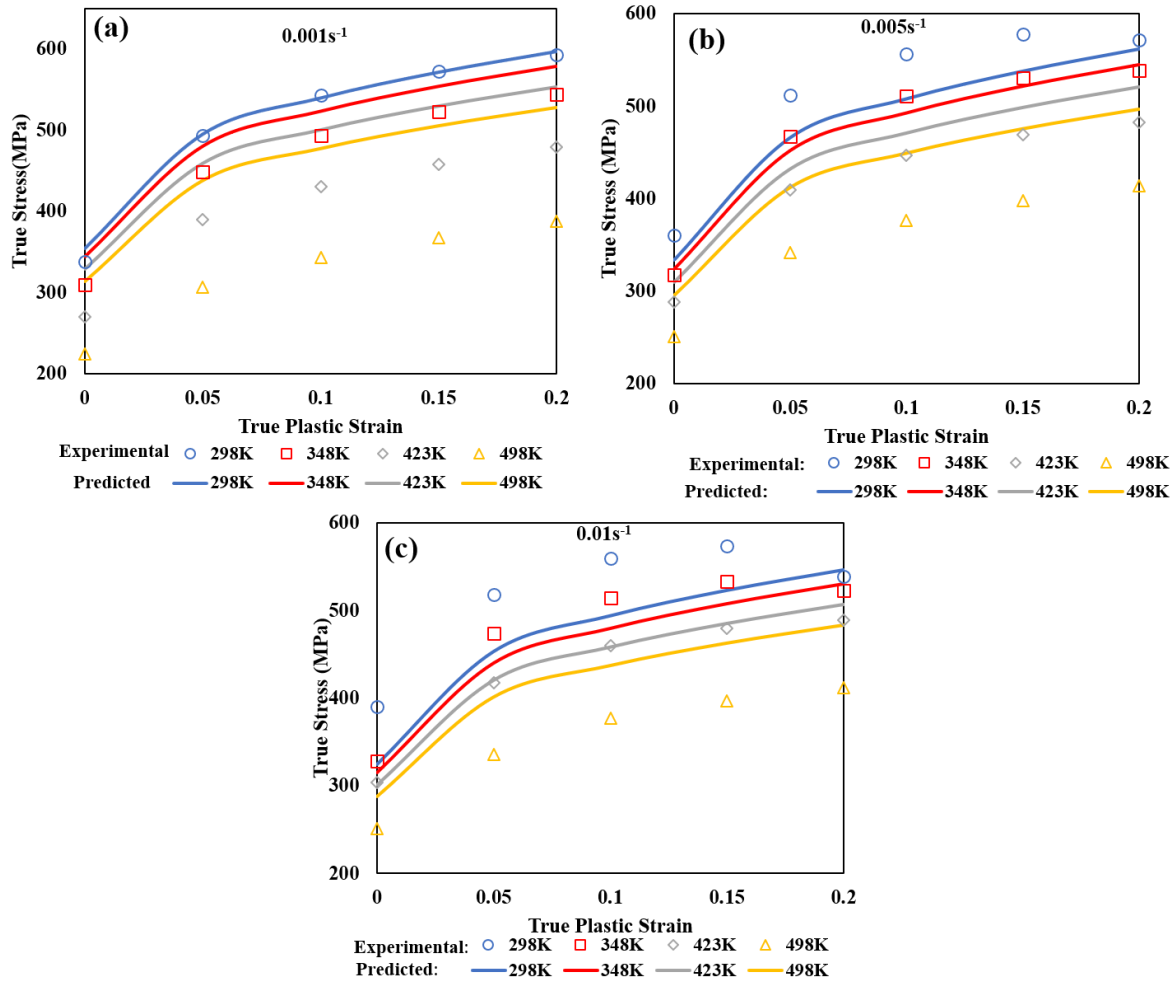


Fig. 5.1: True stress predicted from Johnson Cook model and experimental stress at various strains for different strain rates of (a)  $0.001s^{-1}$  (b)  $0.005s^{-1}$  (c)  $0.01s^{-1}$  for LOS material

$$R = \frac{\sum_{i=1}^{i=N} (\sigma_{exp}^i - \bar{\sigma}_{exp})(\sigma_p^i - \bar{\sigma}_p)}{\sqrt{\sum_{i=1}^{i=N} (\sigma_{exp}^i - \bar{\sigma}_{exp})^2 \sum_{i=1}^{i=N} (\sigma_p^i - \bar{\sigma}_p)^2}} \quad (5.8)$$

where  $\bar{\sigma}_{exp}$  and  $\bar{\sigma}_p$  are mean values of experimental and predicted stresses respectively. Since the  $R$  values have tendency to be biased, it is not necessary that the higher value of the  $R$  refer to better performance of the model in prediction. The  $\Delta$  gives an unbiased value due to the involvement of a term by term defining the error (Srinivasulu and Jain 2006). Hence, both  $R$  and  $\Delta$  and values

must be considered in analysis of predictability of the constitutive model. All the determined constants are listed in Table 5.1.

*Table 5.1: Constants for Johnson Cook (JC) constitutive equation*

Material	A (MPa)	B (MPa)	C	m	n
LOS	337.86	461.74	-0.0367	0.9794	0.3600
SRS	353.75	415.05	0.0131	0.6098	0.4025
TRS	375.26	468.72	-0.0100	0.8964	0.4519

Fig. 5.1 shows the comparison between the experimental values and predicted flow stress values from JC model. The JC model for the LOS material can be written as shown in Eq. 5.9.

$$\sigma = (337.86 + 461.74\varepsilon^{0.3600})(1 - 0.0367\ln\dot{\varepsilon}^*)(1 - T^{*0.9794}) \quad (5.9)$$

Similarly, the constants for the JC model for SRS and TRS materials are determined and listed in Table 5.1.

### 5.3.2 Modified Zerilli-Armstrong (m-ZA) model

According to original Zerilli-Armstrong model(Gupta et al. 2013) the flow stress is expressed in Eq. 5.10.

$$\sigma = A_0 + A_1\varepsilon^n \exp(T(A_2 \ln\dot{\varepsilon} - A_3)) \quad (5.10)$$

where  $\sigma$  is flow stress,  $A_0$  is the thermal component of yield stress,  $A_1, A_2, A_3$  and  $n$  are material constants,  $\varepsilon$  is true plastic strain,  $T$  is absolute temperature and  $\dot{\varepsilon}$  is true plastic strain rate.

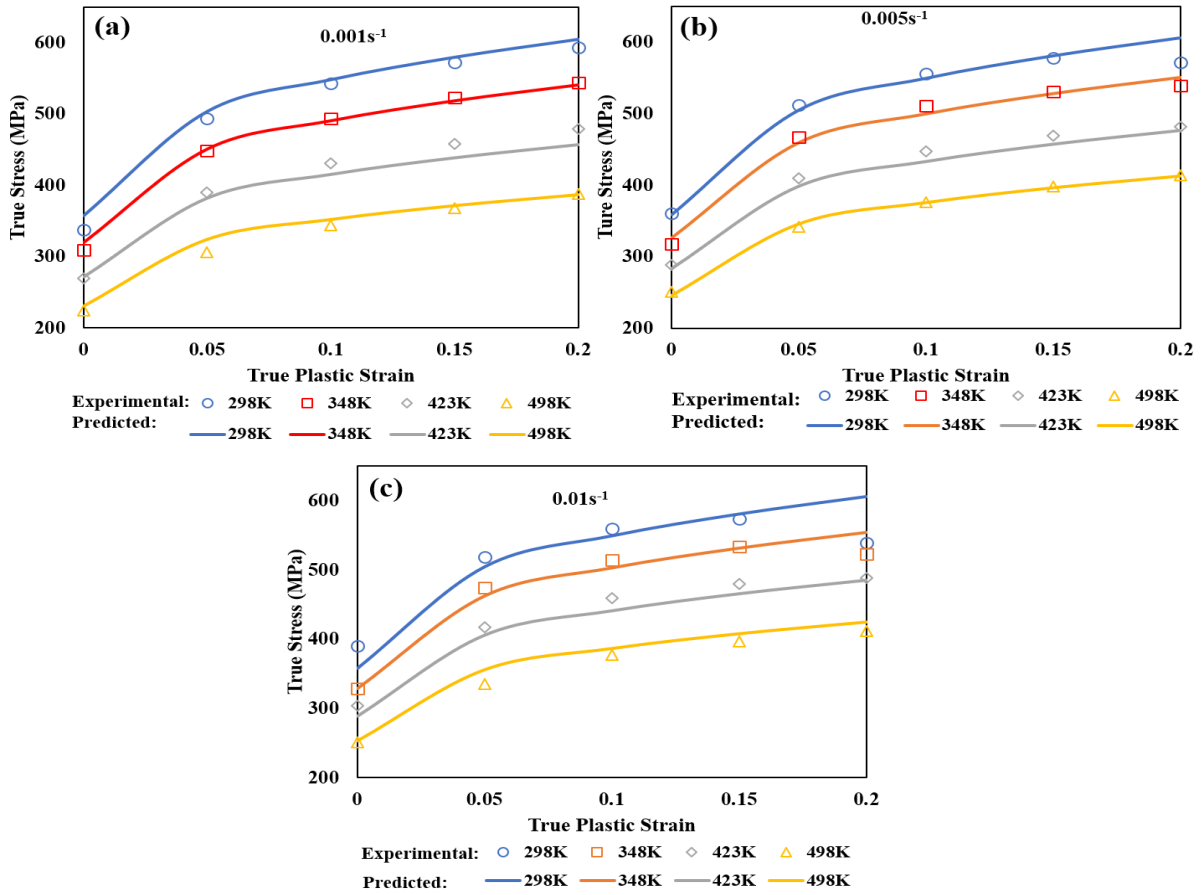


Fig. 5.2: True stress predicted from modified Zerilli-Armstrong and experimental stress at various strains for different strain rates of (a)  $0.001s^{-1}$  (b)  $0.005s^{-1}$  (c)  $0.01s^{-1}$  For LOS material.

The original Zerilli-Armstrong model has two components, thermal and athermal. The thermal component is  $A_1 \varepsilon^n \exp(T(A_2 \ln \dot{\varepsilon} - A_3))$  and the athermal component is  $A_0$ . The thermal component depends on experimental temperature while the athermal component depends on the grain size of the material during deformation. The thermal component can be inferred from the Fig. 2 where the flow stress decreases with increase in temperature. In the modified Zerilli-Armstrong (m-ZA) model the athermal component is neglected and the modified equation is expressed in Eq. 5.11.

$$\sigma = (C_1 + C_2 \varepsilon^n) e^{[-(C_3 + C_4 \varepsilon) T^* + (C_5 + C_6 T^*) \ln \dot{\varepsilon}^*]} \quad (5.11)$$

where  $\sigma$  stands for flow stress,  $C_1$  is taken as yield stress at reference temperature and reference strain rate (Similar to A value in the case of JC model),  $C_2, C_3, C_4, C_5, C_6$  and 'n' are material

constants,  $\varepsilon$  stands for true plastic strain,  $\dot{\varepsilon}^* = \dot{\varepsilon}/\dot{\varepsilon}_0$  is dimensionless strain rate with  $\dot{\varepsilon}$  as strain rate and  $\dot{\varepsilon}_0$  is reference strain rate,  $T^* = T_a - T_{ref}$  where T is instantaneous temperature,  $T_{ref}$  is reference temperature. The  $T_{ref}$  is the minimum temperature of the experiments conducted and is equals to 298K. The m-ZA model considers the strain hardening, strain rate hardening and thermal softening of the material. It also accounts for the coupled effects of temperature – strain hardening and temperature – strain rate hardening.

**Condition 1:** At reference strain rate

At reference strain rate,  $\dot{\varepsilon} = \dot{\varepsilon}_0 = 0.001s^{-1}$ , the  $\dot{\varepsilon}^* = 1$ . Therefore the Eq. 5.11 reduces to Eq. 5.12.

$$\sigma = (C_1 + C_2\varepsilon^n)e^{-(C_3+C_4\varepsilon)T^*} \quad (5.12)$$

By taking natural logarithm on both sides the Eq. 5.12 becomes to Eq. 5.13.

$$\ln(\sigma) = \ln(C_1 + C_2\varepsilon^n) - (C_3 + C_4\varepsilon)T^* \quad (5.13)$$

Using the corresponding experimental data (at reference strain rate of  $0.001s^{-1}$ , and for each strain value) the plot between  $\ln(\sigma)$  vs  $T^*$  gives intercept  $\ln(C_1 + C_2\varepsilon^n)$  and slope  $-(C_3 + C_4\varepsilon)$  for each strain value. Let us say, intercept is  $I_1$ , the intercept is expressed in Eq. 5.14.

$$I_1 = \ln(C_1 + C_2\varepsilon^n) \quad (5.14)$$

By taking exponential and natural logarithm on both sides, the Eq. 5.14 is changed to Eq. 5.15.

$$\ln(e^{I_1} - C_1) = \ln(C_2) + n \times \ln \varepsilon \quad (5.15)$$

$C_1$  is known from experimental data as the yield stress at reference strain rate and reference temperature. By plotting graph  $\ln(e^{I_1} - C_1)$  vs  $\ln \varepsilon$ , n is obtained as slope and the  $C_2$  can be calculated from the intercept.

Similarly, let us say  $S_1$  be the slope obtained from the Eq. 5.13  $S_1$  can be expressed as shown in Eq. 5.16

$$S_1 = -(C_3 + C_4\varepsilon) \quad (5.16)$$

By plotting the graph between  $S_1$  and  $\varepsilon$  at reference temperature and reference strain rate, the  $C_3$  and  $C_4$  values are calculated from intercept and slope respectively.

**Condition 2:** Consideration of coupled effects

By taking natural logarithm on both sides of Eq. 5.11, we get

$$\ln(\sigma) = \ln(C_1 + C_2\varepsilon^n) - (C_3 + C_4\varepsilon)T^* + (C_5 + C_6T^*)\ln\dot{\varepsilon}^* \quad (5.17)$$

By plotting graph  $\ln(\sigma)$  vs  $\ln\dot{\varepsilon}^*$  and say slope of the line is  $S_2$  then the slope can be written as in Eq. 5.18.

$$S_2 = (C_5 + C_6T^*) \quad (5.18)$$

For each temperature and strain one value of  $S_2$  is obtained. Therefore, by plotting the lines  $S_2$  vs  $T^*$ , the  $C_6$  and  $C_5$  are obtained as slope and intercept respectively. Since there are 5 sets of these values, the optimization is performed by minimizing the error using Eq 5.7 and Eq 5.8. All the values of  $C_1, C_2, C_3, C_4, C_5, C_6$  and  $n$  are shown in the Table 5.2.

*Table 5.2: Constants for modified Zerilli-Armstrong (m-ZA) model.*

	$C_1$ (MPa)	$C_2$ (MPa)	$C_3$	$C_4$	$C_5$	$C_6$	$n$
LOS	337.86	464.42	0.0022	0.0002	0.001	0.0002	0.3439
SRS	353.75	425.13	0.0023	-0.0016	0.0122	0.0001	0.3943
TRS	375.26	553.13	0.0024	-0.0004	0.0113	0.0003	0.5122

The comparison between experimental flow stress and predicted flow stress from the m-ZA model is depicted in the graphs shown in Fig. 5.2. The Modified Zerilli-Armstrong constitutive equation for the LOS material can be written as shown in Eq. 5.19.

$$\sigma = (337.86 + 464.42\varepsilon^{0.3439})e^{[-(0.0022+0.0002\varepsilon)T^*+(0.001+0.0002T^*)\ln\dot{\varepsilon}^*]} \quad (5.19)$$

Similarly, all the 7 constants of the model for the SRS and TRS materials are determined and listed in Table 5.2.

### 5.3.3 Modified-Arrhenius equation

Since the modified Arrhenius equation expresses the flow behaviour at elevated temperatures and strain rates, several researchers have been using it (Chen et al. 2019; L. Liu et al. 2019; Wei et al. 2020). The Zener-Holloman parameter is a function of temperature and strain rate and it is expressed in Eq. 5.20.

$$Z = \dot{\epsilon} \times \exp\left(\frac{Q}{RT}\right) \quad (5.20)$$

where  $Z$  is Zener-Holloman parameter,  $Q$  is activation energy ( $\text{KJ mol}^{-1}$ ),  $R$  is universal gas constant ( $8.314 \text{ Jmol}^{-1}\text{K}^{-1}$ ),  $T$  is absolute temperature in Kelvin and  $\dot{\epsilon}$  is true plastic strain rate and it is expressed in Eq. 5.21.

$$\dot{\epsilon} = A \times F(\sigma) \times \exp\left(\frac{-Q}{RT_a}\right) \quad (5.21)$$

where  $A$  is material constant, and  $F(\sigma)$  is expressed in Eq. 5.22.

$$F(\sigma) = \begin{cases} \sigma^n, & \alpha\sigma < 0.8 \\ \exp(\beta\sigma), & \alpha\sigma > 1.2 \\ [\sinh(\alpha\sigma)]^n, & \text{for all } \sigma \end{cases} \quad (5.22)$$

where  $\sigma$  is flow stress,  $n$ ,  $\beta$  are material constants  $\alpha = \beta/n$  and Therefore, by substituting the hyperbolic function  $F(\sigma) = [\sinh(\alpha\sigma)]^n$  in Eq. 5.21, we get upgraded equation in a hyperbolic sinusoidal form and it is expressed as in Eq. 5.23

$$\dot{\epsilon} = A \times [\sinh(\alpha\sigma)]^n \times \exp\left(\frac{-Q}{RT}\right) \quad (5.23)$$

Subsequently, by combining Eq. 5.23 and Eq. 5.20, the flow stress is expressed in Eq. 5.24.

$$\sigma = \frac{1}{\alpha} \ln \left\{ \left(\frac{Z}{A}\right)^{1/n} + \left[\left(\frac{Z}{A}\right)^{2/n} + 1\right]^{1/2} \right\} \quad (5.24)$$



In the above Eq. 5.24 the stress is expressed in terms of strain rate and temperature but the true plastic strain is not included. This Eq. 5.24 is called Arrhenius equation. In order to account for the true plastic strain in Eq. 5.24, an exponential function has been suggested and the modified Arrhenius equation is expressed in Eq. 5.25

$$\sigma = \frac{\beta_0 \varepsilon^{\beta_1} \exp(-\beta_2 \varepsilon)}{\alpha} \ln \left\{ \left( \frac{Z}{A} \right)^{1/n} + \left[ \left( \frac{Z}{A} \right)^{2/n} + 1 \right]^{1/2} \right\} \quad (5.25)$$

where  $\varepsilon$  referred as true plastic strain and  $\beta_0, \beta_1, \beta_2$  are material constants. In five different conditions all the materials constants are determined as given below.

**Condition 1:** Low stress levels i.e. at  $\alpha\sigma < 0.8$

From Eq. 5.21 and Eq. 5.22, at low stress condition, the strain rate can be expressed as in Eq. 5.26

$$\dot{\varepsilon} = A_1 \times \sigma^{n_1} \quad (5.26)$$

By plotting graph  $\ln(\dot{\varepsilon})$  vs  $\ln(\sigma)$ ,  $n_1$  is obtained as slope of the line equation.

**Condition 2:** High stress levels i.e. at  $\alpha\sigma > 1.2$

At high stress levels the strain rate can be expressed from Eq. 5.21 and Eq. 5.22 as in Eq. 5.27.

$$\dot{\varepsilon} = A_2 \times \exp(\beta\sigma) \quad (5.27)$$

$\beta$  is determined as the slope of the graph plotted between  $\ln(\dot{\varepsilon})$  and higher stress.

Since  $\beta$  and  $n_1$  are determined, the  $\alpha$  can be calculated from the Eq. 5.28.

$$\alpha = \beta/n_1 \quad (5.28)$$

**Condition 3:** At all stresses

Since  $\alpha$  is now known value, one can proceed to the case of all stress levels. By taking logarithm on both sides of Eq. 5.23, the Eq. 5.29 is obtained.

$$\ln [\sinh (\alpha \sigma)] = \frac{1}{n} \ln (\dot{\epsilon}) + \frac{Q}{nRT} - \frac{1}{n} \ln (A) \quad (5.29)$$

By plotting graph between  $\ln [\sinh (\alpha \sigma)]$  and  $\ln (\dot{\epsilon})$ ,  $1/n$  is calculated as slope from which  $n$  value is obtained. Similarly, by plotting the graph between  $\ln [\sinh (\alpha \sigma)]$  and  $1/T_a$ ,  $Q/(nR)$  yields as slope of the line. The average values of the  $Q/(nR)$  is used to calculate  $Q$  which is activation energy of the deformation process.

**Condition 4:** Finding  $Z$  and  $A$  values

Since  $Q$  values are now known, the  $Z$  values can be calculated from Eq. 5.20 in which the strain rate and temperature are experimentally fixed values.

By combining the Eq 5.20, Eq 5.21, and taking logarithm on both sides it can be expressed as in Eq. 5.30.

$$\ln (Z) = \ln (A) + n \times \ln [\sinh (\alpha \sigma)] \quad (5.30)$$

By plotting graph between  $\ln (Z)$  and  $\ln [\sinh (\alpha \sigma)]$  at a particular strain, the  $A$  value can be calculated from the intercept of  $\ln (A)$ .

*Table 5.3: Constants for modified Arrhenius constitutive equation*

Material	$n_1$	$\beta$	$\alpha$	$n$	$Q(\text{kJ/mol})$	$A$
LOS	22.6930	0.0386	0.0017	46.9247	129707.63	7.6086e19
SRS	23.4595	0.0179	0.0008	54.3239	130937.30	9.1357e40
TRS	17.7602	0.0312	0.0017	12.7781	36647.55	3490.639

**Condition 5:** Non-linear regression

Now, the material constants  $\alpha$ ,  $Q$ ,  $n$  and  $A$  values are known (listed in Table 5.3) and by substituting them in Eq. 5.25 the unknown material constants  $\beta_0$ ,  $\beta_1$ ,  $\beta_2$  can be found by regression. These values are obtained for each set of temperature and strain rate by nonlinear regression. It is performed using solver perimeter function in excel sheet and the values are listed in Tables 5.4-5.6.

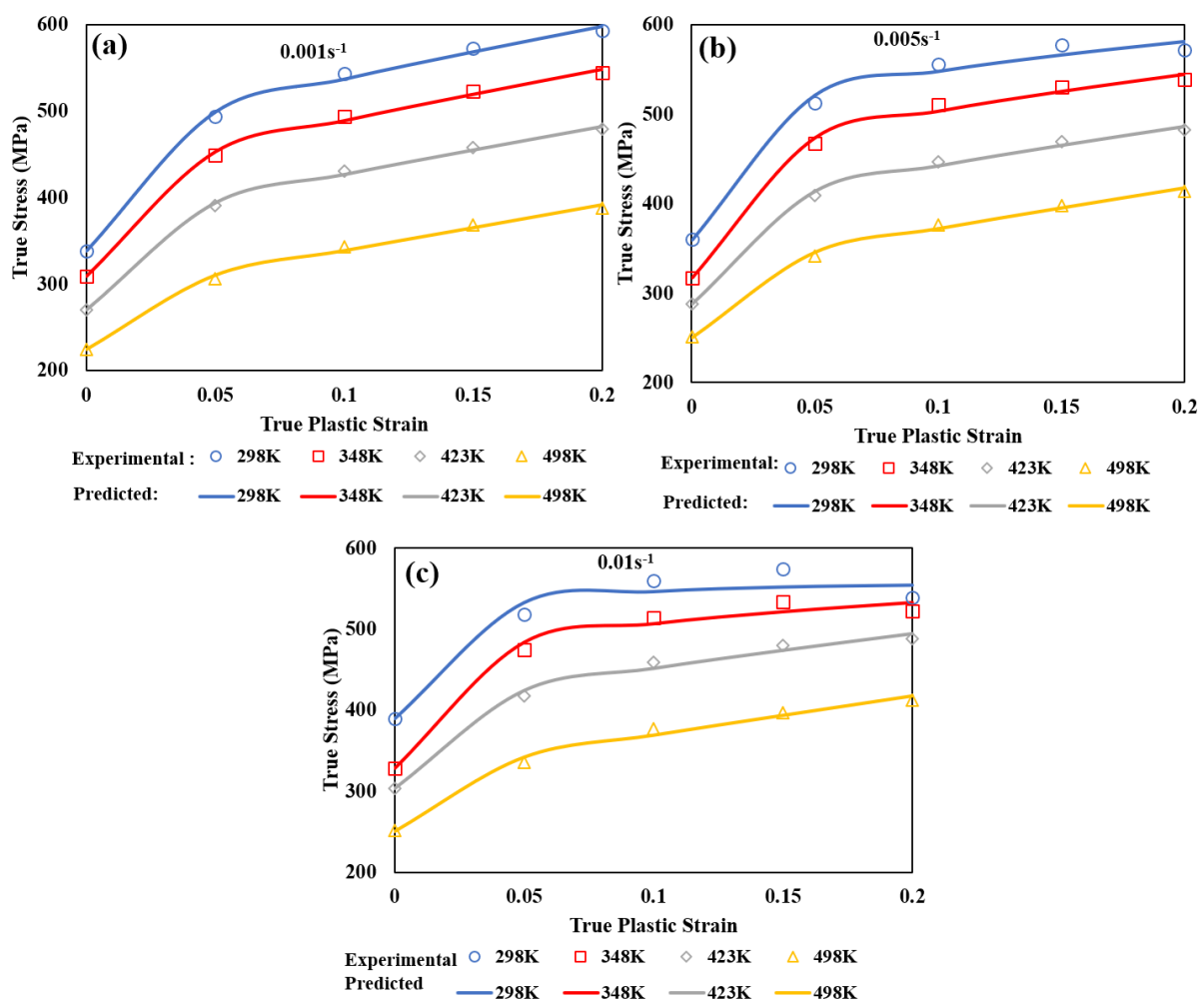


Fig. 5.3: True stress predicted from modified-Arrhenius and experimental stress at various strains for different strain rates of (a)  $0.001s^{-1}$  (b)  $0.005s^{-1}$  (c)  $0.01s^{-1}$  for LOS material

Table 5.4:  $\beta_0$  Values for LOS/SRS/TRS

Temp (K)	0.001s <sup>-1</sup>			0.005 s <sup>-1</sup>			0.01 s <sup>-1</sup>		
	LOS	SRS	TRS	LOS	SRS	TRS	LOS	SRS	TRS
298K	1.111	1.0381	1.098	1.162	1.150	1.132	1.177	1.232	1.178
348K	1.139	1.090	1.158	1.205	1.204	1.185	1.233	1.193	1.138
423K	1.137	1.111	1.190	1.175	1.061	1.049	1.175	1.210	1.156
498K	0.947	0.922	0.997	1.047	1.019	1.014	1.009	1.102	1.058

Table 5.5:  $\beta_1$  Values for LOS/SRS/TRS

Temp (K)	0.001s <sup>-1</sup>			0.005 s <sup>-1</sup>			0.01 s <sup>-1</sup>		
	LOS	SRS	TRS	LOS	SRS	TRS	LOS	SRS	TRS
298K	0.057	0.039	0.039	0.058	0.039	0.039	0.052	0.048	0.048
348K	0.055	0.041	0.041	0.061	0.051	0.051	0.061	0.047	0.047
423K	0.053	0.047	0.047	0.053	0.030	0.030	0.049	0.046	0.046
498K	0.042	0.038	0.038	0.044	0.036	0.036	0.042	0.042	0.042

Table 5.6:  $\beta_2$  Values for LOS/SRS/TRS

Temp (K)	0.001s <sup>-1</sup>			0.005 s <sup>-1</sup>			0.01 s <sup>-1</sup>		
	LOS	SRS	TRS	LOS	SRS	TRS	LOS	SRS	TRS
298K	-0.682	-0.853	-0.853	-0.187	0.098	0.098	0.217	0.980	0.980
348K	-0.763	-0.649	-0.649	-0.360	-0.147	-0.147	-0.076	-0.003	-0.003
423K	-0.852	-0.686	-0.686	-0.578	-0.778	-0.778	-0.566	-0.180	-0.180
498K	-1.160	-0.903	-0.903	-0.840	-0.686	-0.686	-0.937	-0.458	-0.458

The comparison between experimental and predicted flow stress from Modified Arrhenius constitutive equation for LOS material is shown in Fig. 5.3. The m-Arr equation for the LOS material can be written as shown in Eq. 5.31.

$$\sigma = \frac{\beta_0 \varepsilon^{\beta_1} \exp(-\beta_2 \varepsilon)}{0.0017} \ln \left\{ \left( \frac{Z}{7.6086e19} \right)^{1/46.9247} + \left[ \left( \frac{Z}{7.6086e19} \right)^{2/46.9247} + 1 \right]^{1/2} \right\} \quad (5.31)$$

where,  $\beta_0$ ,  $\beta_1$ ,  $\beta_2$  vary with respect to strain rate and temperature, and they are listed in Tables 5.4 – 5.6.

$$Z = \dot{\varepsilon} \times \exp \left( \frac{129707.63}{8.314 \times T} \right) \quad (5.32)$$

Similarly, the constants of m-Arr model for SRS and TRS materials are determined and listed in Tables 5.4 -5.6.

### 5.3.4 Khan-Huang-Liang (KHL) Constitutive modelling

Experimental flow stress behaviour at different temperatures of 298K, 348K, 423K and 498K and at three different strain rates of  $0.001s^{-1}$ ,  $0.005s^{-1}$  and  $0.01s^{-1}$  were already discussed in previous chapters (chapter 3 and chapter 4). Experimental data is used for finding the constants of the KHL model. The flow stress is expressed in Eq 5.33 according to the KHL model.

$$\sigma = \left[ A + B \left( 1 - \frac{\ln \dot{\varepsilon}^*}{\ln D} \right)^{n_1} \varepsilon^{n_0} \right] e^{C \ln(\dot{\varepsilon}^*)} (1 - T^{*m}) \quad (5.33)$$

where  $\sigma$  is true stress,  $\varepsilon$  is referred as true plastic strain, A is true stress at reference temperature and reference strain rate. In the present work the reference temperature and reference strain rates considered as 298K and  $0.001s^{-1}$ . B, C,  $n_0$ ,  $n_1$  and m are material constants.  $D = 10^6 s^{-1}$ . This is arbitrarily chosen upper bound strain rate. The  $\dot{\varepsilon}^*$  is a dimension less strain factor and it is equal to  $\dot{\varepsilon}/\dot{\varepsilon}_0$  where  $\dot{\varepsilon}$  is strain rate,  $\dot{\varepsilon}_0$  is reference strain rate. The  $T^*$  is homologous temperature and is given in Eq 5.34.

$$T^* = \frac{T_a - T_{ref}}{T_m - T_{ref}} \quad (5.34)$$

where  $T_a$  is absolute temperature,  $T_{ref}$  is reference temperature and  $T_m$  is melting temperature. The melting temperature of Zircaloy - 4 is 2123K. The material constants can be determined in different cases.

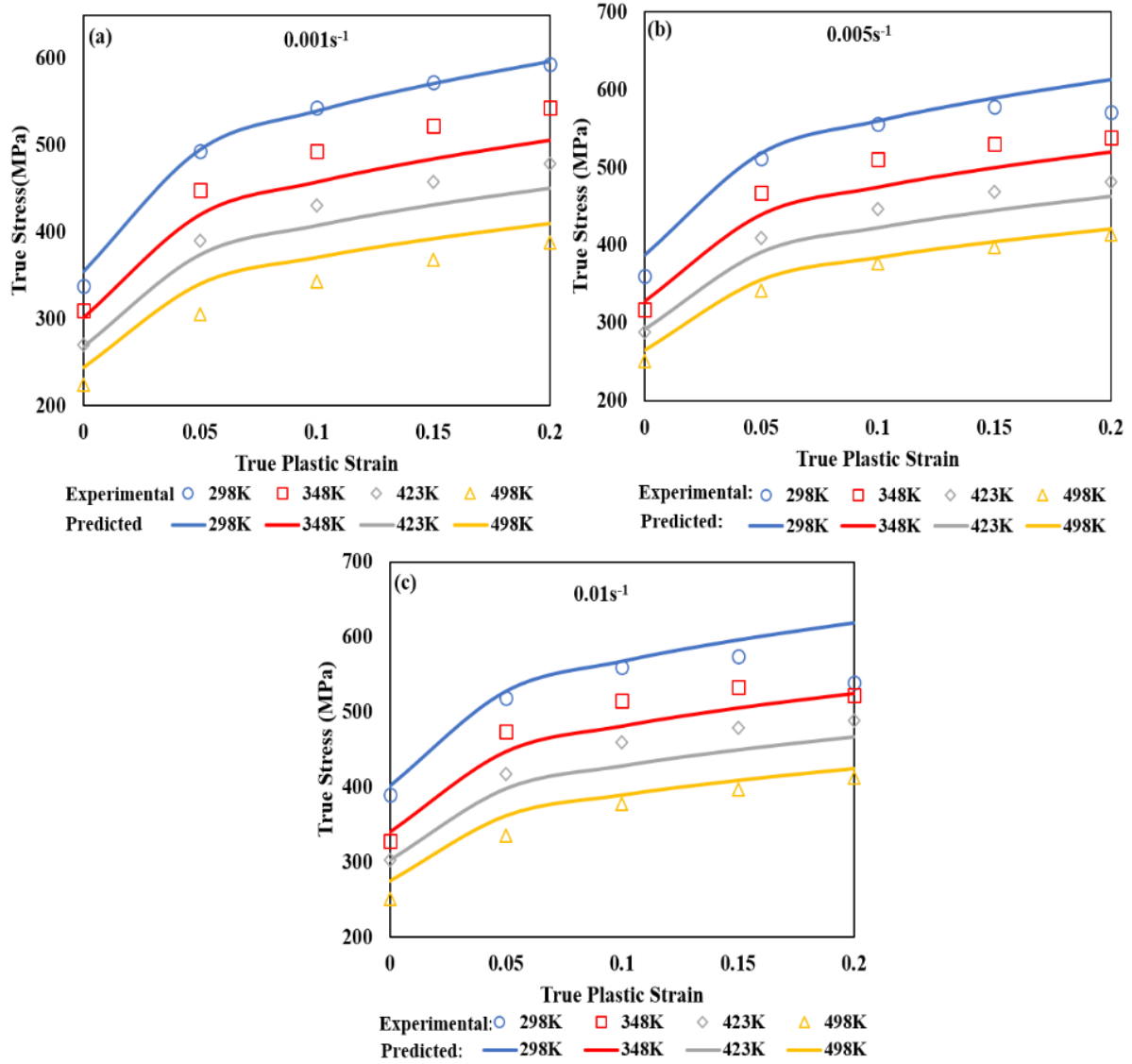


Fig. 5.4: The true stress estimated using KHL model and experimental true stress at various strains and strain rates of (a)  $0.001s^{-1}$ , (b)  $0.005s^{-1}$ , and (c)  $0.01s^{-1}$  for LOS material.

**Case I:** At reference temperature and reference strain rate

At reference temperature (298K) and reference strain rate ( $0.001s^{-1}$ ) the homologous temperature becomes zero and the  $\frac{\dot{\epsilon}}{\dot{\epsilon}_0} = 1$ . Therefore, the Eq 5.33 reduces to Eq 5.35.

$$\sigma = A + B\epsilon^{n_0} \quad (5.35)$$

$$\ln(\sigma - A) = \ln(B) + n_0 \ln(\epsilon) \quad (5.36)$$

'A' is the yield stress taken from the stress strain curve plotted at reference temperature and reference strain rate. By plotting the graph between  $\ln(\sigma - A)$  and  $\ln(\dot{\epsilon})$ , the slope of the line gives  $n_0$  value and B is calculated from intercept. The B and  $n_0$  values calculated for all the three LOS, SRS and TRS materials are tabulated in Table 5.7.

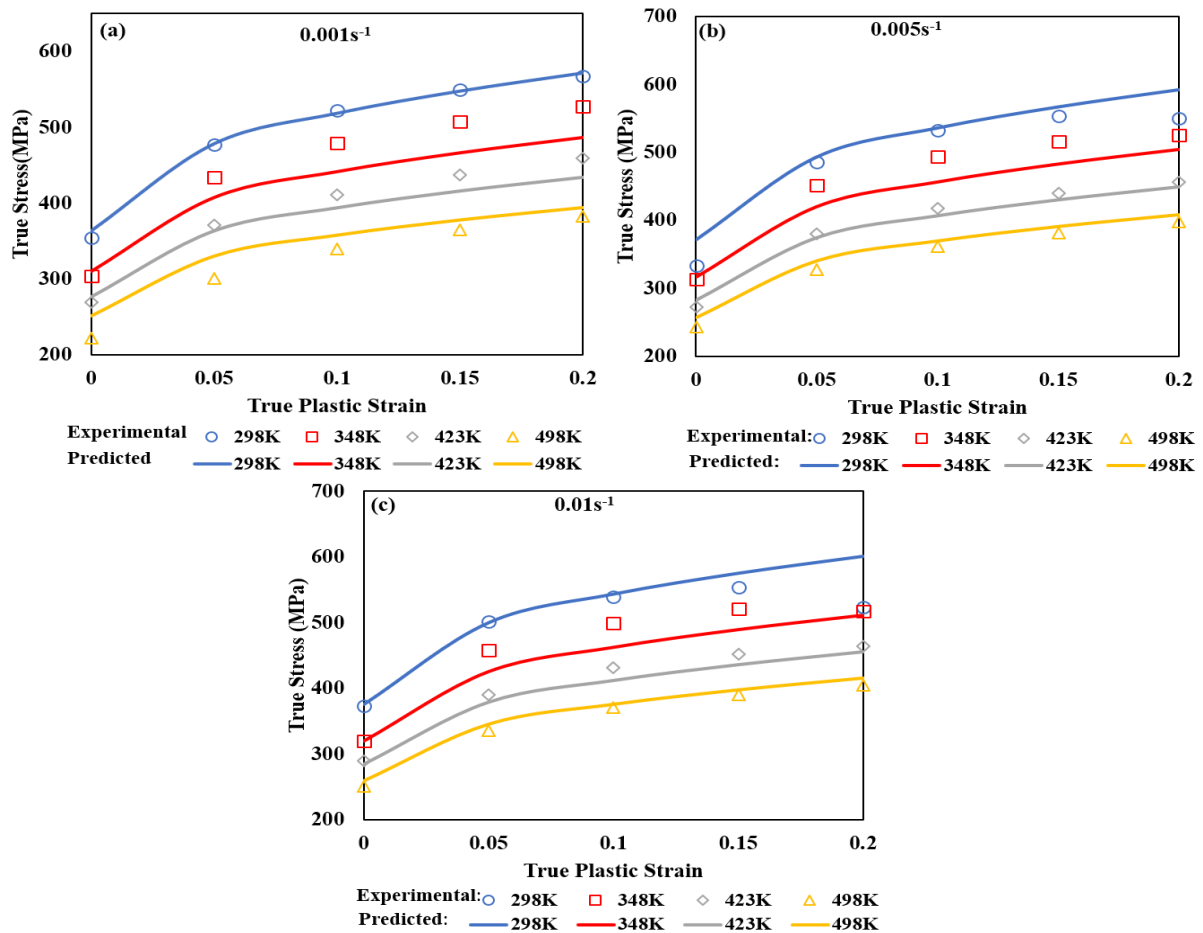


Fig. 5.5: The true stress estimated using KHL model and experimental true stress at various strains and strain rates of (a)  $0.001s^{-1}$ , (b)  $0.005s^{-1}$ , and (c)  $0.01s^{-1}$  for SRS material.

**Case 2:** At low strains

At yield point the strain is very less therefore Eq 5.33 can be approximated as Eq 5.37

$$\sigma \approx Ae^{C \ln(\dot{\epsilon}^*)} \quad (5.37)$$

$$\Rightarrow \ln\left(\frac{\sigma}{A}\right) = C \ln(\dot{\epsilon}^*) \quad (5.38)$$

Therefore, by plotting the linear graph between  $\ln\left(\frac{\sigma}{A}\right)$  and  $\ln(\dot{\epsilon}^*)$  the C value is determined as slope of the line. The C value for all the three materials are determined and listed in Table 5.7.

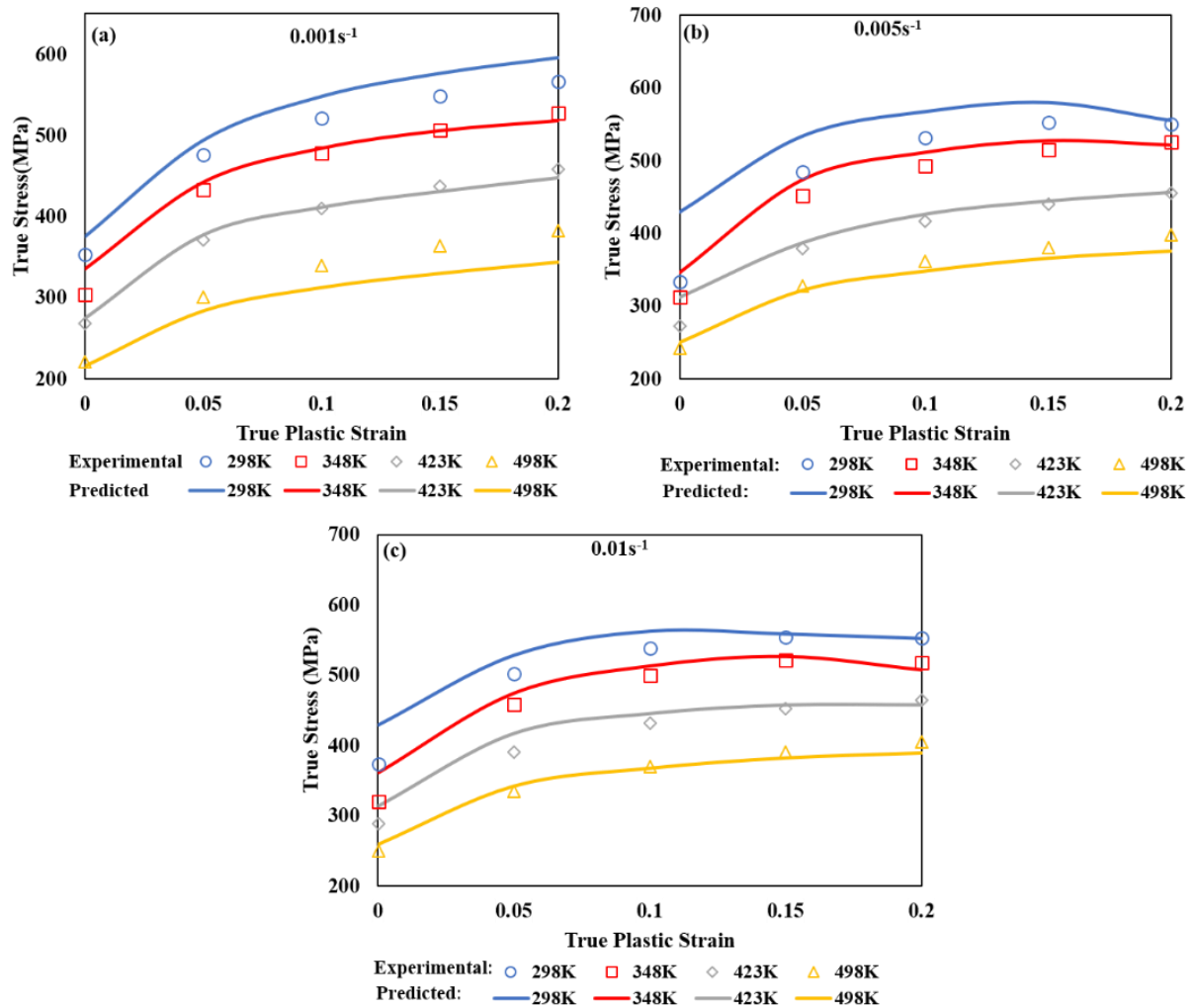


Fig. 5.6: The true stress estimated using KHL model and experimental true stress at various strains and strain rates of (a)  $0.001s^{-1}$ , (b)  $0.005s^{-1}$ , and (c)  $0.01s^{-1}$  for TRS material.

Table 5.7: Constants for KHL model

Material	A	B	$n_0$	$n_1$	m	C
LOS	337.86	461.73	0.3600	1.3135	0.5243	0.0583
SRS	353.75	415.05	0.4025	-0.3077	0.5308	0.0128
TRS	375.26	468.71	0.4519	0.4853	1.2257	0.0632



**Case 3:** At reference temperature

At reference temperature the homologous temperature becomes zero therefore the Eq 5.33 is reduced to Eq 5.39

$$\sigma = \left[ A + B \left( 1 - \frac{\ln \dot{\epsilon}^*}{\ln D} \right)^{n_1} \epsilon^{n_0} \right] e^{C \ln(\dot{\epsilon}^*)} \quad (5.39)$$

By rearranging the terms in the Eq 5.39, the  $n_1$  can be calculated as given in Eq 5.40

$$n_1 = \frac{\ln \left( \frac{\frac{\sigma}{e^{C \ln(\dot{\epsilon}^*) - A}}}{B \epsilon^{n_0}} \right)}{\ln \left( 1 - \frac{\ln \dot{\epsilon}^*}{\ln D} \right)} \quad (5.40)$$

All the  $n_1$  values for the LOS, SRS and TRS are listed in Table 5.7.

The  $m$  value can also be calculated similar to the  $n_1$  as shown in Eq 5.41

$$m = \frac{\ln \left( 1 - \frac{\sigma}{K} \right)}{\ln(T^*)} \quad (5.41)$$

where,  $K = \left[ A + B \left( 1 - \frac{\ln \dot{\epsilon}^*}{\ln D} \right)^{n_1} \epsilon^{n_0} \right] e^{C \ln(\dot{\epsilon}^*)}$

The high temperature experimental values are used for calculating the average value of  $m$ .  $m$  and  $n_1$  values were initially calculated from the Eq 5.40 and Eq 5.41 but these values affected the correlation coefficient of the model. Therefore, for better prediction capability of the model, the set of  $m$  and  $n_1$  values are calculated from the unconstrained nonlinear optimization procedure which involves the error minimization.

The constants for the KHL model are determined and listed in the Table 5.7. By using the constant values determined for all the LOS, SRS and TRS materials, the KHL models for all the three materials can be expressed as given in the Eq 5.42-5.44.

$$\sigma = \left[ 337.86 + 461.73 \left( 1 - \frac{\ln \dot{\epsilon}^*}{\ln D} \right)^{1.3135} \epsilon^{0.3600} \right] e^{0.0583 \ln(\dot{\epsilon}^*)} (1 - T^{*0.5243}) \quad (5.42)$$

$$\sigma = \left[ 353.75 + 415.05 \left( 1 - \frac{\ln \dot{\epsilon}^*}{\ln D} \right)^{-0.3077} \epsilon^{0.4025} \right] e^{0.0128 \ln(\dot{\epsilon}^*)} (1 - T^{*0.5308}) \quad (5.43)$$

$$\sigma = \left[ 375.26 + 468.71 \left( 1 - \frac{\ln \dot{\epsilon}^*}{\ln D} \right)^{0.4853} \epsilon^{0.4519} \right] e^{0.0632 \ln(\dot{\epsilon}^*)} (1 - T^{*1.2257}) \quad (5.44)$$

The Fig. 5.4 - 5.6 shows predicted flow stress from Eq 5.42 – Eq 5.44 and experimental flow stress at different strain rates of 0.001s<sup>-1</sup>, 0.005s<sup>-1</sup> and 0.01s<sup>-1</sup> for LOS, SRS and TRS materials. The results show that the predicted flow stress is very close to the experimental values with high goodness of fit.

The capability of models is assessed by coefficient of correlation (R) value. The coefficient of correlation is a parameter by which the experimental and predicted values are compared with a linear relationship. The coefficient of correlation is given in the Eq 5.8.

The calculated R values for LOS, SRS and TRS materials are listed in Table 5.8 The R values indicate that the predicted values are in good agreement with the experimental true stress. The linear relationship indicating the R value is depicted in Fig 5.7. It is not that, the greater the R value higher is the predictability; the R values may be biased towards higher or lower values. Therefore, average absolute error ( $\Delta$ ), which is unbiased statistical parameter, also determined for assessment of the certainty. The values are calculated from the Eq 5.7. The calculated  $\Delta$  values for all the three materials are listed in Table 5.8. The  $\Delta$  values also are in good agreement with the prediction capabilities measured by the R values.

## 5.4 Comparison of constitutive models

The comparison of constitutive models carried out with the help of prediction capability and suitability. The prediction capability has been assessed by the statistical parameters such as correlation coefficient and average absolute error. The suitability of models has been judged based on the number of constants to be determined. The statistical parameters and number of constants of all the four models are listed in the Table 5.8. Fig 5.1-5.4 illustrates the comparison between experimental and predicted values of the low oxygen sheet Zircaloy – 4 material. As it can be understood from the graphs, the prediction of m-Arr is very close to the experimental

values whereas it is very much deviating in the case of JC model. It is also evident from the Table 5.8 that the average absolute error is around 11 times lower for the m-Arr compared to that of JC model.

The coefficient of correlation values listed in Table 5.8, for all the four types of Zircalloys, the m-Arr has very high goodness of fit with more than 0.9899 R value, where as it is less for the JC model with only above 0.7023 R value. The R value is moderate for the m-ZA model that is above 0.9718. The coefficient of correlation values of JC model are very less compared to the other three models. It is due to, the JC model does not include the coupled effects of strain, strain rate and temperature together. The coefficient of correlation values may bias towards higher values or lower values therefore to check the proper predictability of the models the average absolute error is considered. The minimum average absolute error among all the three materials is obtained as 1.11% for the m-Arr whereas the maximum one is 12.83% for JC model. The limitation of the m-Arr is that it has a greater number of constants to find compared to the other models. Also, the regression constants  $\beta_0$ ,  $\beta_1$ , and  $\beta_2$  are not just three constants but they are varying with strain rate and temperature. Therefore, for each strain rate and temperate combination there exist a regression constant as shown in Tables 5.4-5.6. In this context the JC model is fit due to a smaller number of constants to evaluate but it has high average absolute error and less goodness of fit. Even though the m-Arr has more number of constants to be evaluated, it gives very high goodness of fit and less absolute average error compared to the other two models.

Table 5.8: Comparison of prediction by statistical parameters

	JC Model				m-ZA Model				m-Arr Model				KHL Model			
	R	$\Delta(\%)$	NC	std	R	$\Delta(\%)$	NC	std	R	$\Delta(\%)$	NC	std	R	$\Delta(\%)$	NC	std
LOS	0.7262	11.1421	5	10.73	0.9765	4.4640	7	2.24	0.9950	1.1132	9	1.98	0.9395	4.5742	6	2.94
SRS	0.7261	12.8346	5	11.46	0.9788	4.3042	7	2.65	0.9899	1.3215	9	2.11	0.9423	3.9938	6	3.25
TRS	0.7023	12.2308	5	11.19	0.9718	4.0847	7	4.69	0.9899	1.3215	9	1.83	0.9398	4.7436	6	4.8

NC\* = Number of constants

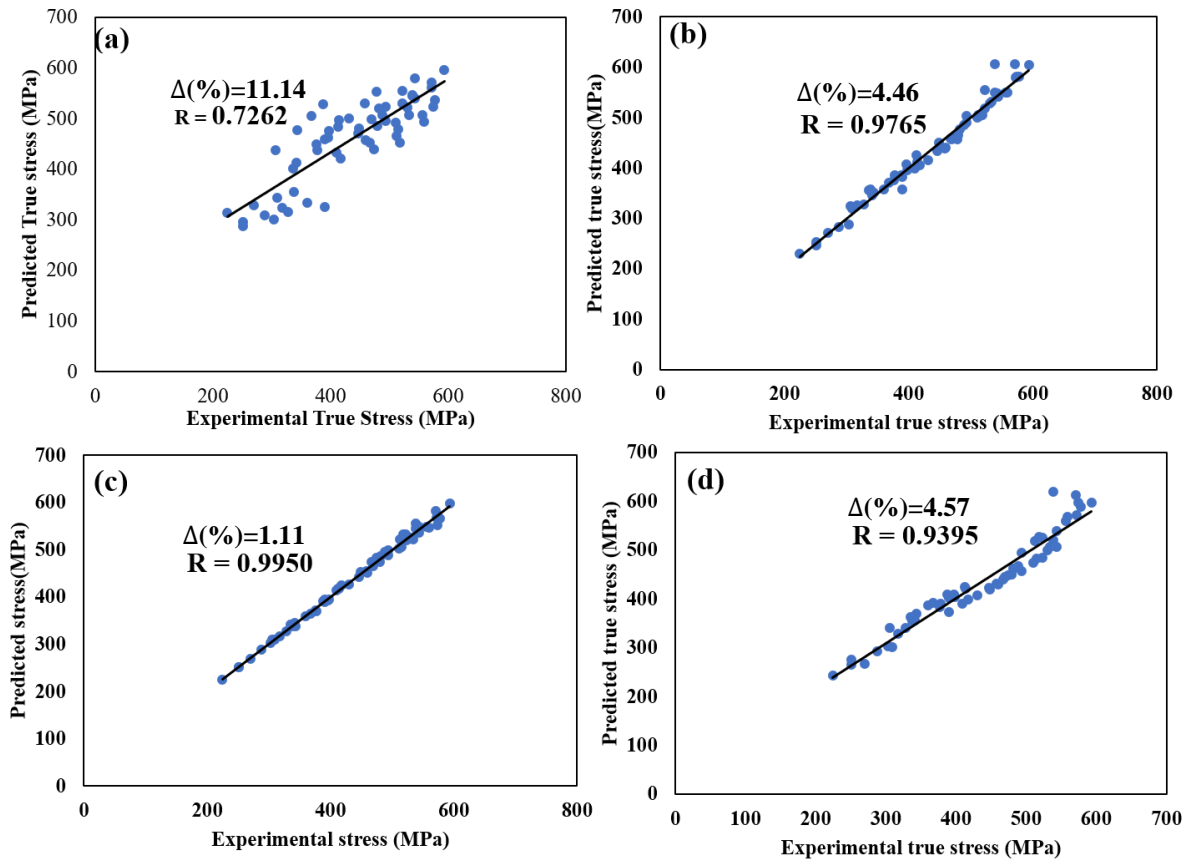


Fig. 5.7: Coefficient of correlation of (a) JC, (b) m-ZA, (c) m-Arr and (d) KHL for LOS

However, the m-Arr, JC and KHL constitutive equations come under the phenomenological models. It means they do not consider the physical aspects during the prediction of flow stress. On the other hand, the m-ZA is a physical based model. It considers the physical aspects such as dislocation movements which activates thermally, thermodynamics theory, kinetics of slips etc. Hence, sometimes, physical based models are

preferred more compared to the phenomenological models. But more important parameters in selecting the constitutive model is high goodness of fit and less absolute average error. Among the four models the *m-Arr* has high goodness of fit and less absolute average error.

The discussion considers most of the aspects such as statistical parameters, phenomenological and physical aspects and number of constants to be evaluated. The results show very clear indication with the consideration of  $R$  and  $\Delta(\%)$  that the *m-Arr* is very much suitable model for all the three types of Zircaloy-4 materials for the prediction of flow stress even though it has a greater number of constants to be evaluated. Along with the constitutive models, it is also important to model the material anisotropy for FE simulations.

## 5.5 Summary

The work materials are subjected to tensile tests and experimental data is used to calibrate constitutive models. From the calibrated models the following points can be made:

- (1) Johnson Cook model is calibrated for all the three types of Zircaloy-4 materials and it is resulted in very poor goodness of fit with maximum  $R$  value of 0.7262 and minimum average absolute error of 11.1421% for LOS among the three materials.
- (2) Modified Zerilli-Armstrong model is calibrated for all the three types of Zircaloy-4 materials and it is resulted in moderate goodness of fit with maximum  $R$  value of 0.9788 and delta value of 4.3042% for SRS among the three Zircaloy-4 sheet materials.
- (3) Modified Arrhenius type equation is calibrated for LOS, SRS and TRS materials and it is resulted in very high goodness of fit with maximum  $R$  value of 0.9950 and minimum delta value of 1.1132% for LOS material among the three materials.
- (4) The comparison among the three types of constitutive equations for all the three materials show that the *m-Arr* is suitable for good predictability of flow stress even though it has a greater number of constants to be determined.

Hence, in chapter 3, 4 and 5 the uniaxial flow stress behaviour Zircaloy-4 has been studied. However, the biaxial deformation of the material is studied as formability of Zircaloy-4 sheets in next chapter.

# Chapter 6

## Formability of Zircaloy-4

### 6.1 Introduction

In 1960's the construction of forming limit diagrams was started. Thereafter, the research underwent to see the effects of different parameters on the forming limit curves of the materials. The parameters include lubrication on the sample, sample dimensions, blank holding force, tool dimensions etc. Further, theoretical prediction of the forming limit curves has been come into picture. In the present work, the formability limits of the Zircaloy-4 at room temperature are analysed in terms of FLDs in three different sample orientations: rolling, 45° to rolling (radial) and 90° to rolling (transverse) directions. FE simulations are conducted and validated with experimental data. Limiting dome height is measured and strain distribution profiles are also plotted. Further, the results are compared with theoretically calibrated FLDs.

### 6.2 Experimental details

Forming limit diagram (FLD) is often used as a diagnostic tool for formability prediction in sheet metal forming processes. In the present study, forming limits of Zirconium-4 alloy sheets were evaluated using a laboratory scale LDH set-up consisting of  $\phi 50$  mm sub-sized hemispherical punch. The schematic diagram of test set-up is shown in Fig. 6.1(a). The tools such as lower die, upper die, and punch were mounted in a 100 ton double action hydraulic press. The blanks were placed between the lower and upper die, and the exact centering of the blank was ensured before conducting the forming experiments. In order to restrict the flow of sheet material into the die cavity, the circular groove of lock bead at a diameter of 99 mm was provided in the lower die and the boss of the lock bead at the corresponding location was provided in the upper die. Fig. 6.1(b) depicts the circular specimen of 150mm diameter and the Hasek specimens of 25mm width used to evaluate the forming limits of the material.

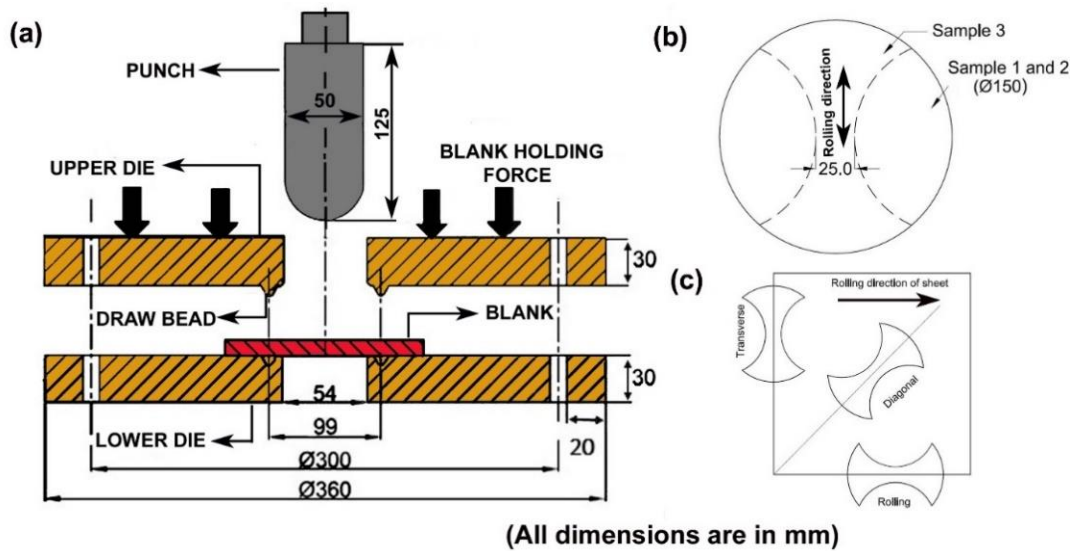


Fig. 6.1: Schematic diagram of (a) LDH test facility with tooling, (b) specimen geometries, and (c) samples cut along different orientation with respect to the sheet rolling direction.

Sample 1 represents the 150 mm circular shape blank where sufficient lubrication using polyethylene sheet with hydraulic oil was used on the circular blank to impose deformation close to equi-biaxial strain path, and dry condition (without lubrication) was used to induce near to plane strain path in the material. Hasek specimen of the same length with a narrower width of 25 mm (Sample 3) was used to achieve tension-compression strain path during deformation. The samples were prepared using milling process along three orientation of sheets namely rolling ( $0^\circ$ ), diagonal ( $45^\circ$ ), and transverse ( $90^\circ$ ) direction with respect to the rolling direction of the sheet as shown in Fig. 6.1 (c).

Prior to deformation, circular grids of 5 mm diameter were imprinted on the surface of blanks using screen printing technique to evaluate the major and minor strains of the deformed blank. The blank-holding force (BHF) was applied within a range of 6-15 ton and the punch was moved at a deformation speed of 20 mm/min. The blanks were stretched with the progression of punch movement, and a mirror was placed below the lower die to observe the appearance of necking/failure during the test. The circular grids turned into ellipses after deformation, and both the major and minor diameters were measured using Leica Stereo zoom





deformed specimens were plotted in the true principal strain locus as shown in Fig 6.2(b). Different clusters of strain data were achieved based on the lubrication and specimen geometry, and hence, it was evaluated by defining strain ratio ( $\alpha = \varepsilon_2 / \varepsilon_1$ ). The line 'OA' denotes the strain path obtained by deforming the sample 1, and it was observed that the strain ratio ( $\alpha = 0.76$ ) was close to equi-biaxial tension ( $\alpha = 1$ ) mode. The line 'OB' represents the deformation path of sample 2 which induced the strain path ( $\alpha = 0.18$ ) closer to plane strain condition whereas the deformation of sample 3 produced tension-compression deformation mode denoted by path 'OC'. Different colors were assigned to distinguish the safe strains from the fractured strains. Thus, as a demarcation of forming limits, a line was drawn separating safe and failure strains to obtain the forming limit diagram (FLD) as shown in Fig. 6.2(b). It is important to note that the slope of the line on the left-hand side FLD was approximate -1.1 whereas on the right-hand side the value was -0.6. These negative trends of the slopes indicate the formability of the material decreased drastically from tension-compression region to equi-biaxial tension region. This also signifies that material possesses higher draw ability in comparison to that of the stretchability.

#### **6.4 Finite element modeling and validation of the FLD**

Numerical simulations of stretch forming process were carried out using a commercially available explicit dynamic solver of LS-Dyna. To reduce the computation time, a quarter symmetric model of tool and blank were modeled as shown in Fig. 6.3. Further, analytical draw bead was provided on the die, and the BHF was applied in a downward direction to ensure that the motion of blank was restricted, and hence inducing tensile stretching in the blank. All the tools were assigned as rigid bodies whereas blank was considered to be deformable body incorporating anisotropy properties. Also, the mechanical properties such as yield strength, strength coefficient, strain hardening exponent obtained from the uniaxial tests were incorporated into the material model. The strain ratio and strain rate sensitivity index are also very useful in deciding the material behaviour (Singh 2010). Barlat-89 yield function was

chosen as the material model, and this was expressed in terms of plane stress state as shown in Eq.6.3 and Eq.6.4.

$$a|k_1 + k_2|^M + b|k_1 - k_2|^M + c|2k_2|^M = 2\sigma_e^M \quad (6.3)$$

$$k_1 = \frac{\sigma_x + h\sigma_y}{2} ; k_2 = \left[ \left( \frac{\sigma_x - h\sigma_y}{2} \right)^2 + \rho^2 \tau_{xy}^2 \right]^{0.5} \quad (6.4)$$

Where,  $\sigma_e$  is the effective stress,  $k_1$  and  $k_2$  are invariants of the stress tensor while  $M$  is an integer exponent.  $a, b, c, h$  and  $\rho$  represents anisotropy coefficients which can be expressed in terms of Lankford anisotropy parameters. In addition to this, the experimentally evaluated FLD was incorporated into the FE codes as fracture criterion. Subsequently, the predicted LDH and strain distribution results were compared with the experimental data.

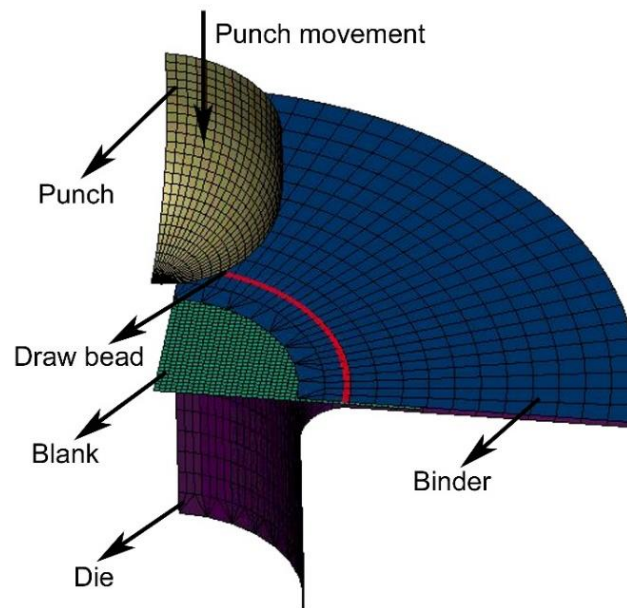


*Fig. 6.3: Finite element model of stretch forming process.*

In order to validate the experimental FLD, it was implemented in the FE model to predict failure. The fracture occurred when the deformation path intersected the incorporated FLD and corresponding FE predicted cups for all the three cases are shown in Fig. 6.4. It can be observed that the predicted strain paths were close to the experimental strain ratios viz. near

to equi-biaxial tension, near to plane strain and tension-compression region. Further, the formability parameters in terms of LDH and strain distribution of predicted results were compared with the experimental data as elaborately discussed in following subsections.

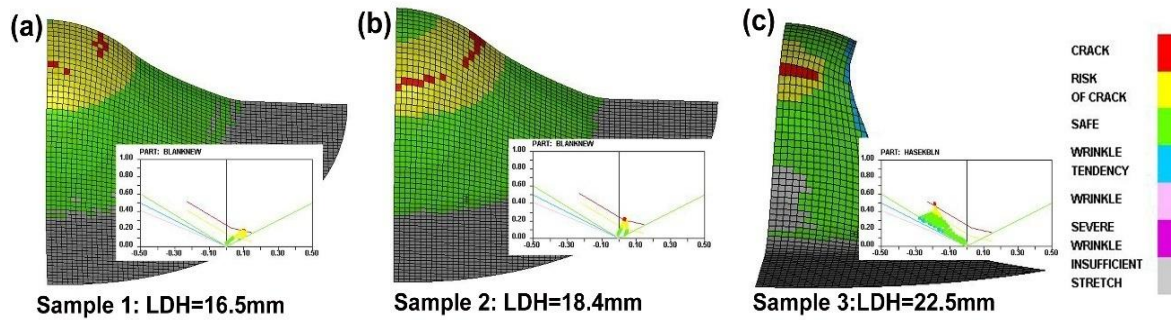


Fig. 6.4: FE predicted cups of (a) sample 1, (b) sample 2, and (c) sample 3 at time step when the deformation path intersects the experimental FLD.

## 6.5 Limiting dome height

The limiting dome height (LDH) of experimentally obtained and predicted results for all three deformation paths were consolidated and compared in Table 6.1. It is evident from the table that the LDH value obtained experimentally showed a decreasing trend from tension-compression (25.45 mm) to equi-biaxial tension (17.17 mm) region showing an agreement with the lower formability on the right-hand side of FLD in comparison to that of the left side. A similar trend was also observed for the predicted LDH. However, the model slightly under-predicts the dome height from the experimental values. The higher deviation in LDH prediction was observed for sample 3 with approximate percentage error of 11.4%. Whereas the deviation was found to decrease significantly by 9.6% and 3.8% for sample 2 and sample 1 respectively. To get more insight into the formability, the strain distribution was plotted along the longitudinal direction of the maximum deformed ellipse and were compared with the predicted results. The strain distribution profile is often referred as the '*strain signature*' of the sample.

Table 6.1: Comparison of experimental and predicted LDH for different strain paths.

Specimen	Experimental LDH (mm)	Simulated LDH (mm)	Error Percentage
Sample 1	17.17	16.51	3.8%
Sample 2	20.35	18.39	9.6%
Sample 3	25.45	22.53	11.4%

## 6.6 Forming limit diagrams of TRS in three sample directions

The samples along different orientations with respect to rolling direction of the sheet were stretch-formed to evaluate the forming limits. Fig. 6.5 shows the deformed samples along different strain path for rolling direction of the sheet. The strains were measured along maximum safe and fractured regions of all the deformed specimens and were plotted in the true principal strain locus as shown in Fig. 6.6. It was observed that the plotted strains were scattered along whole domain, and hence, different colors were assigned to distinguish the safe strains from the fractured strains.

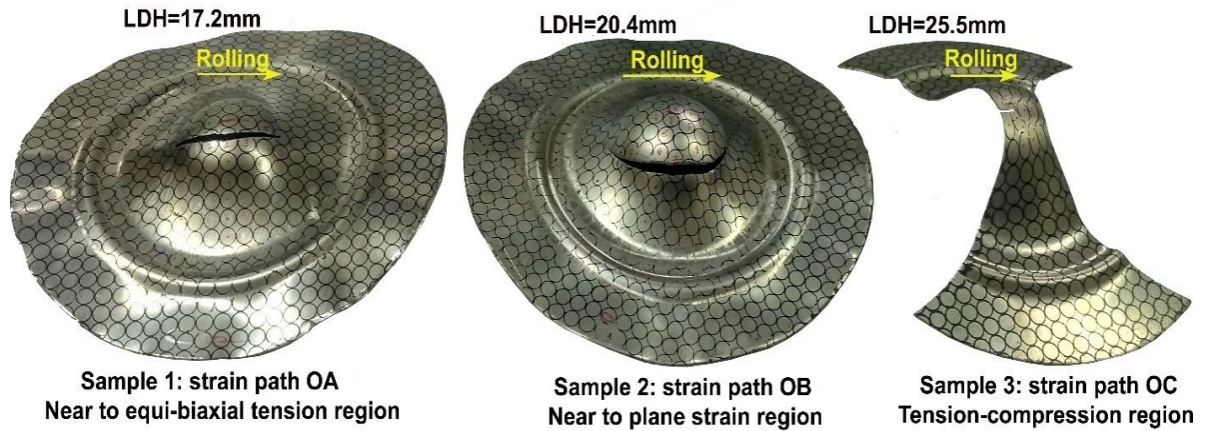


Fig. 6.5: Deformed stretch formed specimens along rolling direction of the sheet.

Fig. 6.6.(a) shows the measured strain in the principal strain space for the specimens deformed in the rolling direction. The line 'OA' denotes the strain ratio ( $\alpha = \frac{\epsilon_2}{\epsilon_1} = 0.76$ ) close to equi-biaxial tension ( $\alpha = 1$ ) mode obtained by deforming sample 1. Deformation path of sample 2 was represented by 'OB' which induced the strain path ( $\alpha = 0.18$ ) closer to plane strain

condition whereas the deformation of sample 3 produced tension-compression deformation mode denoted by path 'OC'. While conducting experiments, it was observed that all the specimens failed without any hint of localized necking. Thus, as a demarcation of forming limits, a line was drawn separating safe and failure strains to obtain the FLD.



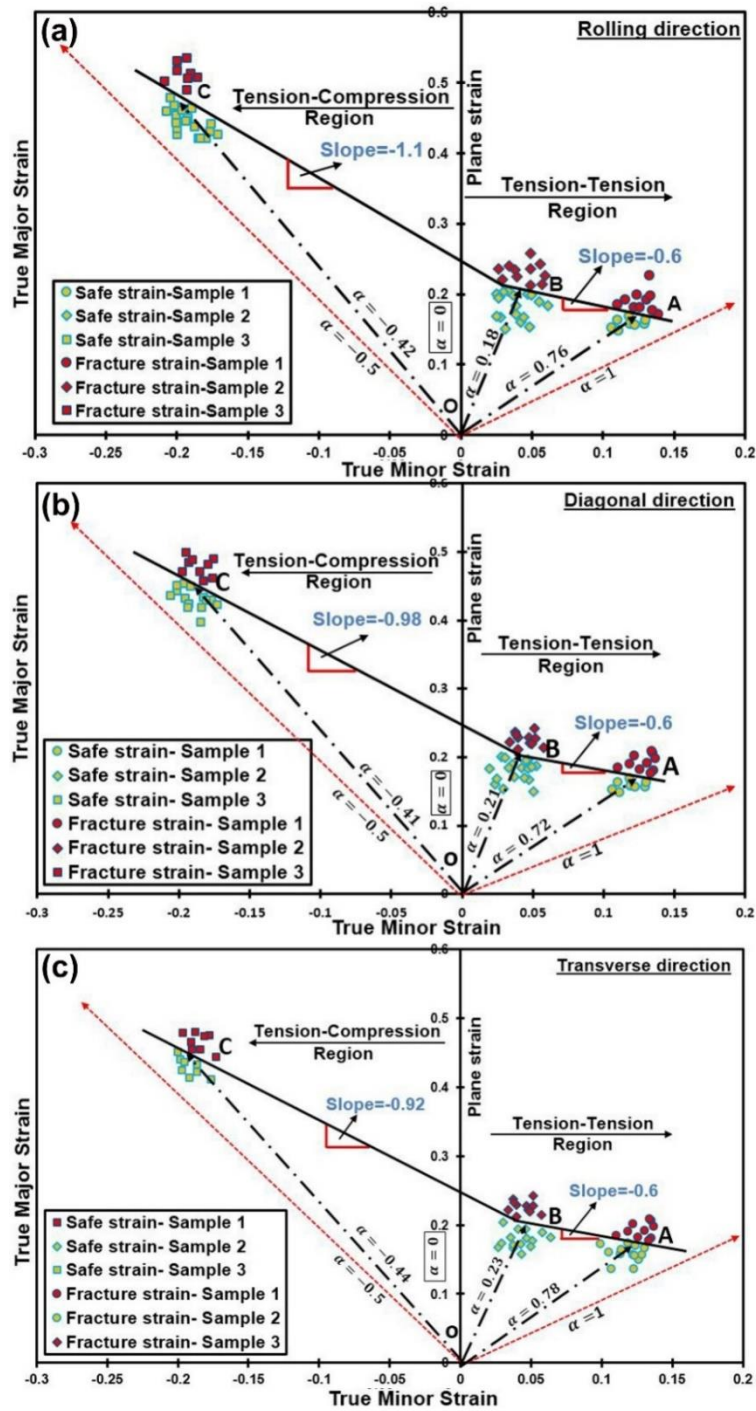


Fig. 6.6: Forming limits of Zirconium-4 alloy along (a) rolling, (b) diagonal, and (c) transverse direction of the sheets.

It is noteworthy to understand that the slope of the line on the left-hand side FLD was approximate -1.1 whereas on the right-hand side, the value was -0.6. This negative trend of the slopes indicated the formability of the material decreased drastically from tension-compression region to equi-biaxial tension region. Moreover, the decreasing trend in the formability is in

agreement with catastrophic decrease in the LDH value. It is noteworthy that the LDH of sample 3 was around 25.5mm, and the LDH value decreased by approximately 20% and 33% for sample 2 and sample 1 as compared to sample 3 respectively. This also signifies that material possesses higher drawability in comparison to that of the stretchability. Similar trend in the FLDs were observed for both diagonal and transverse direction specimens as shown in Fig 6.6(b) and 6.6(c) respectively.

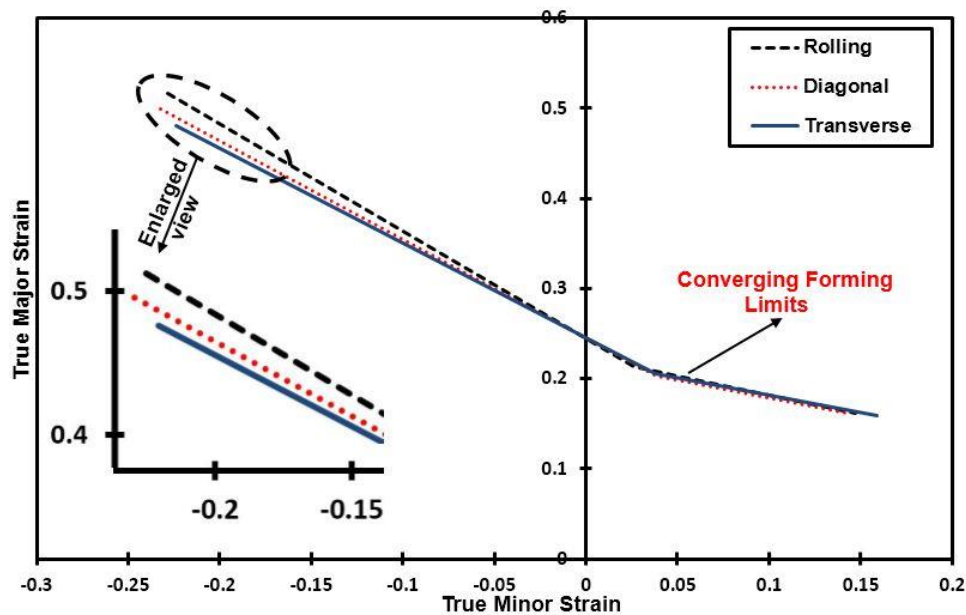


Fig. 6.7: Forming limits comparison along rolling, diagonal, and transverse direction of the sheet.

Fig. 6.7 represents the comparative FLD along three directions of the sheet. It was observed that on the right-hand side of FLD, there exists a very negligible difference in the forming limits among all the three direction, whereas marginal difference was observed along tension-compression region as depicted by the enlarged view in the Fig. 6.7. The true major strain for rolling direction specimen was recorded to be around 0.51 while for the diagonal and transverse direction the values were around 0.49 and 0.45 respectively. This variation in the true major strain values ensured different drawability of the material with respect to the orientation of the sheet.



## 6.7 Strain distribution on TRS.

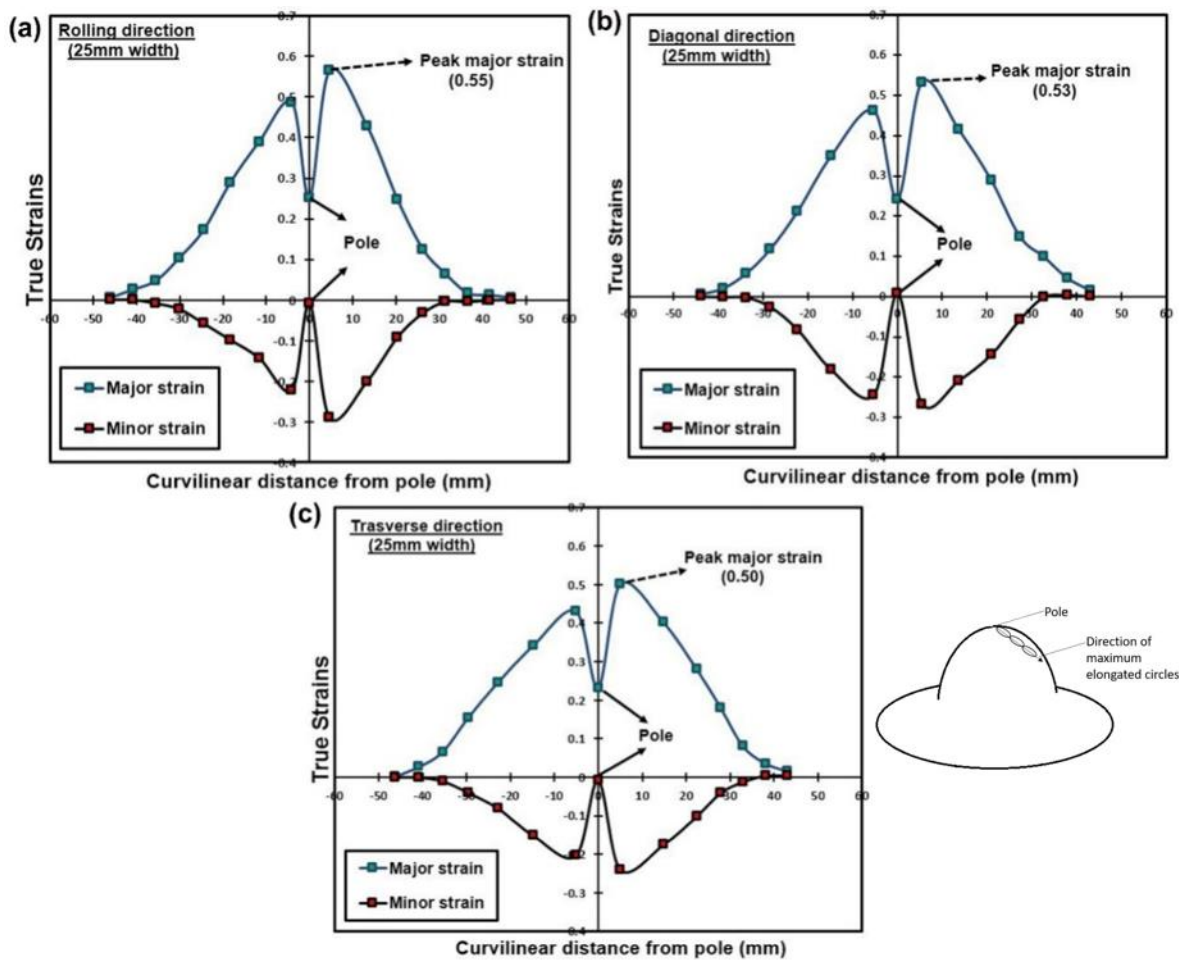


Fig. 6.8: Strain distribution profile of 25mm width Hasek specimen along (a) rolling, (b) diagonal, and (c) transverse orientation with respect to rolling direction of sheet.

It is vital to have the knowledge of strain induced over the final component. Generally, the strain distribution is plotted along the longitudinal direction of maximum deformed ellipse, and is often referred as the '*strain signature*'. Fig. 6.8 shows the strain distribution profile of sample 3 along rolling, diagonal, and transverse direction. The true strains are plotted as a function of highest position (pole) on the stretch formed cup. It was observed that the true major strain showed positive values across the profile whereas negative (compressive) minor strain was observed due to lateral drawing in the specimen. All the three directions of sample 3 exhibited similar trend in true major and minor strain profile. However, the peak strain level

changed with respect to the orientation of the specimens. It was observed that the peak major strain for rolling direction specimen was around 0.55, and the value was found to be decrease for diagonal and transverse direction specimens with an approximate value of 0.53 and 0.50 respectively. The highest peak strain along rolling direction is in agreement with the higher strain hardening exponent value of 0.093 as compared to that of the 0.087 and 0.081 for diagonal and transverse direction specimens respectively. The peak major strain was observed at an approximate distance of 5 mm from the pole which coincides with the failure location for all the samples.

As discrepancy in the FLD towards the right-hand was very negligible, the strain distribution of sample 2 and sample 3 along the rolling direction was considered. Fig. 6.9(a) shows positive major and minor strain profile of sample 2 indicating that the specimen had induced biaxial tensile straining. However, comparatively lower magnitude of minor strain profile signified that the deformation was closer to plane strain mode. It was also observed that the peak major strain was at 20mm from the pole, and the value decreased drastically by approximately 52% as compared to that of the tension-compression condition. Fig. 6.9(b) represents the strain distribution of sample 3 where both major and minor strain profile displayed the well-developed positive strains representing biaxial tensile deformation mode. As the minor strain profile was closer to the major strain profile, the deformation mode was near to the equi-biaxial tension mode. However, the development of the major strain was lower compared to that of sample 1 and 2 which is in agreement with the lower limit in the FLD as mentioned in the Fig. 6.7. Hence, it can be concluded that the strain signature completely depends on the strain path during deformation inherited from the specimen design, and lubrication condition imposed in the Zirconium-4 alloy sheet materials.

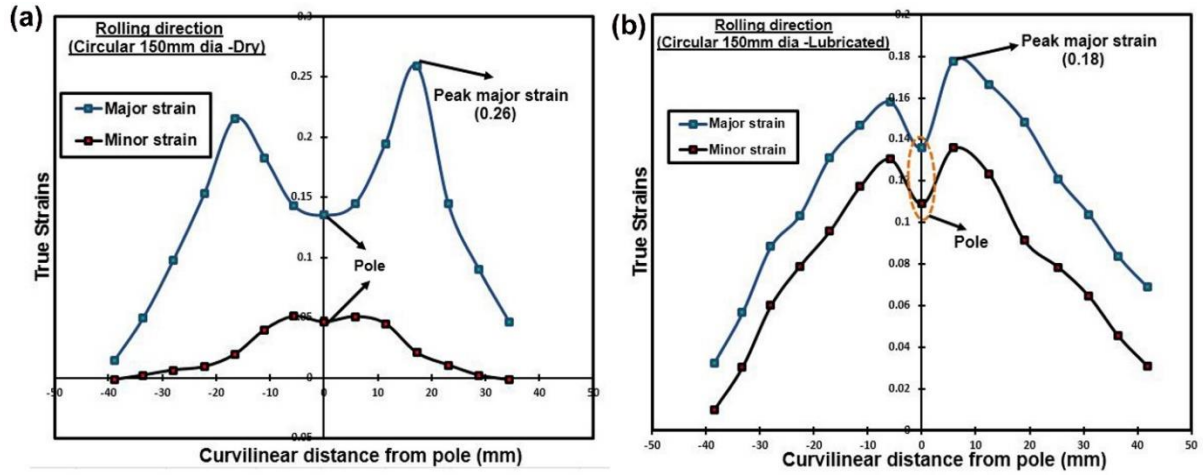


Fig. 6.9: Strain distribution profile along rolling direction for (a) dry condition, and (b) lubricated condition of 150mm circular blank.

## 6.8 Comparison of formability of SRS and TRS in three sample directions

The samples along three different orientations viz. rolling ( $0^\circ$ ), diagonal ( $45^\circ$ ), and transverse ( $90^\circ$ ) with respect to rolling direction of the sheet were stretch-formed to evaluate the forming limits of slab-route processed Zirconium-4 alloy. Fig.6.10 illustrates the deformed samples along different strain path for rolling direction of the sheet. The strains along maximum safe and fractured regions of all the deformed specimens were evaluated, and subsequently plotted in the true principal strain locus as shown in Fig. 6.11.

Fig. 6.11(a) shows the measured strain in the principal strain space for the specimens deformed in the rolling direction. It was noticed that by deforming sample 1, the deformation occurred in the tension-compression mode, and the corresponding strain ratio ( $\alpha = \frac{\epsilon_2}{\epsilon_1} = -0.44$ ) is denoted

by line 'OA' in the figure. It was observed that the limiting strains are fairly high in the tension-compression region where the highest true major strain was around 0.55 with the corresponding true minor strains of nearly 0.18. This observation represented that sheet material possess excellent drawability which is also in agreement with the higher ' $\bar{r}$ ' value (Gupta and Kumar 2006; Ravi Kumar and Swaminathan 1999). The line 'OB' represented the deformation path

induced by sample 2. It was found that the specimen followed a strain path ( $\alpha = 0.28$ ) closer to plane strain condition. For near to plane strain condition, true major strain was around 0.3 and true minor strain was approximately 0.1.

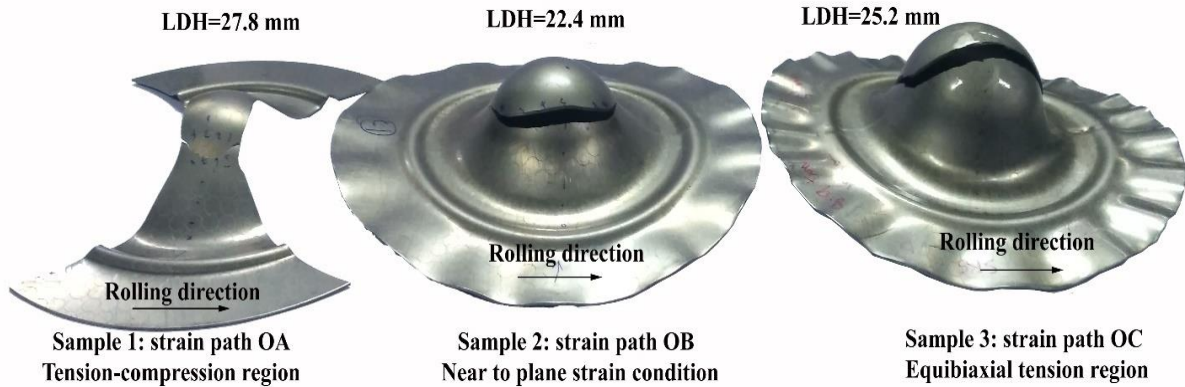


*Fig. 6.10: Stretch formed specimens deformed along different strain paths for rolling direction of the sheet.*

The deformation of sample 3 produced equi-biaxial tension deformation mode denoted by path 'OC'. The limiting strains were found to be around 0.38 and 0.24 for true major strain and true minor strains respectively. It is noteworthy that while conducting experiments all the specimens failed without any indication of localized necking. Thus, as a demarcation of forming limits, a line was drawn separating safe and failure strains to obtain the FLD. It is clearly evident from the figure that limiting strains were higher when the specimens were deformed along equi-biaxial tension deformation mode as compared to plane strain deformation mode. However, the material possessed maximum limiting strains near to tension-compression region. This was also in agreement with the limiting dome height (LDH) values as shown in Fig 6.8.1. The LDH value of sample 2 was around 22.4 mm, and the value was found to increase by approximately 24% and 12.5% for sample 1 and sample 3 as compared to sample 2 respectively. This also signifies that material possesses higher drawability in comparison to that of the stretch-ability. In similar manner, the limiting strain for diagonal and transverse direction was evaluated as shown in the Fig 6.11(b) and 6.11(c) respectively. The

formability of this material sufficiently comparable to that of superalloys IN625LCF and IN718 material (K. S. Prasad et al. 2017; K.S. Prasad et al. 2018; Roamer et al. 1997).

From Fig. 6.11, it was observed that the slope of the line on the left-hand side FLD was approximately -0.93 for rolling direction sheet. The values were around -0.91 and -0.88 for diagonal and transverse direction sheets respectively. This variation in the true major strain values ensured different drawability of the material with respect to the orientation of the sheet. The higher negative trend of the slopes on the left-hand side of FLD indicated the higher drawability of the material. Apart from these, the slope of line on the right-hand side of FLD was close to 0.32 for rolling direction. The higher positive slope on the right side of FLD denoted the improvement in the stretch-ability. The value of slope was higher for transverse direction, and it found to be marginally higher by 12% with respect to rolling direction of sheet.

Fig 6.12(a) and 6.12(b) represents the FLD of Tube route sheet (TRS) and slab route sheet (SRS) Zirconium alloy sheets respectively. It was observed that the limit strains of SRS sheets are higher when compared to that of the TRS sheets which is indicated by higher level of the FLD limit. The FLDs were consistently found to be higher for SRS alloy sheet in all the three orientation with respect to rolling direction of the sheet. In rolling direction, it was observed that limiting strains were found to be higher in tension-compression for SRS material as compared to TRS material. Also, the material possessed higher forming limits in the right side of FLD. This observation was consistently same for diagonal and transverse direction FLDs. Thus, this can be concluded that the SRS Zirconium alloy sheet possess more stretch-ability and drawability as compared to that of the TRS Zirconium alloy sheets and also these results are similar to that for experimental FLD of Zirlo (M. Kim et al. 2016). In order to understand the improvement in the formability, the strain distribution of both the materials were compared and discussed in the subsequently section.

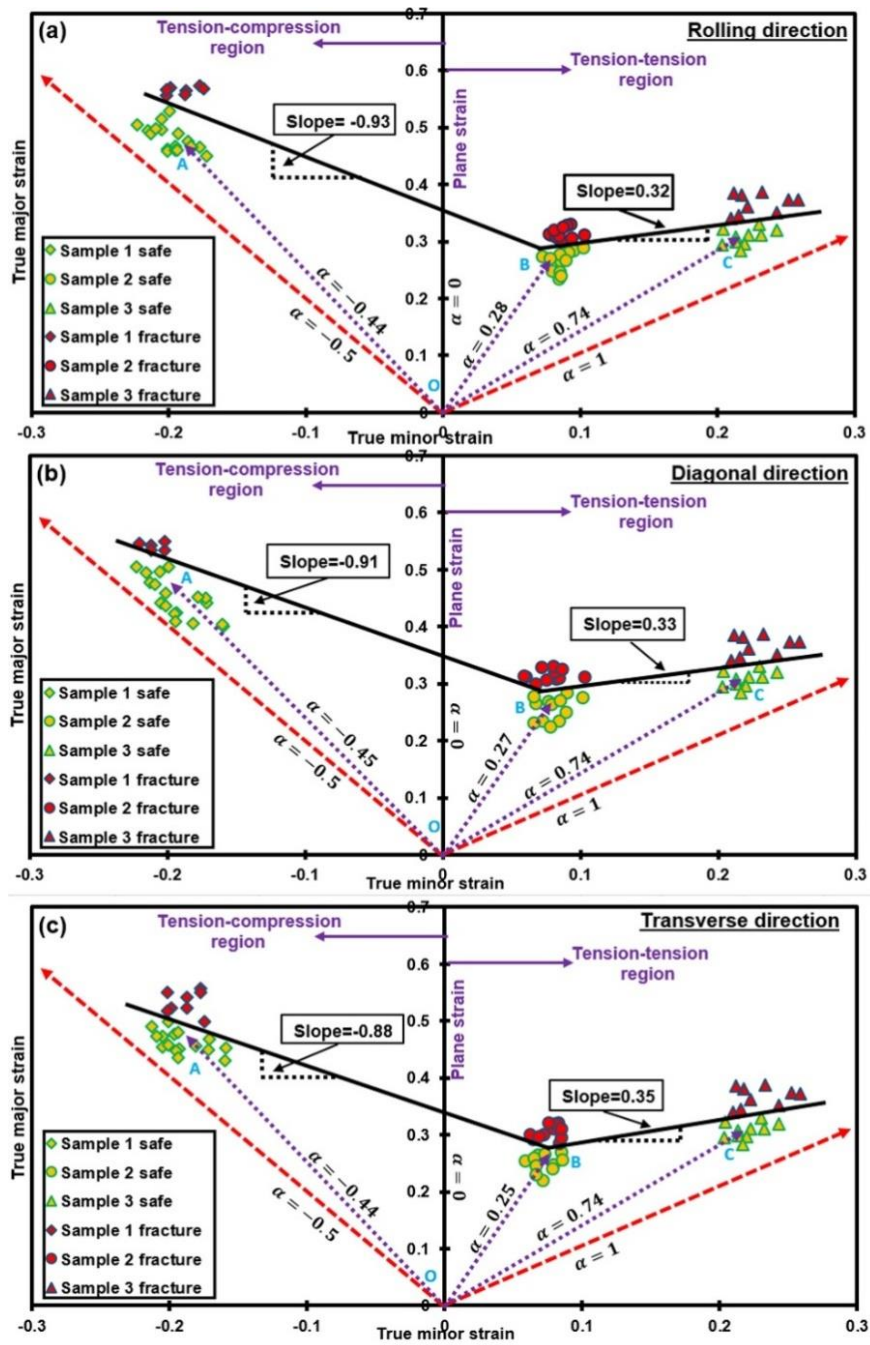


Fig. 6.11: Forming limits of slab-route processed Zirconium-4 alloy along (a) rolling, (b) diagonal, and (c) transverse direction with respect to the rolling direction of the sheets.

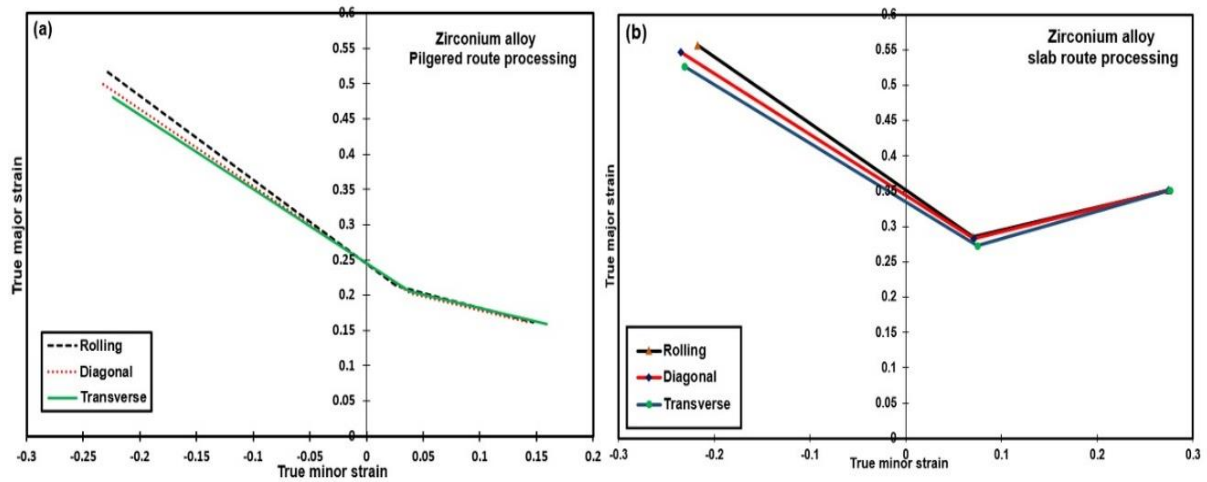


Fig. 6.12: Forming limit comparison between (a) Tube Route Sheet (TRS) and (b) Slab Route Sheet (SRS) Zirconium alloy along three direction of the sheets.

## 6.9 Comparison of strain distribution

Fig. 6.13 depicts the strain distribution profile of SRS sample 1 along rolling, diagonal, and transverse direction. The true strains are plotted as a function of highest position (pole) on the stretch formed cup. It was observed that the true major strain showed positive values (tension) across the profile whereas negative minor strain (compression) was observed due to lateral drawing in the specimen. All the three directions of sample 1 exhibited similar trend in true major and minor strain profile. However, the peak strain level changed with respect to the orientation of the specimens. The peak major strain was observed at an approximate distance of 7.2mm from the pole which coincides with the failure location for all the samples. It was observed that the peak major strain for rolling direction specimen was around 0.58, and the value was found to be decreased for diagonal and transverse direction specimens with an approximate value of 0.55 and 0.53 respectively.

For comparison, the strain distribution profile of TRS sample 1 along rolling, diagonal, and transverse orientation with respect to rolling direction of sheet are shown in Fig 6.14. The general features observed from the strain distribution profiles are very similar to that of the SRS sample. However, in SRS Zirconium alloy, strain gradients were found to be developed which implied uniform distribution of strain distribution and improvement in formability.



Moreover, it was observed that the peak strains were higher for SRS sheets as compared to TRS sheets. The results were consistently higher for SRS sheets in all the orientation with respect to the rolling direction of the sheet. It is well known that ‘*n*’ influences the ability of a material to distribute the strain uniformly.

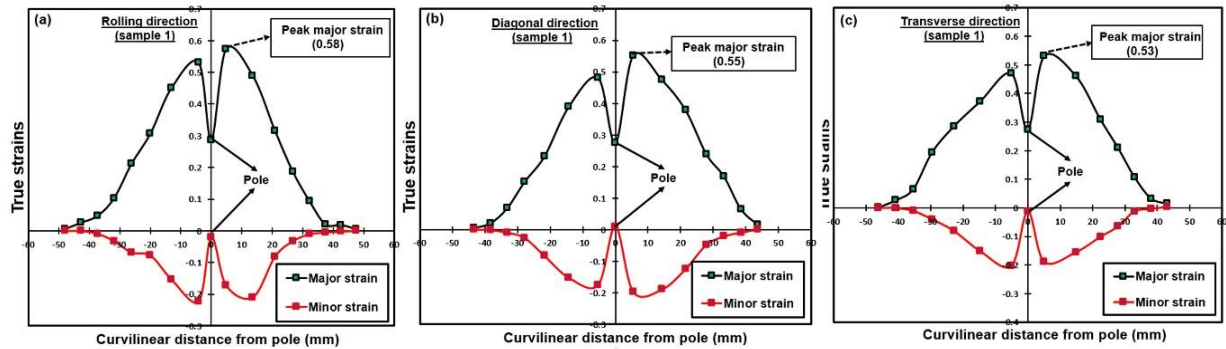


Fig. 6.13: Strain distribution profile of SRS sample 1 along (a) rolling, (b) diagonal, and (c) transverse orientation with respect to rolling direction of sheet.

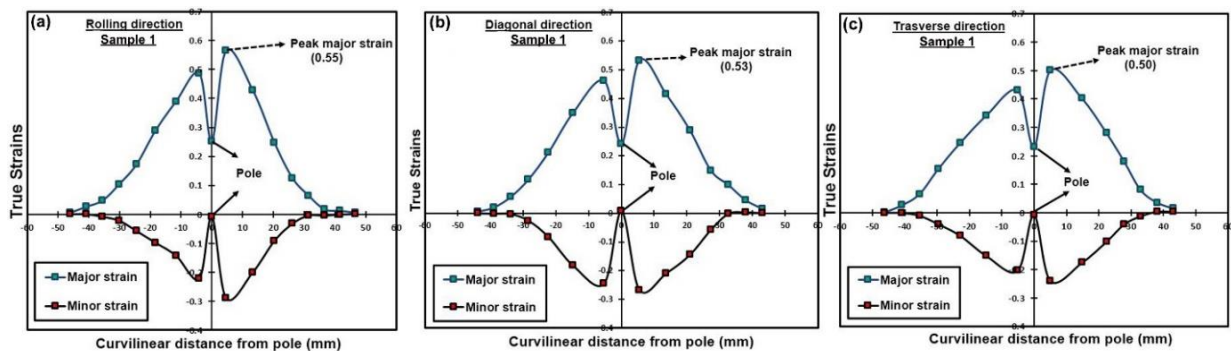


Fig. 6.14: Strain distribution profile of TRS sample 1 along (a) rolling, (b) diagonal, and (c) transverse orientation with respect to rolling direction of sheet.

Figs 6.15 and 6.16 represents the strain distribution profile for SRS and TRS sheets deformed along near to plane strain and equi-biaxial tension deformation mode respectively. As it can be seen from the Fig. 6.12 that forming limit along the right-hand side of the FLD showed a marginal difference in all the tested orientation. Hence, the strain distribution of sample 2 and sample 3 along the rolling direction was considered in the present work. Fig 6.15(a) shows positive major and minor strain profile (tension-tension) of sample 2 indicating that the specimen had induced biaxial tensile straining. However, comparatively lower



magnitude of minor strain profile signified that the deformation was closer to plane strain mode. The peak major strain of 0.30 was found to be at an approximate distance of 17mm from the pole. It was observed that the value was significantly reduced by around 48% as compared to the tension-compression deformation mode which also indicated the decrement in the formability. Fig 6.15(b) represents the strain distribution of sample 3 where both major and minor strain profile displayed the well-developed positive strains representing biaxial tensile deformation mode. As the minor strain profile was closer to the major strain profile, the deformation mode was near to the equi-biaxial tension mode. Also, the development of the major strain was higher by around 17% as compared to that of sample2 which is in agreement with the higher forming limit in the FLD as mentioned in the Fig.6.12. However, it was found that the major strain showed decrement of 39% in peak major strain as compared to tension-compression region.

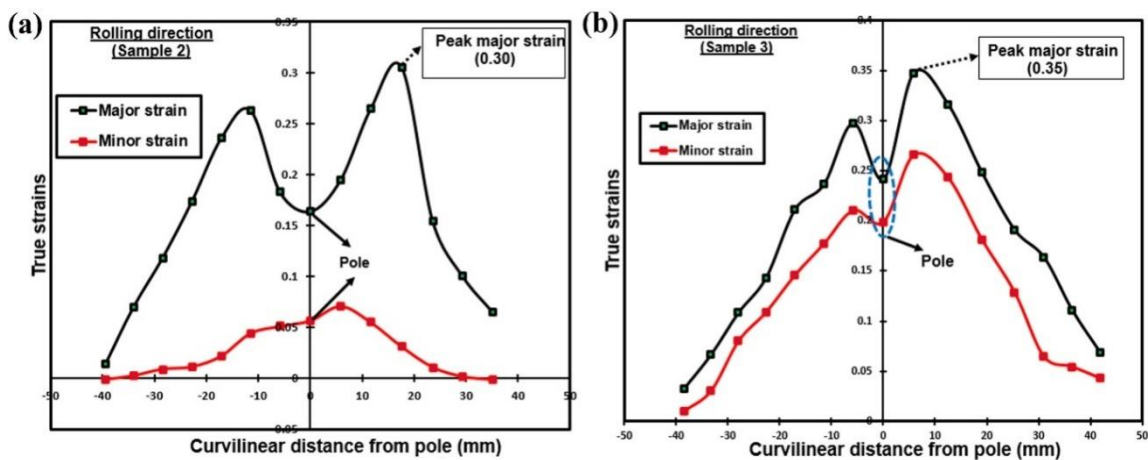


Fig. 6.15: Strain distribution profile of SRS sample along rolling direction for (a) sample 2, and (b) sample 3.

Further, the strain distribution of SRS was compared with the TRS material. It is clearly evident from Figs. 6.15 and 6.16 that though the both the materials showed same strain signature as compared to that of the TRS material, the strains were well developed in case of SRS material. In case of sample 2, the peak major strain was around 0.30 for SRS material

whereas the value was around 0.26 for TRS. This shows the improvement of formability of SRS material by approximately 13% with respect to TRS material. In case of sample 3, the peak strain was found to be 0.35 and 0.18 for SRS and TRS material respectively which signify drastic improvement of 95%. The above observations are in agreement with FLDs results as shown in the Fig. 6.11. Hence, it can be concluded that the material possesses both drawability and stretch-ability as compared to plane strain deformation.

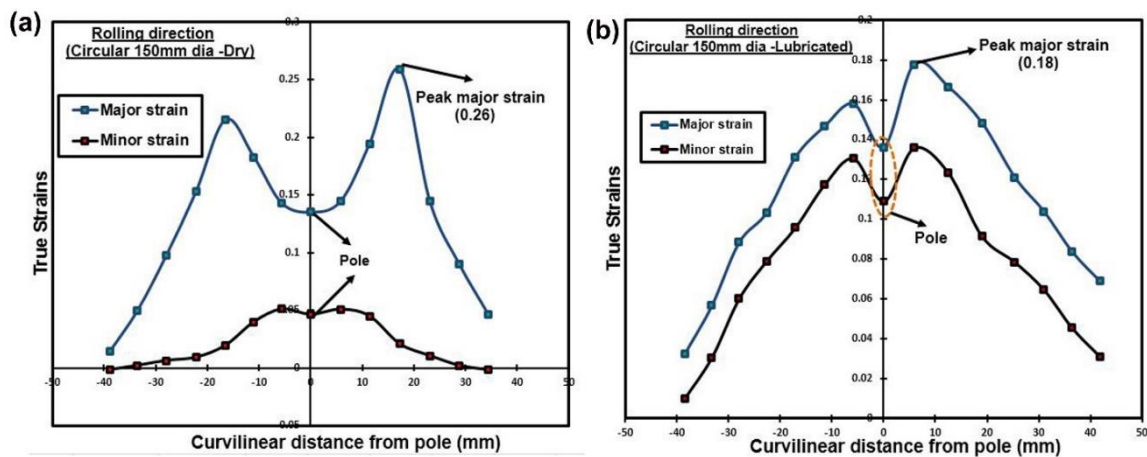


Fig. 6.16: Strain distribution profile of TRS sample along rolling direction for (a) sample 2, and (b) sample 3.

## 6.10 Theoretical forming limit diagrams

Throughout the analysis, Von Mises yield function and associated flow rule is used.

The Von Mises yield function is defined in Eq.6.5

$$\sigma_{eq} = f = \sqrt{\sigma_1^2 + \sigma_2^2 - \sigma_1\sigma_2} \quad (6.5)$$

where,  $\sigma_1$  is true major principal stress,  $\sigma_2$  is true minor principal stress and also the  $\sigma_3 = 0$  (plane stress condition is considered). The  $\sigma_{eq}$  is equivalent true stress.

The associated flow rule is defined in Eq.6.6

$$d\bar{\epsilon}^p = d\lambda \frac{df}{d\bar{\sigma}} \quad (6.6)$$

where,  $d\bar{\epsilon}^p$  is referred as true plastic strain rate,  $d\lambda$  is a proportionality constant and is equal to effective strain rate for uniaxial condition.

The strain ratio is given in the Eq.6.7.

$$\alpha = \frac{\varepsilon_2}{\varepsilon_1} \quad (6.7)$$

where,  $\varepsilon_2$  is minor true strain,  $\varepsilon_1$  is major true strain.

Similarly, stress ratio is defined in Eq.6.8.

$$\beta = \frac{\sigma_2}{\sigma_1} \quad (6.8)$$

where,  $\sigma_2$  is minor true stress,  $\sigma_1$  is major true stress.

The  $\alpha$  and  $\beta$  are inter dependent, the dependence can be derived from associated flow rule as expressed in Eq.6.9 and Eq.6.10

$$\alpha = \frac{2\beta-1}{2-\beta} \quad (6.9)$$

$$\beta = \frac{1+2\alpha}{\alpha+2} \quad (6.10)$$

The rate of change of yield function is expressed as shown in Eq.6.11

$$\frac{df}{d\bar{\varepsilon}^p} d\lambda = \frac{\partial f}{\partial \sigma_1} d\sigma_1 + \frac{\partial f}{\partial \sigma_2} d\sigma_2 \quad (6.11)$$

The power law is used in the entire analysis to represent stress-strain relation and it is expressed in Eq.6.12.

$$\sigma_{eq} = K\varepsilon_{eq}^n \quad (6.12)$$

Where, K is the strength coefficient, n is stain hardening exponent. Combining both equations, Eq.6.5 and Eq.6.8, the equivalent stress can be express as shown in Eq.6.13.

$$\sigma_{eq} = \sigma_1 \sqrt{1 - \beta + \beta^2} \quad (6.13)$$

Equivalent plastic strain increment can also be expressed as shown in Eq.6.14.

$$\varepsilon_{eq} = \frac{2}{\sqrt{3}} \varepsilon_1 \sqrt{1 + \alpha + \alpha^2} \quad (6.14)$$

Triaxility ( $\eta$ ) is defined as the ratio of equivalent stress ( $\sigma_{eq}$ ) to mean stress ( $\sigma_m$ ). It is expressed in Eq.6.15.

$$\eta = \frac{\sigma_m}{\sigma_{eq}} = \frac{1+\alpha}{\sqrt{3}\sqrt{1+\alpha+\alpha^2}} \quad (6.15)$$

Where, mean stress ( $\sigma_m$ ) is expressed in Eq.6.16

$$\sigma_m = \frac{1}{3}(\sigma_1 + \sigma_2 + \sigma_3) \quad (6.16)$$

All the above relations are used in the following section to derive FLC in different theoretical models.

**Swift model:**

According to this model, in principal directions of a material if load reaches to maximum, diffusion neck begins. The constraints for the diffusion neck are expressed in Eq.6.17.

$$\left. \begin{aligned} d\sigma_1 &= \sigma_1 d\varepsilon_1 \\ d\sigma_2 &= \sigma_2 d\varepsilon_2 \end{aligned} \right\} \quad (6.17)$$

The swift diffuse instability given Eq.6.18 can be derived by using Eq.6.6, Eq.6.11 and Eq.6.17. The detailed derivation the of the instability condition is given work done by Stoughton and Zhu's.

$$\begin{bmatrix} \varepsilon_1 \\ \varepsilon_2 \end{bmatrix} = \begin{bmatrix} \frac{2n(2-\beta)(1-\beta+\beta^2)}{4-3\beta-3\beta^2+4\beta^3} \\ -\frac{2n(1-2\beta)(1-\beta+\beta^2)}{4-3\beta-3\beta^2+4\beta^3} \end{bmatrix} \quad (6.18)$$

In the Eq.6.18, the  $n$  (power law exponent) is equal to the uniform elongation  $\varepsilon_{UL}$  and the  $\beta$  is calculated from Eq.6.10 where  $\alpha$  is strain ratio taken as the range between -0.5 to 0.5 (indicating uniaxial tension to equibiaxial tension region).

**Hill model:**

Hill assumed that local neck will form with an angle ( $\varphi$ ) to the direction of major principal stress. The angle is expressed in Eq.6.19.

$$\varphi = \tan^{-1}(\sqrt{-\alpha}) \quad (6.19)$$

In the Eq.6.19, there is a negative sign in the square route. Therefore, the instability expressed in Eq.6.20 has physical meaning only when the  $\alpha$  is negative. The balance between strain rate

effect and reduction in thickness is obtained exactly at local necking. From this the following local necking criterion is derived.

$$\frac{d\sigma_1}{d\varepsilon_1} = \sigma_1(1 + \alpha) \quad (6.20)$$

Hill's expression for the proportional strain condition is given Eq.6.21.

$$\varepsilon_1(1 + \alpha) = n \quad (6.21)$$

In the Eq.6.21, the strain hardening exponent  $n$  is equal to uniform elongation ( $\varepsilon_{UL}$ ) in uniaxial tensile test. Therefore, instead of  $n$ , the  $\varepsilon_{UL}$  can be used in Eq.6.21.

Now, the Hill's instability criterion is expressed in Eq.6.22.

$$\begin{bmatrix} \varepsilon_1 \\ \varepsilon_2 \end{bmatrix} = \begin{bmatrix} \frac{\varepsilon_{UL}}{1+\alpha} \\ \frac{\varepsilon_{UL} \times \alpha}{1+\alpha} \end{bmatrix} \quad (6.22)$$

From eq. (6.10), the equivalent strain for the Hill model can be expressed in Eq.6.23.

$$\varepsilon_{eq} = \frac{2\varepsilon_{UL}\sqrt{1+\alpha+\alpha^2}}{\sqrt{3}(1+\alpha)} \quad (6.23)$$

Therefore, from the power law equation, the equivalent stress for Hill model is shown in Eq.6.24.

$$\sigma_{eq} = K \left( \frac{2\varepsilon_{UL}\sqrt{1+\alpha+\alpha^2}}{\sqrt{3}(1+\alpha)} \right)^n \quad (6.24)$$

Therefore, from Eq.6.24, Eq.6.13 and Eq.6.8 the stress based FLC can also be derived as given in Eq.6.25.

$$\begin{bmatrix} \sigma_1 \\ \sigma_2 \end{bmatrix} = \begin{bmatrix} \frac{K(2+\alpha)}{\sqrt{3}\sqrt{1+\alpha+\alpha^2}} \left( \frac{2\varepsilon_{UL}\sqrt{1+\alpha+\alpha^2}}{\sqrt{3}(1+\alpha)} \right)^n \\ \frac{K(1+2\alpha)}{\sqrt{3}\sqrt{1+\alpha+\alpha^2}} \left( \frac{2\varepsilon_{UL}\sqrt{1+\alpha+\alpha^2}}{\sqrt{3}(1+\alpha)} \right)^n \end{bmatrix} \text{ for } \beta < 0 \quad (6.25)$$

### **Hill-Swift model (H-S):**

Hill-Swift model is developed by overcoming the limitations of the two models. The limitation of the Hill is that it is applicable only in negative  $\alpha$  region and the limitation of the Swift model is that poor appearance of the FLC in negative  $\alpha$  region. By combining both the models, it

means, taking the data of strains for negative region of  $\alpha$  from Hill model and for positive region of  $\alpha$  from Swift model, the Hill-Swift model is developed.

***Storen-Rice model (S-R):***

In plane strain condition, Storen and Rice, introduced a ‘bifurcation of the material’ concept to induce neck in the material. According to them, a vertex on the yield surface has discontinuity and its discontinuity increases until the plastic strain increment is possible in plane strain condition. From this state of condition, they come up with two solutions to form FLDs. Out of the two solutions, one solution is taken to derive the present model. The details of the study are discussed in Stoughton and Zhu’s studies. The derived expression for the bifurcation criterion is expressed in Eq.6.26.

$$\begin{bmatrix} \varepsilon_1 \\ \varepsilon_2 \end{bmatrix} = \begin{bmatrix} \frac{3\alpha^2+n(2+\alpha)^2}{2(1+2\alpha)(1+\alpha+\alpha^2)} \\ \frac{\alpha(3\alpha^2+n(2+\alpha)^2)}{2(1+2\alpha)(1+\alpha+\alpha^2)} \end{bmatrix} \quad (6.26)$$

***Bressan and Williams model (B-W):***

The model developed by Bressan and Williams (B-W) initially used to check the stability of sheets in ships by Alsos et al. To derive the model initially they considered three assumptions, firstly, during the deformation of the sheet material there is no influence of elastic strains. Secondly, shear instability starts in the direction of the thickness when there is no more elongation is found in the length direction. Finally, shearing of material starts when it exceeds a critical shear stress of the material. Shearing of the material starts in a particular orientation and it is expressed in Eq.6.27.

$$\theta = \frac{1}{2} \cos^{-1} \left( -\frac{\alpha}{2+\alpha} \right) \quad (6.27)$$

And also, the critical shear stress ( $\tau_{cr}$ ) value can be predicted by using the Eq.6.28.

$$\tau_{cr} = \frac{\sigma_1}{2} \sin 2\theta \quad (6.28)$$

By combining the Eq.6.27 and Eq.6.28 the Eq. 6.29 can be derived for major principal stress.

$$\sigma_1 = \frac{2\tau_{cr}}{\sqrt{1-\left(\frac{\alpha}{2+\alpha}\right)^2}} \quad (6.29)$$

Material constant calibration for the B-W model even though initially thought to find from uniaxial tensile test or biaxial tensile test but it was nonetheless find from plain strain condition or simply from Hill criteria where  $\alpha = 0$ . Therefore, from Hill criteria, in Eq.6.25 the  $\sigma_1$  value is equal to  $\tau_{cr}$  at  $\alpha = 0$ . The  $\tau_{cr}$  is expressed in Eq.6.30.

$$\tau_{cr} = \frac{K}{\sqrt{3}} \left( \frac{2n}{\sqrt{3}} \right)^n \quad (6.30)$$

In Eq.6.30 the  $n$  value is exactly equal to the elongation ( $\varepsilon_{UL}$ ), therefore,  $\varepsilon_{UL}$  can be used instead of  $n$ . Now, by combining the Eq.6.30 and Eq.6.29, the Eq.6.31 can be obtained.

$$\sigma_1 = \frac{\frac{2K}{\sqrt{3}} \left( \frac{2n}{\sqrt{3}} \right)^n}{\sqrt{1-\left(\frac{\alpha}{2+\alpha}\right)^2}} \quad (6.31)$$

Therefore, the stress based FLC of B-W model is expressed in Eq.6.32.

$$\begin{bmatrix} \sigma_1 \\ \sigma_2 \end{bmatrix} = \begin{bmatrix} \frac{K(2+\alpha)}{\sqrt{3}\sqrt{1+\alpha}} \left( \frac{2\varepsilon_{UL}}{\sqrt{3}} \right)^n \\ \frac{K(1+2\alpha)}{\sqrt{3}\sqrt{1+\alpha}} \left( \frac{2\varepsilon_{UL}}{\sqrt{3}} \right)^n \end{bmatrix} \quad (6.32)$$

The stress based FLC expressed in Eq.6.32, can easily converted by the fundamentals mentioned in Eq.6.7 and equations 6.12 – 6.14.

### **Hill-Tresca Model (H-T):**

According to this model, shear instability occurs in the material much before the visual necking happening and the shear instability is based on the slip mechanism. It means, deformation occur in the material when certain combination of crystallographic plane and direction is activated. Experiments reveal that the direction of the activated planes is close to the maximum shear stress direction. Therefore, for finding the local necking point, shear stress-based criteria such as Tresca's s maximum shear stress theory is used. In this model, for the

FLC in negative strain ratio region, Hill model is used and in positive strain ratio region Tresca's criterion is used.

In Tresca criterion, instability of the material starts when maximum shear stress exceeds a critical value. In the first coordinate portion of Tresca's hexagon, the distance from top side to the center of the hexagon can be expressed in Eq.6.33.

$$\sigma_1 = \sigma_T \quad (6.33)$$

where,  $\sigma_T$  is Tresca's stress at plain strain condition.

From Hill criterion, the equivalent strain can be obtained at plane strain condition by substituting  $\alpha = 0$  in Eq.6.23.

$$\varepsilon_{eqT} = \frac{2\varepsilon_{UL}}{\sqrt{3}} \quad (6.34)$$

where, the uniform elongation  $\varepsilon_{UL}$  is equal to strain hardening exponent  $n$  in power law.

Then, the equivalent stress according to the power law is given in Eq.6.35.

$$\sigma_{eqT} = K \left( \frac{2\varepsilon_{UL}}{\sqrt{3}} \right)^n \quad (6.35)$$

Therefore (by taking  $\alpha = 0$ , in Eq.6.25), the Tresca stress ( $\sigma_T$ ) can be defined as shown in Eq.6.36

$$\sigma_T = \frac{2K}{\sqrt{3}} \left( \frac{2\varepsilon_{UL}}{\sqrt{3}} \right)^n \quad (6.36)$$

Therefore, FLC in positive strain ratio region, is defined in Eq.6.37

$$\begin{bmatrix} \sigma_1 \\ \sigma_2 \end{bmatrix} = \begin{bmatrix} \frac{2K}{\sqrt{3}} \left( \frac{2\varepsilon_{UL}}{\sqrt{3}} \right)^n \\ \frac{(1+2\alpha) 2K}{(2+\alpha) \sqrt{3}} \left( \frac{2\varepsilon_{UL}}{\sqrt{3}} \right)^n \end{bmatrix} \quad (6.37)$$

The stress based FLC shown in Eq.6.37 can be converted in to strain based FLC by using the Eq.6.7 and equations 6.12 – 6.14.

All the four models (H-S, H-R, B-W and H-T) are constructed for Zrcalloy-4 (TRS) and shown in Fig. 6.17.



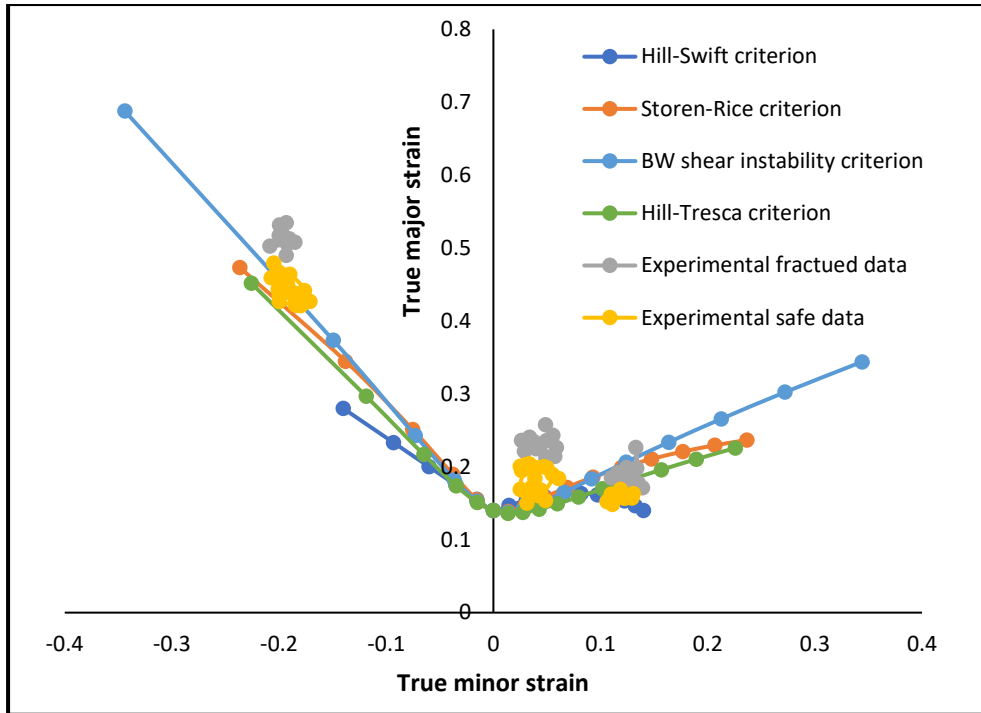


*Fig. 6.17: Comparison of theoretical FLDs with experimental FLDs.*

From the Fig. 6.17, it can be explained that among the four models, B-W shear instability criteria is predicting well in tension-compression region and at near plain strain region and H-S criterion is in good agreement with the experimental data at near equi-biaxial region.

## 6.11 Summary

Zircaloy-4 sheet materials, produced by pilgering method and rolling, were subjected to limiting dome height test. The formability limits are analyzed in terms of experimental FLD in three sample directions, Finite element validation and theoretical FLDs. Thereby the following points are made

- The experimental FLD of Zircaloy-4 shows negative slopes both in right hand and left-hand side of the FLD. The negative trend is drastically decreased from left hand side of the FLD to the right, indicating that the material has higher drawability than stretchability.
- It is validated by identifying the fracture on the predicted cups while strain paths are

intersecting the incorporated FLD. Also, the predicted strain paths are closer to that of the experimental ones.

- Both, the experimental and predicted LDH values show a decreasing trend from tension-compression region to equi-biaxial mode which is a good agreement with the higher formability on the left-hand side of the FLD than that of the right-hand side of the FLD.
- The true strain values, major and minor, with respect to curve linear distance from the pole are positive and nearly equal for the lubricated sample, indicating the near equi-biaxial tension and these values are in good agreement with the FEM predicted values. Further, the non-lubricated sample shows near plain strain mode while the small width sample is resulting in tension – compression mode.
- The variation in the true major strain values ensured different drawability of the material with respect to the orientation of the sheet.
- The strain signature completely depends on the strain path during deformation inherited from the specimen design, and lubrication condition imposed in the Zirconium-4 alloy sheet materials.
- The Slab-route sheet (SRS) Zirconium material showed higher forming limits along all the strains paths as compared to that of the tube route sheet (TRS) Zirconium alloy sheets. This observation was consistently same for all the three orientation with respect to the rolling direction of the sheet. Thus, the SRS Zirconium alloy offers excellent scope for producing components where stretching and drawing operation are the predominant mode of deformation.
- The SRS Zirconium alloy gives better and more uniform strain distribution during the stretch forming operation than the TRS Zirconium alloy sheets. The strain distribution profiles revealed two major strain peaks symmetrically located about the pole.

However, the magnitude was unequal. The SRS material showed higher peak strain as compared to TRS material signifying higher formability of the material.

- Hill-Swift criterion (H-S), Storen-Rice bifurcation criterion (S-R), Bressan and Williams (B-W) model, Hill-Tresca (H-T) model are calibrated for Zicaloy-4 (TRS) material. B-W shear instability criteria is predicting well in tension-compression region and at near plain strain region and H-S criterion is in good agreement with the experimental data at near equi-biaxial region.
- To get actual FLD, the limiting strains need to be calculated under six to eight different strain paths. However, in this work the limiting strains were calculated under three different strain paths. Therefore, this is only an approximate FLD and more experiments are required to get the precise FLD.

# Chapter 7

## Conclusions and Future work

The Zircaloy-4 sheet materials, produced from both pilgering (Tube Route Sheet, TRS) and rolling (Slab Route Sheet, SRS) have been used in the current study. Besides, the Low Oxygen Sheet (LOS), which is also a Slab Route Sheet with less Oxygen content, has been used. Several tests were conducted to study the characteristics of sheet materials and the conclusions obtained from the analysis are presented in section 7.1. The specific contributions to the research and future scope of work are highlighted in section 7.2 and section 7.3 respectively.

### 7.1 Conclusions

- The Zircaloy-4 sheet materials, as it is in received state, were characterized in terms of their microstructure, texture, tensile properties and fractography at room temperature by conducting EBSD, XRD, Tensile and SEM tests and then the following conclusions are drawing by analysing their characteristics.
  - Microstructure study of the three materials reveal the equiaxed grains and It is also clear that the majority of the grains have their basal poles parallel to N= sheet plane normal (the red grains).
  - All the three sheet materials exhibit the presence of moderate texture at room temperature. The intensity is maximum ( $f(g) = 6.5$ ) in TRS samples in comparison to those of the SRS ( $f(g) = 4.7$ ) and LOS ( $f(g) = 4.8$ ).
  - With an increase in strain rate at room temperature, the strength parameters ( $\sigma_Y$  and  $\sigma_{UTS}$ ) increased while elongation values decreased.
  - The yield strength and percentage elongation values vary with respect to the sample orientation from longitudinal (L) to transverse (T) and the variations are captured

in terms of yield strength and elongation-based anisotropy parameters ( $A_{IP}$  and  $\delta$ ) values. The inplane anisotropy ( $A_{IP}$ ) and anisotropy index ( $\delta$ ) values are moderate which indicate the moderate texture presence in the material, which is in good agreement with the result obtained by pole figures and ODF obtained by XRD test. In this way, a correlation between texture and sample orientation-based flow parameters has been established in three different Zircaloy-4 sheet materials.

- To understand the flow behaviour, especially in hardening region, the stress-strain data at room temperature is fitted with Holloman equation, which resulted in a good fit with  $R^2$  values lies in the range of 0.99433 to 0.99954.
  - The hardening behaviour of the three alloys is captured in terms of the log scaled true stress-strain graphs and instantaneous work hardening curves. The true stress-strain graphs reveal the single mechanism activation in tensile test and instantaneous work hardening curves exhibit the three typical regimes (i.e. regime I, regime II and regime III).
  - The fracture surface of the tensile tests at room temperature exhibit dimple structure indicating ductile failure of the materials irrespective of the variation of the strain rate.
- Similar to the correlation between tensile properties and its texture at room temperature as presented in above conclusions, the orientation dependant tensile flow behaviour at elevated temperatures ( $75^\circ\text{C}$  to  $225^\circ\text{C}$  with an increment of  $75^\circ\text{C}$ , at strain rate of  $0.001\text{s}^{-1}$ ) is studied. The effect of temperature on texture of the material also is studied in terms of pole figures and ODF by conducting XRD tests. Further, the fracture surfaces of the material after the tensile tests are analyzed. The conclusions of all these studies are listed below.

- All the three materials exhibit moderate texture and the LOS material shows maximum texture intensity among the three. The basal pole figures do not exhibit perfect c-type texture.
  - Irrespective of temperature variation, the yield strength ( $\sigma_Y$ ) follows a specific trend, that it is maximum and minimum along T and L sample directions respectively in all the three alloys.
  - The  $A_{IP}$  and  $\delta$  values are determined and the calculated moderate values indicate the presence of moderate texture in all the three alloys at elevated temperatures.
  - At elevated temperatures also, the true plastic stress and true plastic strain values are best fitted with the Holloman equation and the  $R^2$  ranges between 0.99039 and 0.99959.
  - Similar to the room temperature, the derivative curves, irrespective of variation in temperature, exhibits the three typical work hardening regions (i.e., Regime I, II and III).
- Furthermore, the experimental stress strain data at different temperatures (Room temperature and 348K to 498K) and strain rates ( $0.001s^{-1}$ ,  $0.005s^{-1}$  and  $0.01s^{-1}$ ) are used to calibrate constitutive models for the Zircaloy-4 sheet materials (LOS, SRS, TRS). The conclusions of the constitutive model's study are presented below.
- Johnson Cook model is calibrated for all the three types of Zircaloy-4 materials and it is resulted in very poor goodness of fit with maximum  $R$  value of 0.7262 and minimum average absolute error of 11.1421% for LOS among the three materials.
  - Modified Zerilli-Armstrong model is calibrated for all the three types of Zircaloy-4 materials and it is resulted in moderate goodness of fit with maximum  $R$  value of 0.9788 and delta value of 4.3042% for SRS among the three Zircaloy-4 sheet materials.

- Modified Arrhenius type equation is calibrated for LOS, SRS and TRS materials and it is resulted in very high goodness of fit with maximum  $R$  value of 0.9950 and minimum delta value of 1.1132% for LOS material among the three materials.
  - The comparisons among the three types of constitutive equations for all the three materials show that the  $m$ - $Arr$  is suitable for good predictability of flow stress even though it has a greater number of constants to be determined.
- Zircaloy-4 sheet materials, produced by pilgering and rolling methods, were subjected to limiting dome height test. The formability limits are analyzed in terms of experimental FLDs in three sample directions, strain distribution on samples, finite element simulation, and theoretical FLDs. Thereby, the following conclusions are made.
- The experimental FLD of TRS shows negative slopes both in right hand and left-hand side of the FLD. The negative trend is drastically decreased from left hand side of the FLD to the right, indicating that the material has higher drawability than stretch ability.
  - It is identified that the fracture on the predicted cups while strain paths are intersecting the incorporated FLD. Also, the predicted strain paths are closer to that of the experimental ones.
  - Both, the experimental and predicted LDH values show a decreasing trend from tension-compression region to equi-biaxial mode which is a good agreement with the higher formability on the left-hand side of the FLD than that of the right-hand side of the FLD.
  - The true strain values, major and minor, with respect to curve linear distance from the pole are positive and nearly equal for the lubricated sample, indicating the near equi-biaxial tension and these values are in good agreement with the FEM predicted

values. Further, the non-lubricated sample shows near plain strain mode while the small width sample is resulting in tension – compression mode.

- The variation in the true major strain values ensured different drawability of the material with respect to the orientation of the sheet.
- The strain signature completely depends on the strain path during deformation inherited from the specimen design, and lubrication condition imposed in the Zirconium-4 alloy sheet materials.
- The Slab-route sheet (SRS) Zirconium material showed higher forming limits along all the strains paths as compared to that of the tube route sheet (TRS) Zirconium alloy sheets. This observation was consistently same for all the three orientation with respect to the rolling direction of the sheet. Thus, the SRS Zirconium alloy offers excellent scope for producing components where stretching and drawing operation are the predominant mode of deformation.
- The SRS Zirconium alloy gives better and more uniform strain distribution during the stretch forming operation than the TRS Zirconium alloy sheets. The strain distribution profiles revealed two major strain peaks symmetrically located about the pole. However, the magnitude was unequal. The SRS material showed higher peak strain as compared to TRS material signifying higher formability of the material.
- Hill-Swift criterion (H-S), Storen-Rice bifurcation criterion (S-R), Bressan and Williams (B-W) model, Hill-Tresca (H-T) model are calibrated for Zicaloy-4 (TRS) material. B-W shear instability criteria is predicting well in tension-compression region and at near plain strain region and H-S criterion is in good agreement with the experimental data at near equi-biaxial region.



## 7.2 Specific Contributions to the Research

Through this thesis on the formability of three different Zircaloy-4 sheet materials the following specific contributions have been made towards the frontiers of state-of-art research on nuclear structural materials.

- ❖ Determination of tensile properties of three different types of Zircaloy-4 sheet materials at different temperatures and strain rates.
- ❖ Determination of the variation of the tensile properties with strain rate and temperature in three sample directions and their correlation with texture.
- ❖ Calibration of constitutive models for the three Zircaloy-4 materials and selecting a suitable model by comparing them.
- ❖ Development of experimental forming limit diagrams for Zircaloy-4 sheet materials produced from both pilgering and rolling methods in three different sample orientations.
- ❖ Validation of the limiting dome height test of Zircaloy-4 sheet material with FEM simulation.
- ❖ Calibration of different theoretical forming limit diagrams and comparing their predictability with experimental data.

## 7.3 Future Scope of Work

The research work that is presented in the thesis can be enhanced in the following directions.

- The forming limit diagrams for Zircaloy-4 sheet materials at elevated temperature can be accomplished by using inert gas atmosphere.
- The texture can be controlled by altering the manufacturing parameters of the Zircaloy-4 sheet materials thereby altering the formability of the sheet material.
- The stamping of spacer grid strips can be simulated thereby understanding the fracture zones of the strips

## References

- Abe, Hideaki, and Munekatsu Furugen. 2012. "Method of Evaluating Workability in Cold Pilgering." *Journal of Materials Processing Technology* 212(8): 1687–93. <http://dx.doi.org/10.1016/j.jmatprotec.2012.03.012>.
- Abe, Hiroaki et al. 2015. "Development of Advanced Expansion Due to Compression (A-EDC) Test Method for Safety Evaluation of Degraded Nuclear Fuel Cladding Materials." *Journal of Nuclear Science and Technology* 52(10): 1232–39.
- Akhiani, Hamed, and Jerzy A Szpunar. 2013. "Effect of Surface Roughness on the Texture and Oxidation Behaviour of Zircaloy-4 Cladding Tube." *Applied Surface Science* 285: 832–39.
- Badrish, Anand, Ayush Morchhale, Nitin Kotkunde, and Swadesh Kumar Singh. 2020. "Influence of Material Modeling on Warm Forming Behaviour of Nickel Based Super Alloy." *International Journal of Material Forming*: 1–21.
- Ballinger, R. G., G E Lucas, and R M Pelloux. 1984. "The Effect of Plastic Strain on the Evolution of Crystallographic Texture in Zircaloy-2." *Journal of Nuclear Materials* 126(1): 53–69.
- Banumathy, S., R. K. Mandal, and A. K. Singh. 2009a. "Structure of Orthorhombic Martensitic Phase in Binary Ti–Nb Alloys." *Journal of Applied Physics* 106(9): 093518. <http://aip.scitation.org/doi/10.1063/1.3255966>.
- Banumathy, S, R K Mandal, and A K Singh. 2009b. "Structure of Orthorhombic Martensitic Phase in Binary Ti–Nb Alloys." *Journal of Applied Physics* 106(9): 93518.
- Bind, A K, S Sunil, and R N Singh. 2016. "Effect of Hydrogen Isotope Content on Tensile Flow Behaviour of Zr-2.5 Nb Pressure Tube Material between 25 and 300 C." *Journal of Nuclear Materials* 476: 5–12.
- Bodunrin, Michael Oluwatosin. 2020. "Flow Stress Prediction Using Hyperbolic-Sine

- Arrhenius Constants Optimised by Simple Generalised Reduced Gradient Refinement.”  
*Journal of Materials Research and Technology*.
- Bressan, J. D., and J. A. Williams. 1983. “The Use of a Shear Instability Criterion to Predict Local Necking in Sheet Metal Deformation.” *International Journal of Mechanical Sciences* 25(3): 155–68.
- Cappelaere, Chantal et al. 2012. “Thermal Creep Model for CWSR Zircaloy-4 Cladding Taking into Account the Annealing of the Irradiation Hardening.” *Nuclear Technology* 177(2): 257–72. <https://www.tandfonline.com/doi/full/10.13182/NT12-A13370>.
- Che, Jiangtao et al. 2018. “An Integrated Johnson–Cook and Zerilli–Armstrong Model for Material Flow Behaviour of Ti–6Al–4V at High Strain Rate and Elevated Temperature.” *Journal of the Brazilian Society of Mechanical Sciences and Engineering* 40(5): 253.
- Chen, Fei et al. 2019. “Physically-Based Constitutive Modelling of As-Cast CL70 Steel for Hot Deformation.” *Metals and Materials International*: 1–11.
- Cox, B. 2005. “Some Thoughts on the Mechanisms of In-Reactor Corrosion of Zirconium Alloys.” *Journal of Nuclear Materials* 336(2–3): 331–68.
- Deng, Siying et al. 2019. “A Model to Describe Hardening Behaviour of Zircaloy-4 Tube during Cold Pilgering Process.” *International Journal of Material Forming* 12(2): 321–29.
- Desu, Raghuram Karthik, Swadesh Kumar Singh, and Amit Kumar Gupta. 2016. “Comparative Study of Warm and Hydromechanical Deep Drawing for Low-Carbon Steel.” *The International Journal of Advanced Manufacturing Technology* 85(1–4): 661–72. <http://link.springer.com/10.1007/s00170-015-7819-2>.
- Dieter, George Ellwood, and David J Bacon. 1962. “Mechanical Metallurgy.” *Journal of the Franklin Institute* 273(4): 338.  
<http://linkinghub.elsevier.com/retrieve/pii/S0016003262911456>.

- Eyler, J H. 1981. *Development and Control of the Process for the Manufacture of Zircaloy-4 Tubing for LWBR Fuel Rods*. Bettis Atomic Power Lab., West Mifflin, PA (USA).
- Fu, Zhong-tao et al. 2016. "Identification of Constitutive Model Parameters for Nickel Aluminum Bronze in Machining." *Transactions of Nonferrous Metals Society of China* 26(4): 1105–11.
- Fuloria, Devasri et al. 2016. "Tensile Properties and Microstructural Evolution of Zircaloy-4 Processed through Rolling at Different Temperatures." *Materials & Design* 103: 40–51. <https://linkinghub.elsevier.com/retrieve/pii/S0264127516305275>.
- Geng, Peihao, Guoliang Qin, Jun Zhou, and Zengda Zou. 2018. "Hot Deformation Behaviour and Constitutive Model of GH4169 Superalloy for Linear Friction Welding Process." *Journal of Manufacturing Processes* 32: 469–81.
- Ghazanfari, Amir, and Ahmad Assempour. 2012. "Calibration of Forming Limit Diagrams Using a Modified Marciniak-Kuczynski Model and an Empirical Law." *Materials and Design* 34: 185–91. <http://dx.doi.org/10.1016/j.matdes.2011.07.057>.
- Gupta, Amit Kumar et al. 2013. "Development of Constitutive Models for Dynamic Strain Aging Regime in Austenitic Stainless Steel 304." *Materials & Design* 45: 616–27. <http://dx.doi.org/10.1016/j.matdes.2012.09.041>.
- Gupta, Amit Kumar, V K Anirudh, and Swadesh Kumar Singh. 2013. "Constitutive Models to Predict Flow Stress in Austenitic Stainless Steel 316 at Elevated Temperatures." *Materials & Design* 43: 410–18.
- Gupta, Amit Kumar, and D Ravi Kumar. 2006. "Formability of Galvanized Interstitial-Free Steel Sheets." *Journal of Materials Processing Technology* 172(2)(October 2005): 225–37.
- Haggag, Fahmy M, and K Linga Murty. 1997. "A Novel Stress-Strain Microprobe for Nondestructive Evaluation." In *Nondestructive Evaluation and Materials Properties III*,

The Minerals, Metals & Materials Society.

Hill, R. 1952. "On Discontinuous Plastic States, with Special Reference to Localized Necking in Thin Sheets." *Journal of the Mechanics and Physics of Solids* 1(1): 19–30.

Hong, Hyun Seon, Seon Jin Kim, and Kyung Sub Lee. 2002. "Influence of Dilute Silicon Addition on the Oxidation Resistance and Tensile Properties of Modified Zircaloy-4." *Journal of nuclear materials* 304(1): 8–14.

Kass, Stanley. 1964. "The Development of the Zircaloys." In *Corrosion of Zirconium Alloys*, ASTM International, 3-3–25. <http://www.astm.org/doiLink.cgi?STP47070S>.

Keller, C, E Hug, and D Chateigner. 2009. "On the Origin of the Stress Decrease for Nickel Polycrystals with Few Grains across the Thickness." *Materials Science and Engineering A* 500(1–2): 207–15.

Kelly, P M, and P D Smith. 1973. "Strain-Ageing in Zirconium-Oxygen Alloys." *Journal of Nuclear Materials* 46(1): 23–34.

Kim, Kwang Yong, and Jun Woo Seo. 2005. "Numerical Optimization for the Design of a Spacer Grid with Mixing Vanes in a Pressurized Water Reactor Fuel Assembly." *Nuclear Technology* 149(1): 62–70.  
<https://www.tandfonline.com/doi/full/10.13182/NT05-A3579>.

Kim, Minsoo, Felix Rickhey, Hyungyil Lee, and Naksoo Kim. 2016. "Analytical Determination of Forming Limit Curve for Zirlo and Its Experimental Validation." *Journal of Manufacturing Processes* 23: 122–29.  
<http://dx.doi.org/10.1016/j.jmapro.2016.06.006>.

Kotkunde, Nitin et al. 2017. "Experimental and Theoretical Investigation of Forming Limit Diagram for Ti-6Al-4 V Alloy at Warm Condition." *International Journal of Material Forming* 10(2): 255–66.

Kotkunde, Nitin, Aditya D Deole, Amit Kumar Gupta, and Swadesh Kumar Singh. 2014.

- “Comparative Study of Constitutive Modeling for Ti–6Al–4V Alloy at Low Strain Rates and Elevated Temperatures.” *Materials & Design* 55: 999–1005.
- Kotkunde, Nitin, Amit Kumar Gupta, and Swadesh Kumar Singh. 2015. “Formability Study of Ti-6Al-4V Alloy under Warm Conditions.” *Advances in Materials and Processing Technologies* 1(1–2): 210–22.  
<http://www.tandfonline.com/doi/full/10.1080/2374068X.2015.1118994>.
- Krishnan, R., and M. K. Asundi. 1981. “Zirconium Alloys in Nuclear Technology.” *Proceedings of the Indian Academy of Sciences Section C: Engineering Sciences* 4(1): 41–56.
- Lei, L I U, Yun-xin Wu, GONG Hai, and WANG Kai. 2019. “Modification of Constitutive Model and Evolution of Activation Energy on 2219 Aluminum Alloy during Warm Deformation Process.” *Transactions of Nonferrous Metals Society of China* 29(3): 448–59.
- Lian, Junhe et al. 2017. “An Evolving Non-Associated Hill48 Plasticity Model Accounting for Anisotropic Hardening and r-Value Evolution and Its Application to Forming Limit Prediction.” *International Journal of Solids and Structures*.
- Lin, Y C, and Xiao-Min Chen. 2011. “A Critical Review of Experimental Results and Constitutive Descriptions for Metals and Alloys in Hot Working.” *Materials & Design* 32(4): 1733–59.
- Lin, Yanli et al. 2018. “Constitutive Modeling of the High-Temperature Flow Behaviour of  $\alpha$ -Ti Alloy Tube.” *Journal of Materials Engineering and Performance* 27(5): 2475–83.
- Liu, Chengze et al. 2018. “Texture and Yielding Anisotropy of Zircaloy-4 Alloy Cladding Tube Produced by Cold Pilger Rolling and Annealing.” *Materials Science and Engineering A* 719: 147–54. <https://doi.org/10.1016/j.msea.2018.02.043>.
- Liu, Lei, Yun-xin Wu, Hai Gong, and Kai Wang. 2019. “Modification of Constitutive Model

- and Evolution of Activation Energy on 2219 Aluminum Alloy during Warm Deformation Process.” *Transactions of Nonferrous Metals Society of China* 29(3): 448–59. [http://dx.doi.org/10.1016/S1003-6326\(19\)64954-X](http://dx.doi.org/10.1016/S1003-6326(19)64954-X).
- Long, F. et al. 2017. “Microstructure Characterization of a Hydride Blister in Zircaloy-4 by EBSD and TEM.” *Acta Materialia* 129: 450–61. <http://dx.doi.org/10.1016/j.actamat.2017.03.016>.
- Lustman, B. 1979. “Zirconium Technology—Twenty Years of Evolution.” In *Zirconium in the Nuclear Industry*, 100 Barr Harbor Drive, PO Box C700, West Conshohocken, PA 19428-2959: ASTM International, 5-5–14. <http://www.astm.org/doiLink.cgi?STP36669S>.
- Manda, Premkumar, Uday Chakkingal, and A. K. Singh. 2016. “Effect of Alloying Elements in Hot-Rolled Metastable  $\beta$ -Titanium Alloys. Part II: Mechanical Properties.” *Metallurgical and Materials Transactions A* 47(7): 3447–63. <http://link.springer.com/10.1007/s11661-016-3508-5>.
- Marciniak, Zdzislaw, and Kazimierz Kuczyński. 1967. “Limit Strains in the Processes of Stretch-Forming Sheet Metal.” *International Journal of Mechanical Sciences* 9(9): 609–20.
- Marciniak, Zdzisław, Kazimierz Kuczyński, and Tadeusz Pokora. 1973. “Influence of the Plastic Properties of a Material on the Forming Limit Diagram for Sheet Metal in Tension.” *International Journal of Mechanical Sciences* 15(10): 789–800.
- Marimuthu, Karuppasamy Pandian, Wanseop Choi, Naksoo Kim, and Hyungyil Lee. 2018. “Numerical Investigations on the Effect of Pit on Two-Step Dimple Forming of Atomic Fuel Spacer Grid.” *International Journal of Advanced Manufacturing Technology* 94(1–4): 293–99.
- Mondal, Chandan, A.K. Singh, A.K. Mukhopadhyay, and K Chattopadhyay. 2013. “Tensile

- Flow and Work Hardening Behaviour of Hot Cross-Rolled AA7010 Aluminum Alloy Sheets.” *Materials Science and Engineering: A* 577: 87–100.  
<http://dx.doi.org/10.1016/j.msea.2013.03.079>.
- Murty, K. Linga, and Indrajit Charit. 2006a. “Texture Development and Anisotropic Deformation of Zircalloys.” *Progress in Nuclear Energy* 48(4): 325–59.
- Murty, K. Linga, and Indrajit Charit. 2006b. “Texture Development and Anisotropic Deformation of Zircalloys.” *Progress in Nuclear Energy* 48(4): 325–59.
- Nagase, Fumihisa, and Toyoshi Fuketa. 2006. “Fracture Behaviour of Irradiated Zircaloy-4 Cladding under Simulated LOCA Conditions.” *Journal of nuclear science and technology* 43(9): 1114–19.
- Nakamura, Shoji, Hideo Harada, Subramanian Raman, and Paul E. Koehler. 2007. “Thermal Neutron Capture Cross Sections of Zirconium-91 and Zirconium-93 by Prompt  $\gamma$ -Ray Spectroscopy.” *Journal of Nuclear Science and Technology* 44(1): 21–28.
- Philippe, M J, M Serghat, Paul Van Houtte, and C Esling. 1995. “Modelling of Texture Evolution for Materials of Hexagonal Symmetry—II. Application to Zirconium and Titanium  $\alpha$  or near  $\alpha$  Alloys.” *Acta metallurgica et materialia* 43(4): 1619–30.
- Prasad, K. S. et al. 2017. “Microstructures, Forming Limit and Failure Analyses of Inconel 718 Sheets for Fabrication of Aerospace Components.” *Journal of Materials Engineering and Performance* 26: 1513–30.
- Prasad, K. Sajun, Amit Kumar Gupta, Yashjeet Singh, and Swadesh Kumar Singh. 2016. “A Modified Mechanical Threshold Stress Constitutive Model for Austenitic Stainless Steels.” *Journal of Materials Engineering and Performance* 25(12): 5411–23.  
<http://link.springer.com/10.1007/s11665-016-2389-5>.
- Prasad, K.S. et al. 2018. “Prediction of Fracture and Deep Drawing Behaviour of Solution Treated Inconel-718 Sheets: Numerical Modeling and Experimental Validation.”



*Materials Science and Engineering A* 733.

- Pshenichnikov, Anton, Juri Stuckert, and Mario Walter. 2015. "Microstructure and Mechanical Properties of Zircaloy-4 Cladding Hydrogenated at Temperatures Typical for Loss-of-Coolant Accident (LOCA) Conditions." *Nuclear Engineering and Design* 283: 33–39.
- Qiang, Zhao et al. 2020. "Hot Deformation Behaviour of 7A04 Aluminum Alloy at Elevated Temperature: Constitutive Modeling and Verification." *International Journal of Material Forming* 13(2): 293–302.
- Qiu, X. et al. 2001. "Effect of Intrinsic Lattice Resistance in Strain Gradient Plasticity." *Acta Materialia* 49(19): 3949–58.  
<http://linkinghub.elsevier.com/retrieve/pii/S1359645401002993>.
- Rasaee, Sajad, A H Mirzaei, and D Almasi. 2020. "Constitutive Modelling of Al7075 Using the Johnson–Cook Model." *Bulletin of Materials Science* 43(1): 23.
- Ravi Kumar, D, and K Swaminathan. 1999. "Formability of Two Aluminium Alloys." *Materials science and technology* 15(11): 1241–52.
- Rickhey, Felix, Minsoo Kim, Hyungyil Lee, and Naksoo Kim. 2015. "Evaluation of Combined Hardening Coefficients of Zircaloy-4 Sheets by Simple Shear Test." *Materials & Design (1980-2015)* 65: 995–1000.
- Rickover, Hyman George, Lawton D Geiger, and Benjamin Lustman. 1975. *History of the Development of Zirconium Alloys for Use in Nuclear Reactors*. Energy Research and Development Administration.
- Roamer, P. et al. 1997. "Room Temperature Formability of Alloys 625LCF, 718 and 718SPF." In *Advanced Steel Processing and Products Research Center Colorado School of Mines Golden, CO, 80401.*, , 315–329.
- Rudra, Amitava, Satyabrata Das, and Rupa Dasgupta. 2019. "Constitutive Modeling for Hot

- Deformation Behaviour of Al-5083+ SiC Composite.” *Journal of Materials Engineering and Performance* 28(1): 87–99.
- Sarkar, Apu et al. 2016. “Investigation of Microstructure and Mechanical Properties of Proton Irradiated Zircaloy 2.” *Journal of Nuclear Materials* 479: 524–32.  
<http://dx.doi.org/10.1016/j.jnucmat.2016.07.050>.
- Le Saux, Matthieu et al. 2008. “A Model to Describe the Anisotropic Viscoplastic Mechanical Behaviour of Fresh and Irradiated Zircaloy-4 Fuel Claddings under RIA Loading Conditions.” *Journal of Nuclear Materials* 378(1): 60–69.
- Le Saux, Matthieu, Jacques Besson, and Sébastien Carassou. 2015. “A Model to Describe the Mechanical Behaviour and the Ductile Failure of Hydrided Zircaloy-4 Fuel Claddings between 25° C and 480° C.” *Journal of Nuclear Materials* 466: 43–55.
- Saxena, Ambuj, A Kumaraswamy, Nitin Kotkunde, and Kurra Suresh. 2019. “Constitutive Modeling of High-Temperature Flow Stress of Armor Steel in Ballistic Applications: A Comparative Study.” *Journal of Materials Engineering and Performance* 28(10): 6505–13.
- Seo, Yunmi, Hong Chul Hyun, Hyungyil Lee, and Naksoo Kim. 2011. “Forming Limit Diagrams of Zircaloy-4 and Zirlo Sheets for Stamping Process of Spacer Grids of Nuclear Fuel Rod.” *AIP Conference Proceedings* 1383: 92–98.
- Seong, Yujin et al. 2020. “Physics-Based Constitutive Model of Porous Materials for Die/Isostatic Compaction of Metallic Powders.” *Metals and Materials International* 26(2): 221–29.
- Setty, D. S., Reddy P. Ravinder, and A. L. N. Murthy. 2008. “Resistance Butt Welding of Zirconium Alloy Material.” *Materials and Manufacturing Processes* 23(8): 844–51.  
<http://www.tandfonline.com/doi/abs/10.1080/10426910802384904>.
- Shibata, Akira et al. 2016. “Corrosion Properties of Zircaloy-4 and M5 under Simulated PWR

- Water Conditions.” *Nuclear Technology* 196(1): 89–99.
- Shibata, Keiichi et al. 2011. “JENDL-4.0: A New Library for Nuclear Science and Engineering.” *Journal of Nuclear Science and Technology* 48(1): 1–30.
- Singh, Swadesh Kumar. 2010. “Development of ANN Model and Study the Effect of Temperature on Strain Ratio and Sensitivity Index of EDD Steel.” *International Journal of Material Forming* 3(4): 259–66. <http://link.springer.com/10.1007/s12289-010-0685-4>.
- Singh, Swadesh Kumar, Amrit Dixit, and D. Ravi Kumar. 2008. “Optimization of the Design Parameters of Modified Die in Hydro-Mechanical Deep Drawing Using LS-DYNA.” *The International Journal of Advanced Manufacturing Technology* 38(1–2): 32–37. <http://link.springer.com/10.1007/s00170-007-1083-z>.
- Singh, Swadesh Kumar, and D. Ravi Kumar. 2005. “Application of a Neural Network to Predict Thickness Strains and Finite Element Simulation of Hydro-Mechanical Deep Drawing.” *The International Journal of Advanced Manufacturing Technology* 25(1–2): 101–7. <http://link.springer.com/10.1007/s00170-003-1842-4>.
- Song, Kee-nam, and Sang-hoon Lee. 2012. “Effect of Weld Properties on the Crush Strength of the PWR Spacer Grid.” *Science and Technology of Nuclear Installations* 2012: 1–12.
- Song, Kee Nam, Soo Bum Lee, Moon Kyun Shin, et al. 2010. “New Spacer Grid to Enhance Mechanical/Structural Performance.” *Journal of nuclear science and technology* 47(3): 295–303.
- Song, Kee Nam, Soo Bum Lee, Moon Kyun SHIN, et al. 2010. “New Spacer Grid to Enhance Mechanical/Structural Performance.” *Journal of Nuclear Science and Technology* 47(3): 295–303. <http://www.tandfonline.com/doi/abs/10.1080/18811248.2010.9711957>.
- Srinivasulu, Sanaga, and Ashu Jain. 2006. “A Comparative Analysis of Training Methods for Artificial Neural Network Rainfall-Runoff Models.” *Applied Soft Computing Journal*

6(3): 295–306.

Stören, S., and J. R. Rice. 1975. “Localized Necking in Thin Sheets.” *Journal of the Mechanics and Physics of Solids* 23(6): 421–41.

Su, Nan et al. 2020. “Constitutive Modeling of 17-4PH Stainless Steel Sheet at Elevated Temperature and Statistical Optimization.” *Journal of Materials Engineering and Performance* 29(2): 1194–1205.

Swift, H. W. 1952. “Plastic Instability under Plane Stress.” *Journal of the Mechanics and Physics of Solids* 1(1): 1–18.

Talia, J E, and F Povolò. 1977. “Tensile Properties of Zircaloy-4.” *Journal of Nuclear Materials* 67(1–2): 198–206.

Tao, Zhi-jun et al. 2018. “A Modified Johnson–Cook Model for NC Warm Bending of Large Diameter Thin-Walled Ti–6Al–4V Tube in Wide Ranges of Strain Rates and Temperatures.” *Transactions of Nonferrous Metals Society of China* 28(2): 298–308.

Taouinet, Mustapha, N. E. Kamel, and S. Lebaili. 2013. “Diffusion Bonding Between Zircaloy-4 and 304L Stainless Steel in the Presence of a Eutectic.” *Materials and Manufacturing Processes* 28(12): 1327–34.

<http://www.tandfonline.com/doi/abs/10.1080/10426914.2013.822982>.

Tenckhoff, Erich. 2005. “Review of Deformation Mechanisms, Texture, and Mechanical Anisotropy in Zirconium and Zirconium Base Alloys.” *Journal of ASTM International* 2(4): 25–50. <http://www.astm.org/doiLink.cgi?JAI12945>.

Tonpe, Sunil, and U. Kamachi Mudali. 2017. “Effect of Thermomechanical Process on Microstructural Evolution, Mechanical and Corrosion Properties of Zircaloy-4 Tubes of Mock-up Dissolver Vessel.” *Materials and Manufacturing Processes* 32(1): 27–33.

Tung, Hsiao Ming, Tai Cheng Chen, and Che Chung Tseng. 2016. “Effects of Hydrogen Contents on the Mechanical Properties of Zircaloy-4 Sheets.” *Materials Science and*

- Engineering A* 659: 172–78. <http://dx.doi.org/10.1016/j.msea.2016.02.051>.
- Vacca, Annalisa et al. 2016. “Electrodeposition of Zirconium from 1-Butyl-1-Methylpyrrolidinium-Bis(Trifluoromethylsulfonyl)Imide: Electrochemical Behaviour and Reduction Pathway.” *Materials and Manufacturing Processes* 31(1): 74–80. <http://www.tandfonline.com/doi/full/10.1080/10426914.2015.1004698>.
- Vakhitova, E., D. Sornin, F. Barcelo, and M. François. 2017. “Texture Evolution in Oxide Dispersion Strengthened (ODS) Steel Tubes during Pilgering Process.” *Journal of Nuclear Materials* 494: 20–28. <http://dx.doi.org/10.1016/j.jnucmat.2017.07.002>.
- Wang, Xiang-dong et al. 2018. “Prediction on Hot Deformation Behaviour of Spray-Formed 7055 Aluminum Alloy via Phenomenological Models.” *Transactions of Nonferrous Metals Society of China* 28(8): 1484–94.
- Wei, Dejin, Ruirui Liu, Chengkun Zuo, and Haitao Zhou. 2020. “High Temperature Plastic Deformation Constitutive Equation of a New Alloy for Piston Ring.” *Metals and Materials International* 26: 739–746. <https://doi.org/10.1007/s12540-019-00480-3>.
- Wu, Y T, and C H Koo. 1997. “Effects of Texture on the Superplasticity of Ti-25Al-10Nb Alloy.” *Intermetallics* 5(1): 29–36.
- Xia, Chaoqun et al. 2016. “Effect of Annealing on Microstructure and Tensile Property of a Novel ZrB Alloy.” *Materials Science and Engineering: A* 674: 1–8. <http://dx.doi.org/10.1016/j.msea.2016.07.079>.
- Xu, Jian, Xinde Bai, An Jin, and Yudian Fan. 2000. “Effect of Yttrium Ion Implantation on Aqueous Corrosion Resistance of Zircaloy-4.” *Journal of Materials Science Letters* 19(18): 1633–35.
- Zener, Clarence, and John Herbert Hollomon. 1944. “Effect of Strain Rate upon Plastic Flow of Steel.” *J. Applied Phys.* 15(1): 22–32.
- Zhang, Hongming et al. 2018. “A Physically-Based Constitutive Modelling of a High

Strength Aluminum Alloy at Hot Working Conditions.” *Journal of Alloys and Compounds* 743: 283–93.

# List of Publications

## **International Journals**

1. Limbadri K, Singh SK, Satyanarayana K, Singh AK, Ram AM, Ravindran M, Krishna KM, Reddy MC, Suresh K. *Orientation-Dependent Tensile Flow Behaviour of Zircaloy-4 at Room Temperature*. Metallography, Microstructure, and Analysis. 2018 Aug 1;7(4):421-33.
2. Singh SK, Limbadri K, Singh AK, Ram AM, Ravindran M, Krishna M, Reddy MC, Suresh K, Prasad KS, Panda SK. *Studies on texture and formability of Zircaloy-4 produced by pilgering route*. Journal of Materials Research and Technology. 2019 Apr 1;8(2):2120-9.
3. Limbadri K, Singh SK, Satyanarayana K, Singh AK, Ram AM, Ravindran M, Krishnan MK, Chaithanya K, Suresh K, *Effect of Processing Routes on Orientation Dependent Tensile Flow Behaviour of Zircaloy-4 at Elevated Temperatures*. Metallography, Microstructure, and Analysis 2019 Jun 15;8(3):393-405.
4. Limbadri K, Suresh K, Singh SK. *Flow stress prediction of zircaloy-4 at elevated temperatures using KHL Constitutive model*. Advances in Materials Processing Technologies. 2020 March 6;6(2):362-371.

## **Submitted**

1. Limbadri K, Suresh K, Singh SK. *Constitutive models for flow stress prediction of Zircaloy-4*. Transactions of Nonferrous Metals Society of China (under review).

## **International Conferences**

1. Limbadri K, Toshniwal K, Suresh K, Gupta AK, Kutumbarao VV, Ram M, Ravindran M, Kalyankrishnan G, Singh SK. *Stress Variation of Zircaloy-4 and Johnson Cook Model for rolled sheets*. Materials Today: Proceedings. 2018 Dec 31;5(2):3793-801. (Scopus)
2. Limbadri K, Krishnamurthy HN, Ram AM, Saibaba N, Rao VK, Murthy JN, Gupta AK, Singh SK. *Development of Johnson cook model for Zircaloy-4 with low oxygen content*. Materials Today: Proceedings. 2017 Jan 1;4(2):966-74. (Scopus).

## Biography

**Biography of the Candidate: Mr. K Limbadri** completed his B. Tech from Gokaraju Rangaraju Institute of Engineering and Technology (GRIET), Hyderabad in 2012. He received his M. Tech degree in Materials Technology from NIT Warangal in 2014. He has 6 years of teaching experience in reputed engineering colleges. He is pursuing his Ph. D. in the Department of Mechanical Engineering at BITS Pilani Hyderabad Campus. His research interest Includes, Microstructure and Texture studies, Formability of Sheet Metal Forming and Constitutive modelling.

**Biography of the Supervisor: Dr. Kurra Suresh** holds his Ph. D degree from BITS- Pilani. He did his Masters in Production Engineering from Indian Institute of Technology Delhi (IITD) and B.E in Mechanical Engineering from Andhra University. He is Presently working as Assistant Professor in the Department of Mechanical engineering at BITS Pilani Hyderabad Campus. He has the teaching and research experience of around 14 years. He has published 12 research articles in reputed international journals and about 17 conference papers. His research areas include Sheet metal forming, Bulk metal forming, Advanced manufacturing processes, Finite element simulation of manufacturing processes, CAD/CAM Modelling and optimization. He also received sponsored project from Department of Science and Technology (DST) and Aeronautics Research Development Board (AR&DB).

**Biography of the Co-Supervisor: Dr. Swadesh Kumar Singh** holds a Masters and Ph. D. from Indian Institute of Technology (IIT) Delhi India. He received a gold medal for his Bachelor's degree at AMU. He is presently working as a Professor in the Department of Mechanical Engineering at GRIET, Hyderabad, India. Prior to joining GRIET he has also served as Assistant Executive Engineer in Indian Engineering Services (IES) and also worked with BHEL for a brief period of time. Dr. S K Singh has been involved in research on



Numerical Simulation and Experimental studies on Formability of Sheet Metal Forming at room and at elevated temperatures, Characterization of Metals and Bio composites. He has done extensive research in the area of Characterization of Low Carbon and Austenitic Stainless Steels, Titanium Grade-5, DP Steel and Zircaloy. He is awarded Young Scientist award by Department of Science and Technology, Govt of India and Young Teacher award by All India Council of Technical Education, Govt of India for his contribution in research. He has authored over 95 international journal and 70 conference papers and received the sponsored project grants from various agencies. He has got h-index of 18 on Scopus. His articles appear in high impact factor journals like Materials & Design, Journal of Material Processing Technology, CIRP and so on. He received the research funding from Department of Science and Technology, All India Counsel of Technical Education, Department of Atomic Energy, Aviation Research and Development board and several consultancies from Industries.

